2023-05-01

Evaluating The Impact Of Climate Variability And Landcover Changes On Hydrologic Responses

Marisol Dominguez
University of Texas at El Paso

EVALUATING THE IMPACT OF CLIMATE VARIABILITY AND LANDCOVER CHANGES ON HYDROLOGIC RESPONSES

MARISOL DOMINGUEZ TUDA

Doctoral Program in Geological Sciences

APPROVED:

Hugo Gutierrez-Jurado, Ph.D., Chair

Christopher Brown, Ph.D.

Gabriel de Oliveira, Ph.D.

Diane Doser, Ph.D.

Laura Alvarez, Ph.D.

Marianne Karplus, Ph.D

Stephen Crites, Ph.D.
Dean of the Graduate School

EVALUATING THE IMPACT OF CLIMATE VARIABILITY AND LANDCOVER CHANGES ON HYDROLOGIC RESPONSES

by

MARISOL DOMINGUEZ TUDA, B.S., M.S

DISSERTATION

Presented to the Faculty of the Graduate School of

The University of Texas at El Paso

in Partial Fulfillment

of the Requirements

for the Degree of

DOCTOR OF PHILOSOPHY

Department of Earth, Environmental & Resource Sciences

THE UNIVERSITY OF TEXAS AT EL PASO

May 2023

Acknowledgments

I would like to express my sincere gratitude to my project advisor, Dr. Hugo Gutierrez-Jurado, for his patience and guidance throughout the completion of this work. Also, his encouragement to work on different projects allowed me to travel to places around the globe to present this art piece. To my committee members, Dr. Marianne Karplus, Dr. Christopher Brown, Dr. Diane Doser, Dr. Gabriel de Oliveira, and Dr. Laura Alvarez for being part of this journey while providing their outstanding support and feedback. To the Earth, Environmental, and Resource Sciences department for providing all the elements needed to complete my research project. Most importantly, thanks to God, my family, and my friends who made this possible. Also, to Hatsumi, my Akita-inu, for her company. Support for the research was provided by NSF Graduate Research Fellowship Award Fellow ID: Fellow ID: 2018252939 Grant # 1848741.

Table of Contents

List of Tables

List of Figures

Introduction

Projected climate and land cover changes in the 21st century profoundly impact the functioning of the earth's water cycle. Identifying the components that contribute to the persistence and resilience of watersheds in light of climate change constitutes a research priority of global relevance, and will enable detect the areas most sensitive to climate variability and landcover changes. Global vulnerability of ecosystem services, particularly water service provision, needs to be urgently and continually assessed, given the unceasing human and climate-induced changes in land cover conditions worldwide. Given the increasing rate of extreme weather events, we present three interrelated research studies evaluating the impact of climate variability and land cover changes on hydrologic responses while displaying the direction of hydrologic behavior and climate conditions.

Previous studies have documented hydrologic responses to climate variability in a few catchments within geographically limited regions. Because of this limited geographic extent, other important landscape factors such as elevation, slope, and aspect, which influence climate variabilities, have not been assessed at a large scale. Thus, there is a lack of a global synthesis evaluating the hydrologic responses to climatic variability, while evaluating the role of the topography in altering the response. In terms of the effects of landcover changes and their impact on hydrologic responses, previous studies have mainly focused on the effect of forest cover loss on Temperate Coniferous forests and the tropical Amazonia region, emphasizing the need for understanding the impacts across other forest types or other basins of similar biome to reveal the directions that major water resources are heading in a global scale. Although there is evidence of changing water yield (increasing or decreasing) under forest disturbance, there is no consensus on the direction of hydrologic changes. Also, most of these studies have not been assessed quantitatively limiting our knowledge of the reliable extent of the land cover effects on hydrologic

changes.

Human-driven deforestation and wildfires are major causes of tree cover loss. Many of these events occur in highly threatened-biodiverse tropical rainforests and boreal ecosystems. However, their impacts on hydrologic processes have not been systematically studied and the directions in which hydrologic changes may be occurring are still unclear. For example, although the Amazon basin has been extensively studied (Chambers & Artaxo, 2017; Lawrence & Vandecar, 2015; Leite-Filho et al., 2021; Malhi et al., 2008; Spracklen Xu et al., 2022 & Garcia-Carreras, 2015), other important tropical basins that have a major influence on global climates, such as the Central African and Southeast Asian forests have received less attention (Lawrence & Vandecar, 2015). Furthermore, the frequency of fire and forest exploitation leading to forest clearing in boreal systems is proportionally second to that in tropical ecosystems (Hansen et al., 2013), but only a few studies evaluate these impacts on boreal hydrology (Pimentel & Arheimer, 2021). Compounded with the loss of tree cover, changes in land surface properties reinforce current climatic trends such as rising temperatures leading to increasing snowmelt in high-latitude regions. Studies evaluating the role of forest clearing in these dynamics are missing or fragmented (te Wierik et al., 2021; Valeo et al., 2003). Given the lack of clarity on the effects of forest disturbance on hydrologic responses and the thresholds driving changes in water yield and regional climate, reporting the tipping points leading to significant changes in the hydrologic sensitivity in the world's major forests is critical to aid in forest management strategies to prevent irreversible or permanent changes in freshwater resources.

First, we present a global assessment assessing the sensitivity of the world's water landscapes to climate variability during 2001-2016, using a new metric called the Hydrologic Sensitivity Index (HSi) (Chapter 2). This equation is based on the well-known Budyko curve that uses annual values of Potential and Actual Evapotranspiration (PET and AET), and Precipitation (P), to assess the hydrologic behavior of a location under a given climatic condition by plotting the Evaporative Index (EI, AET/P)

against the Dryness Index (DI, PET/P). For values $HSi \geq 1$: Sensitive and $HSi < 1$: Resilient. We also point out whether the sensitive areas resulted in a decrease or increase in water yield and warmer vs cooler climate conditions. Also, since elevation, slope, and aspect are the three defining factors in temperature and humidity regimes, we evaluate their influence on HSi. Moreover, the variables used for computing HSi are evaluated against in-site measurement to confirm the use of high-quality datasets throughout the entire study. Next, we document critical thresholds of deforestation in 45 regions that underwent extensive forest cover loss induced by either drought, fire, or clear-cutting during the 2001-2016 period and report if these trends lead to increasing or decreasing water yield and warmer or cooler climate conditions (Chapter 3). HSi is used in this study to evaluate departures in historic hydrologic behavior in the face of land cover disturbances such as tree cover loss using 3-year HSi averages of before and after-disturbance periods. The Hydrologic Sensitive Area (HSia) was obtained by computing the portion of the area with high HSi values (HSi>1) relative to the entire disturbed area. We identified the critical threshold in forest cover loss before hydrologic responses are detected and the speed at which the disturbed area attains complete sensitivity once this threshold is surpassed, while also detecting if the observed changes in hydrologic regime increase or decrease water yield and if they are accompanied by warmer or cooler climate conditions. Lastly, we document the most hydrologically sensitive ecoregions to tree cover loss within the Amazon basin by reporting the differences in response in HSia to the most recent extreme drought events (Amazon drought in 2005, 2010, and 2015) while exploring the underlying factors leading to such responses.

Chapter 1: Global Analysis of the Hydrologic Sensitivity to Climate Variability

Abstract

Identifying the regions with the greatest changes in their hydrologic behavior under extreme weather events in the 21st century constitutes a study priority of global impact. Here, we present a global assessment assessing the sensitivity of the world's water landscapes to climate variability during 2001-2016, using a new metric called the Hydrologic Sensitivity Index (HSi). This equation is based on the well-known Budyko curve that uses annual values of Potential and Actual Evapotranspiration (PET and AET), and Precipitation (P), to assess the hydrologic behavior of a location under a given climatic condition by plotting the Evaporative Index (AET/P) against the Dryness Index (PET/P). For values $HSi \geq 1$: Sensitive and $HSi < 1$: Resilient. Also, since elevation, slope, and aspect are the three o defining factors in temperature and humidity regimes, we evaluate their influence on HSi. Overall, the majority of the world's biomes display a tendency toward a drier state. Particularly, we identify the regions with hydrologic sensitivity to climate variability in tropical rainforests accompanied by decreasing water yields and warmer/drier conditions evident along the southernmost part of the Amazon the and central part of the Congo basin. High sensitivity is also seen along easternmost Canadian and Eurasian arctic tundra and boreal forests with increasing water yield trends and dominant warmer/drier climate conditions. The hydrologic sensitivity is amplified at high elevations and steep-sloped terrain outlining the importance of the topography in modulating these effects. We direct the attention towards climate warming resulting in decreased forest cover as a potential mechanism driving the decreasing water yield patterns in tropical zones, while snowmelt and increasing precipitation in the tundra and boreal forests result in surplus water yields. Our global study highlights the particular locations with the greatest hydrologic changes to climate

variability while outlining the main water yield and climate directions—a study that indicates where water resources have been changing the greatest and in what ways.

1.1 Background

Global warming and human interventions are changing the behavior of Earth's water cycle (Stott, 2016, Easterling et al., 2017, Sterling et al, 2013, Rodell et al., 2018, Tabari, 2020). Although there is evidence that extreme weather events and increasing climatic variability are intensifying hydrologic processes worldwide (Held & Soden, 2006, Milly et al., 2015, Huntingon, 2006, Tabari, 2020, Creed et al., 2014), there is still no consensus on the direction or the magnitude in which different components of the water cycle will respond in the world's major terrestrial ecosystems under these imposed changes (Stott, 2016, Zhan et al., 2012, Salmoral et al., 2015, Martens et al., 2018, Padron et al., 2017). As the current human population arrives at a critical environmental carrying capacity, and the world enters a warmer climate, our planet's ecosystems are changing and adapting (Seddon et al., 2016, Pecl et al., 2017), bringing along changes in the way water is partitioned in the landscape (Milly et al., 2005; Held & Soden, 2006; Huntington 2006; Creed et al., 2014; Tabari, 2020). Whether natural or human-induced, ecosystems' alterations to the water cycle at the global scale need to be urgently assessed. Particularly in the face of increasing climate variability and the rising numbers and intensity of extreme weather events altering hydrologic processes worldwide (Stott, 2016; Milly et al., 2005; Zhan et al., 2012). Thus, looking at variations in hydrologic response as a function of the variability in climatic forcing offers an opportunity to detect regions where hydrologic dynamics are changing (Gao et al., 2016). Furthermore, identifying locations with changing hydrologic responses to climatic variability is important for detecting regions arriving at critical thresholds that may compromise the availability of water for both ecosystems and human settlements.

1.2 Concept of Elasticity

Assessing the hydrologic sensitivity to climate variability can be approached from the concept of elasticity. Elasticity here is defined as the capacity of a system to keep a consistent response in spite of sudden perturbations, and/or extreme climatic variability (i.e. hydrologic resilience; Creed et al., 2014). Thus, in that sense, hydrologic sensitivity is the inverse of elasticity and can be used to detect regions with unstable hydrologic systems. The elasticity concept has been devised using the well-known and widely used Budyko's curve (Creed et al., 2014, Roderick et al., 2014, Helman et al., 2017, Sinha et al., 2018, Padron et al.,2017), which provides a reference condition on the behavior of the long term mean water balance as a function of the average climatic condition of an area (Trenberth, 2011, Roderick et al., 2014, Helman et al., 2017, Li et al., 2019, Budyko, 1974, Greve et al., 2016) (Figure 1). It uses annual values of Potential and Actual Evapotranspiration (PET and AET respectively), and Precipitation (P) and examines changes in the Evaporative Index (i.e. hydrologic response, EI=AET/P) against changes in the Dryness Index (i.e. climate condition, DI; PET/P) over defined periods of time. Simply put, Budyko's curve represents the historical average of multiple catchments across varying climate types. Therefore, a region's EI can be obtained along the curve given information on its climate (DI). Thus, elasticity (*e*) is quantified by how far the EI deviates from Budyko's curve relative to the change in DI defined as the ratio between the range of the dryness index (ΔDI) and that of the evaporative index relative to the curve (ΔEI_R) (Creed et al., 2014) (Equation 1). Positive deviation (+ΔEI, more AET) indicates less water yield (-Q, water left over on Earth's surface after evaporation has taken place) while negative deviation (-ΔEI, less AET) indicates greater water yield (+Q) (Figure 1). A catchment has high elasticity when there is a small deviation in EI_R relative to a change in DI ($e > 1 = \Delta DI > \Delta EI_R$, resilient) and low elasticity when a great deviation of EI_R occurs relative to DI ($e < 1 = s\ \Delta DI < \Delta EI_R$, sensitive).

$$e = \frac{\Delta DI}{\Delta EI_R} = \frac{\Delta DI}{\Delta(EI-B)} \cdot \quad (1)$$

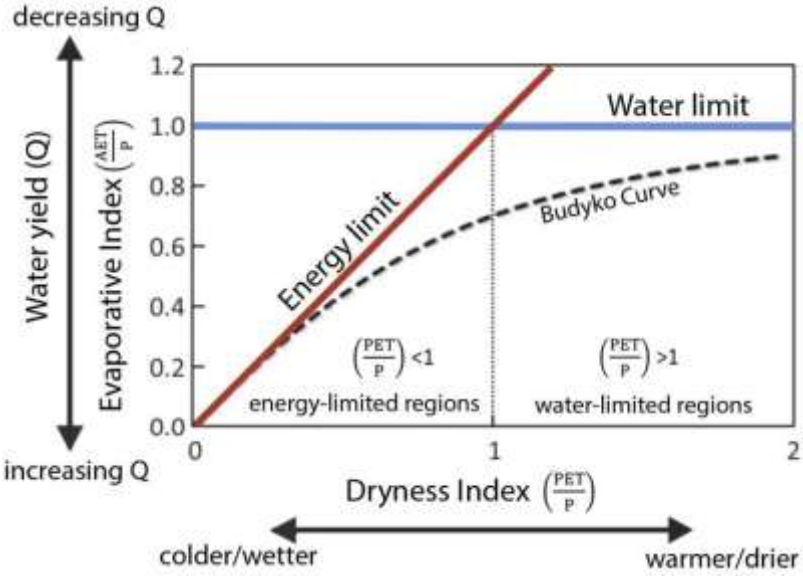

Figure 1: Budyko's Framework. The framework plots the evaporative index against the dryness index. When the evaporative index increases (decreases) the water yield decreases (increases). The solid lines represent the energy (red) and water limit (blue) lines, and the dashed line represents the historical average of where regions would plot given information on their climate (known as the original Budyko curve) (Creed et al., 2014, Budyko, 1974) .

1.3 Novelty of this global assessment

Although previous studies have documented regions undergoing hydrological changes using the concept of elasticity for showing how varying climate and the intensification of human activities can have a strong influence on year-to-year changes in hydrologic responses, (Wu et al, 2017b, Creed et al., 2014, Helman, 2017, Li et al., 2019, Wu et al., 2017), they have only been assessed in a few catchments within geographically limited regions. Because of this limited geographic extent, other important factors known to modulate climatic variabilities, such as elevation, slope, and aspect, have been obviated. For example, elevation and aspect in complex terrain alter temperature and humidity regimes across different land conditions within similar climatic zones. Elevation leads to changes in temperature and precipitation regimes which are further amplified by slope and aspect creating distinct microclimates (Gutiérrez-Jurado et al.,

2006, Sristava et al., 2020). Together, these factors influence the partitioning of water in the landscape and hence its hydrologic response over time (Gutiérrez-Jurado et al., 2007), raising questions about which of them plays a major role in maintaining a consistent hydrologic behavior in spite of large climatic perturbations (e.g. climatic deviations from the normal). Changes to hydrologic functioning in response to climatic perturbations are expected to vary widely according to land cover conditions, topographic complexity of the terrain and geographic location (Sterling et al., 2013), specifically in places where sensitive characteristics to these perturbations are relevant. Thus, it is important to evaluate the hydrologic responses to climatic variability globally, and to assess the recurrence (frequency) of heightened responses, while evaluating the role of terrain properties in locations where relatively minor perturbations result in significant changes in hydrologic functioning.

In this study, we evaluate the hydrologic responses to climatic variability globally, and assess the frequency of these responses, while evaluating the role of major topographic factors in modulating these responses. Given that different biomes (climate types) have unique characteristics and the way they respond to extreme climate forcing is inextricably linked to how it will affect water resources (Padron et al., 2017, Motew & Kucharick, 2013, Gudmunsson et al., 2016), we explore the resulting hydrologic sensitive areas for each of the different terrestrial biomes in the world. Finally, we document the average direction in which hydrologic changes occur in these sensitive areas, noting if these regions are shifting to drier (+ΔDI) or wetter state (-ΔDI) and if they are yielding more (-ΔEI) or less (+ΔEI) water.

2. Methods

2.1 Data Collection

We use annual values of the 3 key variables (AET, PET and P) for the period of January

2001 to December 2016 due to the availability of datasets. The main characteristics **(**i.e. component, product, temporal resolution, spatial resolution) of the satellite products used are listed in Table 1. AET is derived from Penman-Monteith Leuning version 2 (PML-V2) at 500m resolution (Zhang et al., 2019). The PML_V2 product performs well against observations at 95 flux sites across the globe and is similar to or noticeably better than major state-of-the-art AET products such as PML-V1, MOD16, and GLEAM (Zhang et al., 2019). PET is derived from the Moderate-Resolution Imaging Spectroradiometer (MOD16A2) version 6 onboard the Terra satellite and produced at 500m resolution (Running et al., 2019). It has been validated over 46 eddy flux towers, and the close agreement in the seasonality between data reveals the reasonability (magnitude, range and directions of variations) for valid pixels (Running et al., 2019). P is derived from the Multi-Source Weighted-Ensemble Precipitation dataset (MSWEPv2) at 0.1-degree resolution (Beck et al., 2019a). This dataset, MSWEPv2, combines gauge and satellite products, with multiple corrections for regional differences and has shown to be a robust dataset when compared to other P products with a high spatial resolution (Beck et al., 2019b) is (≤0.1°,) which include Climate Hazards Group Infrared Precipitation with Stations (CHIRPS; 0.05°), CPC morphing technique (CMORPH; 0.07°), Global Satellite Mapping of Precipitation (GSMaP; 0.1°), Integrated Multi satellite Retrievals for Global Precipitation Measurement (IMERG; 0.1°), and Precipitation Estimation from Remotely Sensed Information Using Artificial Neural Networks–Cloud Classification System (PERSIANN-CCS; 0.04°). Overall, the three products used in this study have been tested worldwide and span a variety of climates and land cover types providing the opportunity to apply these datasets for studies of global terrestrial water and energy cycles and environmental changes.

Table 1: Data Collection. List of products with temporal and spatial resolution used to evaluate HSi.

Variable	Product	Temporal resolution	Spatial resolution	Reference
AET (April 4, 2002-present)	**PML-V2** (Penman-Monteith-Leuning Version 2)	8-day	**500m**	Zhang et al.(2019)
PET (2001-present) AET(2001)	**MODIS** (MOD16A2.006 Modeling Imaging Spectroradiometer)	8-day	**500m**	https://doi.org/10.5067/MODIS/MOD16A2.006
P (1979-Oct. 2017)	**MSWEP-v2** (Multi-Source Weighted Ensemble Precipitation Dataset Version 2)	Daily	**0.1**◦ (11,100m)	Beck et al. (2019)
DEM Digital Elevation Models **(Elevation, Aspect, & Slope)**	**SRTM & GTOPO30** (Global 30-arc Second Elevation >60◦ N) (Shuttle Radar Topographic Mission 90m <60◦ N)	GTOPO30:1996 SRTM:2008	GTOPO30:**1**◦ (~1000m) SRTM:**90m**	http://lta.cr.usgs.gov/GTOPO30

2.1.1 Testing the quality of the hydrologic datasets

We selected as many in-situ measurement for each variable (AET, PET, and P) from Ameriflux with more than 4 years of continuous data during 2001-2016 period and compare them to our satellite data. The Ameriflux is a network of in-situ instrumentation measuring ecosystem CO_2, water, and energy fluxes in North, Central and South America (Novick et al., 2018). It was established to connect research on field sites representing major climate and ecological biomes, including tundra, grasslands, savanna, crops, and conifer, deciduous, and tropical forests. The daily data available was added to compute annual values of AET and P. Values of PET was not a direct flux tower measurement and had to be computed with 11 parameters identified in Ameriflux dataset (See Appendix Equation A1).The following charts display the correlation coefficient (R^2), regression coefficient ($y=\mathbf{B_1}x+B_0$), where B_1=slope or relationship between variables, and the Nash-Sutcliffe efficiency coefficient (NSH) for annual values of AET, PET, and P between satellite product and in-situ Ameriflux data. These 3 variables test the relationship between variables where values close to 1 indicate high correlation. For

P, there is a clear positive correlation between datasets with a R^2=0.71, B_1= 0.875, and NSH=0.69. For PET, R^2=0.72, y=0.875, and NSH=-.69. For AET, R^2 = 0.61, B_1=0.99, and NSH=0.61. These results indicate that the satellite datasets chosen (PML-v2 for AET, MSWEP-v2 for P, and MODIS for PET) are suitable for large-scale spatial analysis. Also, HSi was computed using in-situ measurements and compared to satellite-based HSi with a resulting correlation coefficient of R^2=0.69 across 30 sites.

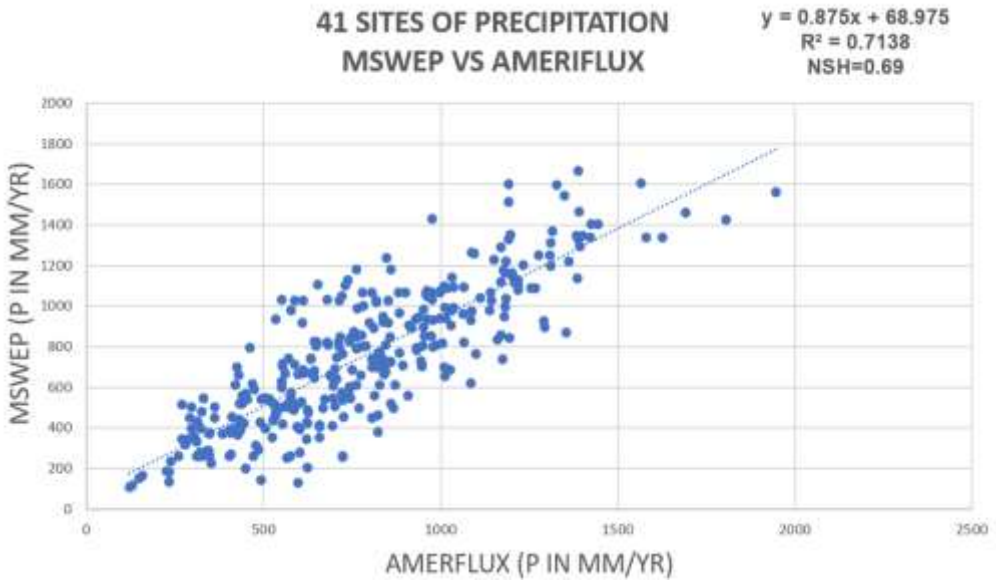

a)

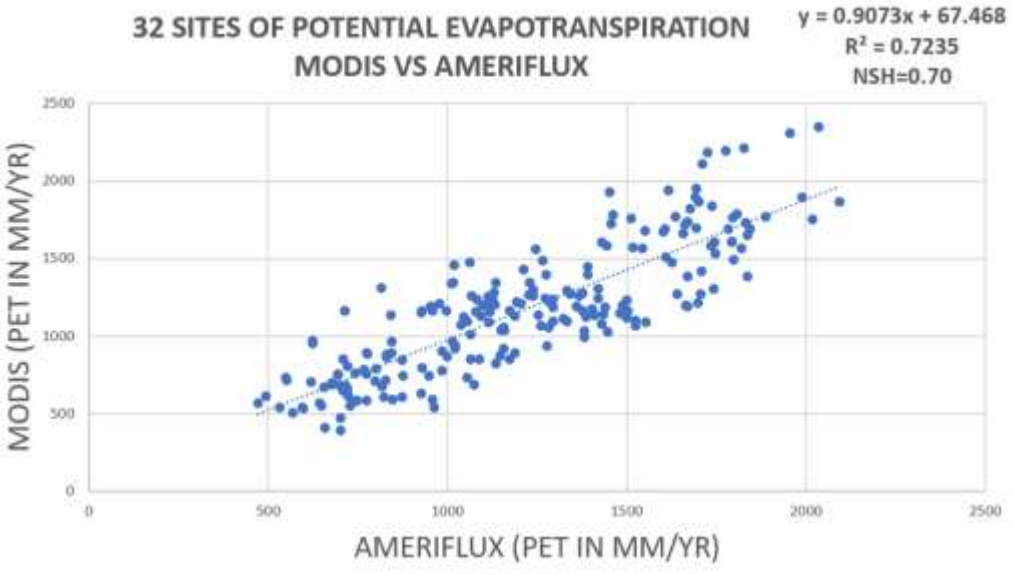

b)

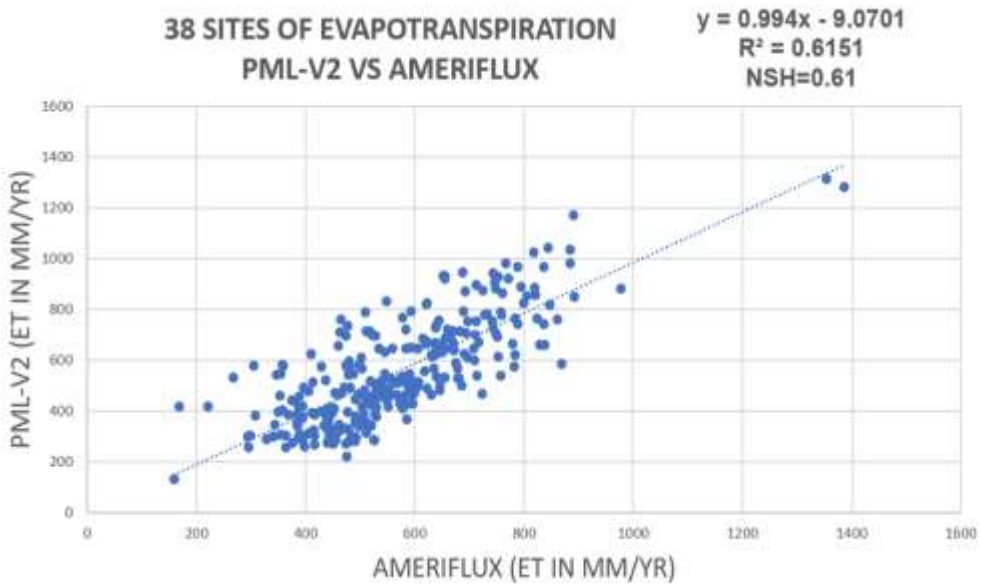

c)

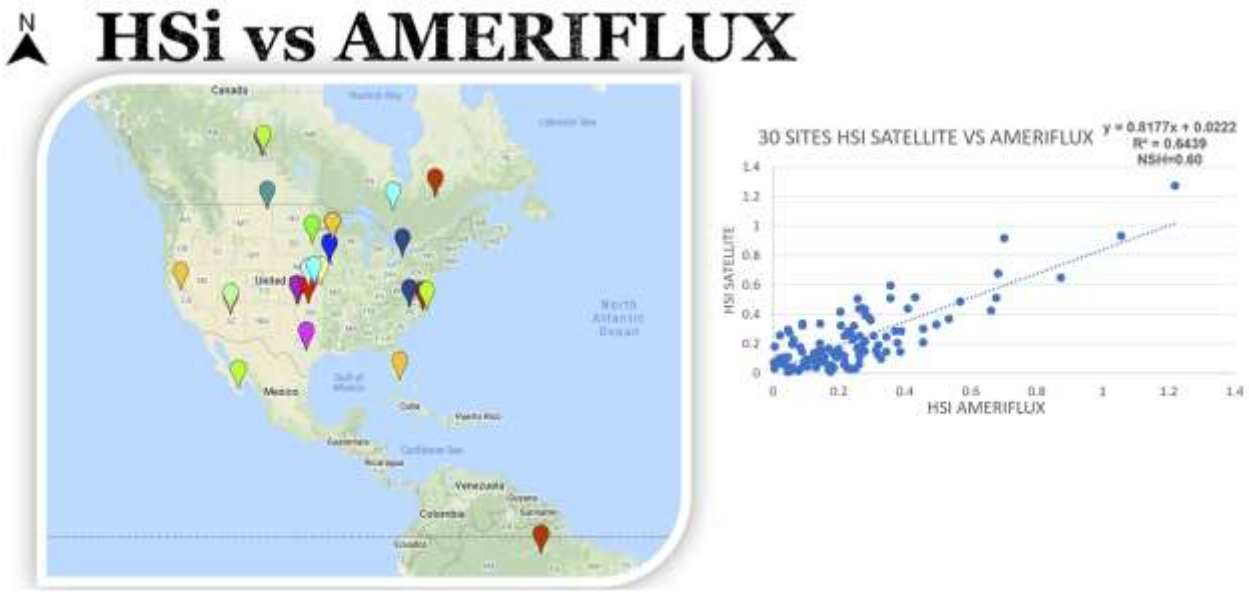

d)

Figure 1.1 a-d: Correlation test of satellite datasets with in-situ measurements. Comparison between MSWEP-V2, MODIS, and PMLV-2 against Ameriflux data where a) P, b) PET, and c) AET, and d) HSia are compared, respectively.

2.2 A new metric: Hydrologic Sensitivity Index

This study focuses on identifying regions that are most sensitive or are likely change to an alternative or permanent state in hydrologic functioning. Thus, we developed a new metric called the Hydrologic Sensitivity Index (HSi) by taking the inverse of the elasticity formulation.

However, since Budyko's framework is limited to steady-state conditions (Greve et al., 2016) and this study is executed at an interannual scale, Budyko's formulation needs an adjustment**.** Specifically, at sub-annual and interannual timescales, changes in storage water terms such as soil moisture, groundwater, snow storage, or human interventions result in AET>P (additional water other than P) does not characterize steady-state conditions (Greve et al., 2016). Consequently, we apply the adapted Budyko formulation presented by Greve et al., 2016 to account for changes in storage (B_A) (Equation 2a and Figure 2) using the parameter y_0, which represents a measure of the maximum amount of additional water besides P being available to AET (Equation 2b). This parameter is calculated as the difference between AET and P (only when AET-P >0) normalized by PET. The parameter *k* is a free model constant that can be interpreted as a factor other than the aridity index that influences the water partitioning of EI and was determined to be $\kappa = 2.6$ corresponding to the best fit to the original Budyko function However since this parameter varies by region it must be estimated (Greve et al., 2016).

$$B_A = \frac{AET}{P} = 1 + \left(\frac{PET}{P}\right) - \left(1 + (1 - y_0)^{k-1} * \left(\frac{PET}{P}\right)^k\right)^{\frac{1}{k}}, \tag{2a}$$

$$\text{where } y_0 = \frac{AET - P}{PET}, \; if \; AET - P > 0 \tag{2b}$$

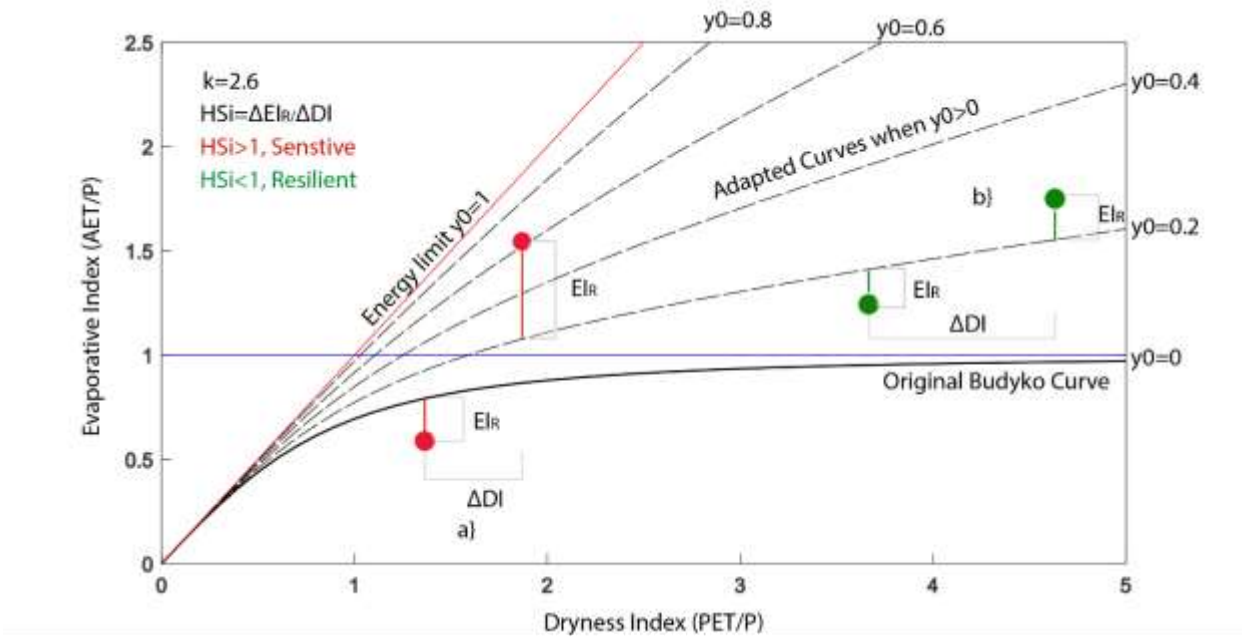

Figure 2: Adapted Budyko Curve. The Budyko framework accounts for changes in storage for regions where AET-P>0, so the range in EI_R is in reference to the adjusted curve, while the range in DI is not affected. HSi is calculated as the ratio of a catchment's range in EI to its range in DI between consecutive pair of years.. HSi= $(\Delta DI)/(\Delta EI_R)$, where a) high sensitivity (HSi > 1, red) (i.e., approximating theoretical behavior), and (b) low hydrologic sensitivity (HSi<0, green) (i.e., deviating from theoretical behavior).

Hence, by tracking the changes in hydrologic response (ΔEI_R) of a location or region relative to the adapted curve (B_A), that is, its water yield deviation to interannual climatic variability (ΔDI) for consecutive years, we can calculate the hydrologic sensitivity in the following manner:

$$HSi = \frac{\Delta EIR}{\Delta DI} = \left|\frac{\Delta(EI_R - B_A)}{\Delta DI}\right|, \quad (3)$$

where sensitive regions will display HSi>1, and resilient locations will show HSi <1 (Equation 3). It is important to note that HSi evaluates the absolute difference between DI and EI_R between successive years, regardless of which year was warmest or wettest. A conceptual diagram depicting the algorithm used is shown in Figure 2, of which a detailed description is provided next. HSi evaluates the absolute ratio between ranges in DI and EI_R values between consecutive years (e.g. HSi $= |\Delta EI_R/\Delta DI| = |\Delta EI_{R,2001-2002}/\Delta DI_{2001-2002}|$.

2.3 Computing HSi

Knowing the year-to-year hydrologic sensitivity is more meaningful when looking over a longer period of time. Regions consistently showing sensitive behavior can be identified by looking at the frequency with which HSi >1 is detected. Figure 3 displays the algorithm for computing HSi frequency. First, we compute annual values of AET, PET, P, and y_0. Next, we compute HSi for every successive pair of years from 2001 to 2016. All computations leading to the HSi are performed in the Google Earth Engine Platform (Golerick et al., 2017). A total of 15 HSi maps were obtained representing the HSi for each consecutive pair of years. For each map, where HSi >1, regions are classified as ***Sensitive,*** and for HSi ≤1, ***Resilient***. To provide a synthesis of the general trend of global hydrologic sensitivity, we display the frequency of HSi, showing the recurrence of HSi >1 for every terrestrial location with a range of 0 (low frequency) to 15 (high frequency). Regions where frequency HSi ≥7 are considered highly recurring and as such are deemed as the most hydrologically sensitive.

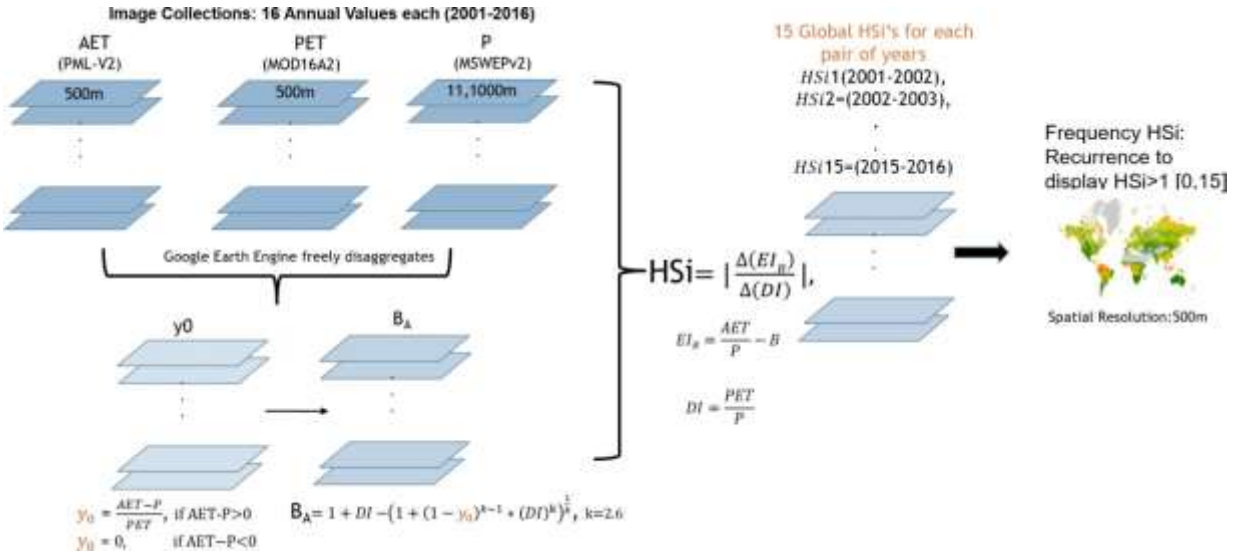

Figure 3: HSi Algorithm. Flowchart for computing HSi. Input data layers are shown in medium blue, intermediate data layers computed in Google Earth Engine as part of the algorithm are shown in light blue, and final output is displayed as a map of HSi Frequency.

2.4 Computing Mean Sensitive Area

Besides the geographic occurrence of hydrologic sensitive areas, identifying the percentage of sensitive areas relative to the total area in a biome can help inform the regions of the world where the hydrologic response has been consistently changing. Figure 4 displays the algorithm for estimating the mean hydrologic sensitive area for each terrestrial biome. For this analysis, the biome boundaries were obtained from Terrestrial Ecosystems of the World (TEOW) shapefiles (Figure 5) by the World Wildlife Fund (Olson et al., 2001). The 15 pairs of ΔEI_R's and

ΔDI's per biome are used to quantify sensitivity for every consecutive pair of years. Hydrologic-sensitive areas are represented by the colored quadrants (green and red or light and dark blue). All colored area shows that the interannual absolute change in the evaporative index, $|\Delta EI|$, is greater than the interannual absolute change in the dryness index, $|\Delta DI|$ which is equivalent to $|HSi|>1$. The diagram is split into 4 quadrants indicating the possible climate and water yield directions: drier ($+\Delta DI$) wetter ($-\Delta DI$) and less water yield ($+\Delta EI$) and more water yield ($-\Delta EI$). Sensitive area (grid cells) where $|HSi|>1 = |\Delta EIR|>|\Delta DI|$ equivalent to:

$I = \Delta EI_R > \Delta DI$ = less water yield and drier climate;

$II = \Delta EI_R > -\Delta DI$ = less water yield and wetter climate;

$III = -\Delta EI_R < -\Delta DI$ = more water yield and wetter climate;

$IV = \Delta EI_R < \Delta DI$ = more water yield and drier climate.

Sensitive area is defined by the percentage of sensitive grid cells ($HSi>1$) to the total number of grid cells within each biome. Once we obtain all 15 values (one per pair of years) of sensitive area per biome, we compute the temporal average. Additionally, we display sensitive areas with the direction of change by including the portion of the sensitive area allocated toward drier vs wetter climate conditions (Figure 4a) and less vs greater water yield (Figure 4b) and

direction of change. For instance, the percentage of sensitive grid values toward warmer/drier (ΔDI) and colder/wetter (-ΔDI) values define the climate direction, while decreasing (ΔEI) and increasing (-ΔEI) water yield define the water yield direction. Also, the fraction of the sensitive area is plotted relative to the global land area to provide a global areal extent of sensitivity for each biome. In addition, we created two maps to spatially display the median climate and water yield trends for regions with HSi>1 and Frequency ≥7.

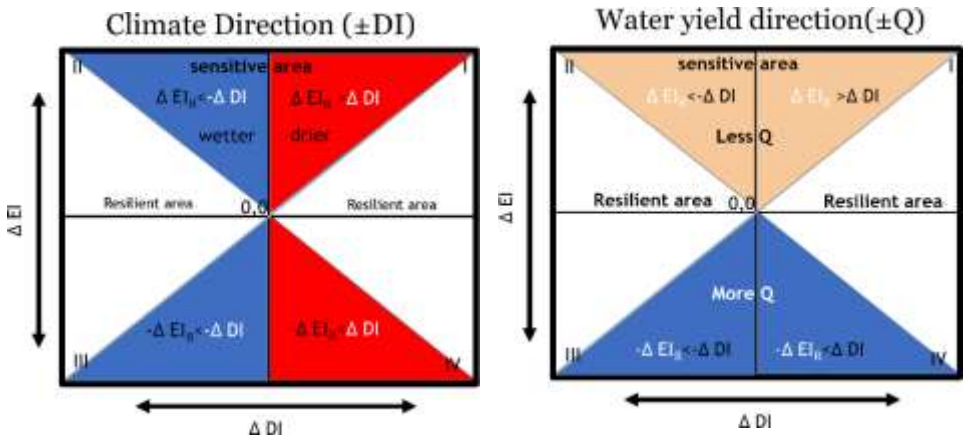

Figure 4: Mean Hydrologic Sensitive Area Concept. The diagrams show how the hydrologically sensitive area is calculated**. a)** Quadrant 1 and IV where hydrologic sensitive areas have become drier (red), so that the change in +ΔDI is positive, while in quadrant II and III represents the areas which have become wetter the absolute change in -ΔDI is negative (green). **b)** Quadrant I and II represent the condition where hydrologic sensitive areas show decreasing water yield trends, so that the change in $+\Delta EI_R$ is positive (light blue), while quadrants III and IV represent the areas that show increasing water yield trends so that the change in $-\Delta EI_R$ is negative (dark blue).

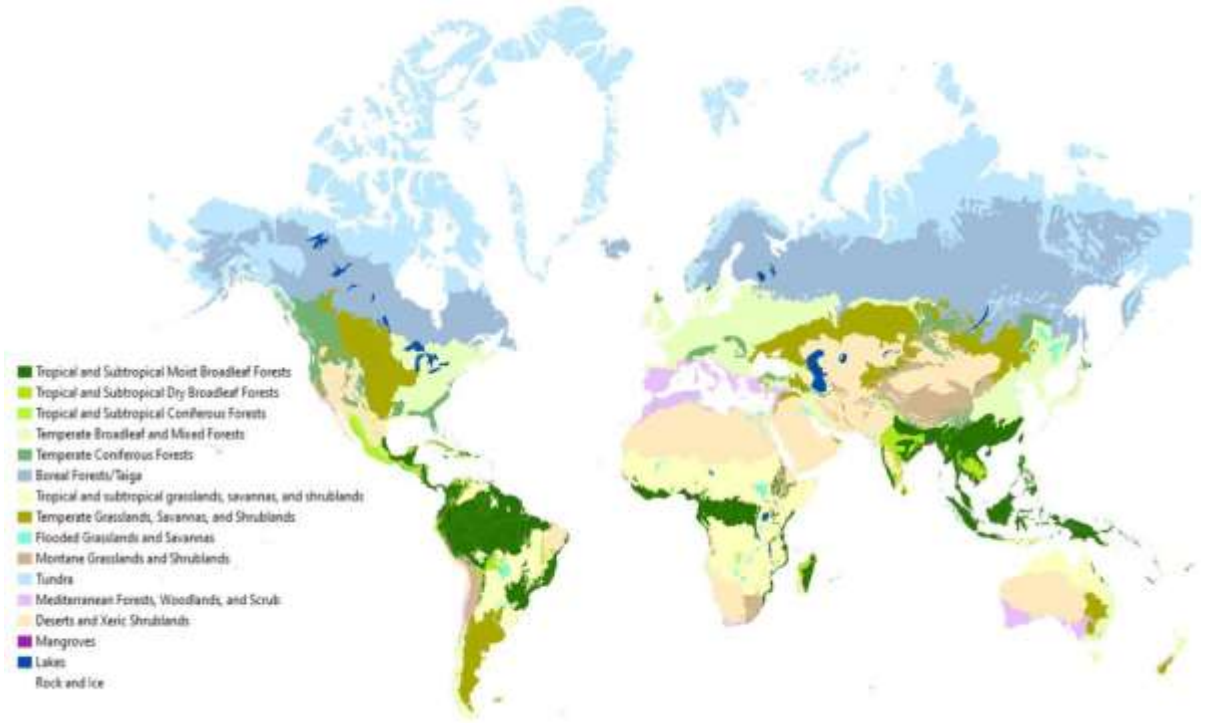

Figure 5: Global Terrestrial Ecosystems. A total of 14 Major Terrestrial Ecosystems reflect the diverse climate types (we do not consider lakes and rock ice biomes for this study). Terrestrial communities represented here include the full extent of continental topographic relief (Oslon, 2001).

2.5 Computing the effect of elevation, slope, and aspect

We evaluate the effect of topography on hydrologic sensitivity by plotting the average HSi frequency for all elevation ranges (binned every 100 m), aspects (binned every 22.5°), and slope steepness (binned every 5°) against latitudinal change. For this analysis, we used global digital elevation models (DEMS) from the Shuttle Radar Topography Mission (SRTM, Jarvis et al., 2008) data (90 m resolution; version 4, for latitudes < 60◦ N and GTOPO30 (1◦ resolution; http://lta.cr.usgs.gov/GTOPO30) for latitudes > 60◦ N as seen in Table 1. Slope and aspect maps were derived from the DEMs using standard GIS-based methods in ArcMap 10.7. (Burrough et al., 2015). The elevation range used is 0 to7000 meters above sea level (m.a.s.l), aspect (N, NE, E, SE, S, SW, W, NW) specifically above slope values greater than 10° (no flat areas used), and slope 0 to 90 degree.

3. Results

3.1 Average annual excess water used from storage (y_0) (i.e., groundwater-dependent ecosystems)

We note that water storage was used to supplement precipitation to satisfy the annual AET ($y_0>0$; Figure 6), except in locations where "no data" values in either AET or PET impeded the calculation of y_0 (gray areas in Figure 6). In particular, high values ($y_0>0.2$) occur along the Yucatan Peninsula (y_0~0.3-0.4, Mexico), California (y_0~0.30-0.35, USA) a,nd Great plains (y_0~0.25, USA), Patagonia (y_0~0.28-0.41, Argentina), Tamil Nadu and Rajasthan (y_0~0.3-0.4 India), Caatinga forest (y_0~ 0.26-0.38, Brazil) and Eastern Africa (y_0~0.40-0.65). Some of these regions showing large y_0 values correspond to groundwater-fed irrigated croplands where significant abstraction of water resources subsidizes high AET rates (e.g. Central Valley, California and Central Midwestern USA, Northern India, Northeastern China; Aeschbach-Hertig & Gleeson, 2012). Other areas with large y_0 values show groundwater-dependent ecosystems where vegetation has continual access to water regardless of precipitation conditions yielding high annual AET (e.g. Yucatan Peninsula; Uuh-Sonda et al., 2018). Other regions along the high Artic tundra, northernmost boreal zones, and equatorial tropical zones display no excess storage (y_0~0), while all other regions have slight excess water storage (y_0>0-0.20) (see Figure 6).

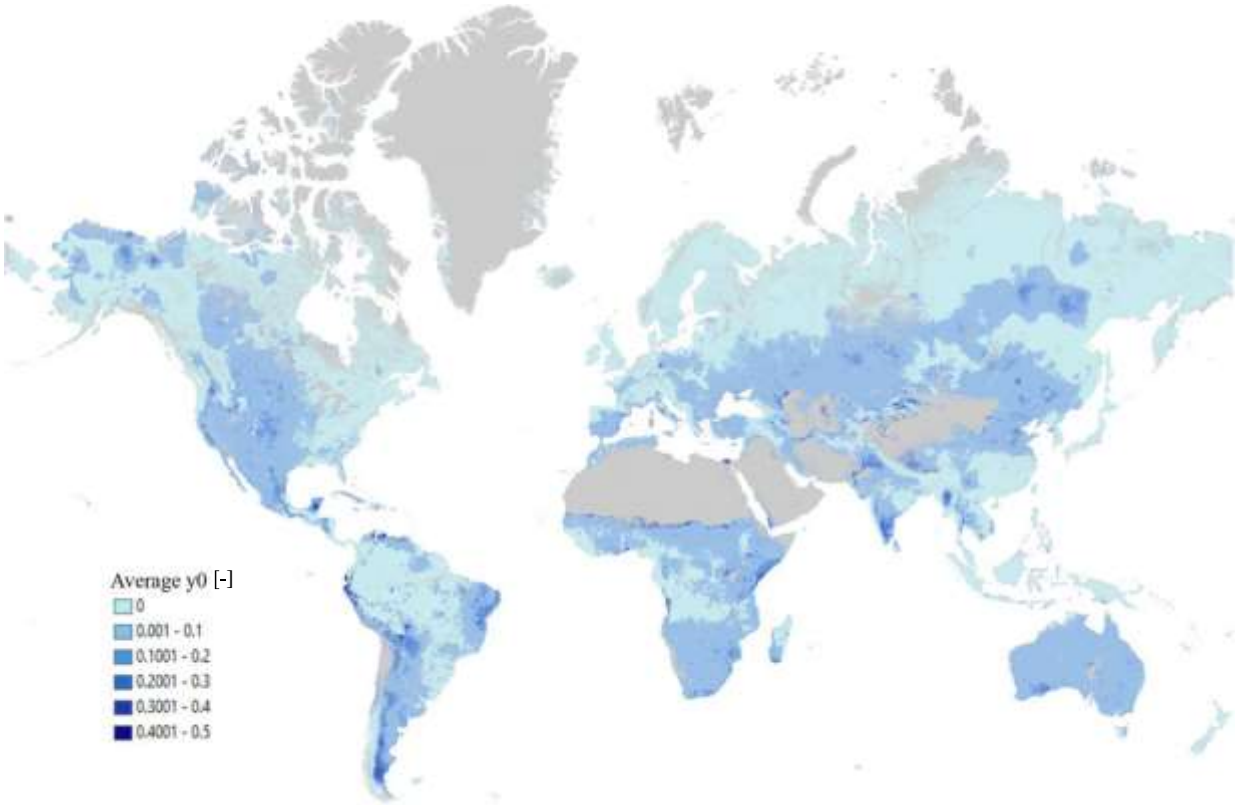

Figure 6: Average excess water used from storage. 16-year average excess water storage as a fraction of the potential evapotranspiration (additional water other than P available to AET standardized by PET). The values range from 0 (no significant changes in storage) to 0.4 or greater (red, high changes in storage). Areas with dominant barren land and permanent ice (no data) are shown in grey. Pixel resolution is 500m. Map created in Google Earth Engine and modified with continental outline shapefile in ArcGIS 10.7 software.

3.2 Frequency HSi

The areas exhibiting the most frequent hydrologic sensitivity during the 2001-2016 period were located in the tropical rainforests (tropical & subtropical moist broadleaf forest) of Central and South America (Amazon Basin), central-western Africa (Congo Basin), and southeast Asia (Himalayan region, Indochinese Peninsula, and the Malay Archipelago), the Arctic tundra, parts of the boreal forest, and tropical and subtropical coniferous forests scattered throughout North America and Eurasia (Figure 7). Overall, arid and semiarid areas worldwide display low frequency (<2) of HSi, and the areas displaying the highest frequency (>7) are in general surrounded by a zone of increasingly lower HSi frequency (orange and yellow areas in Figure 7) outwards.

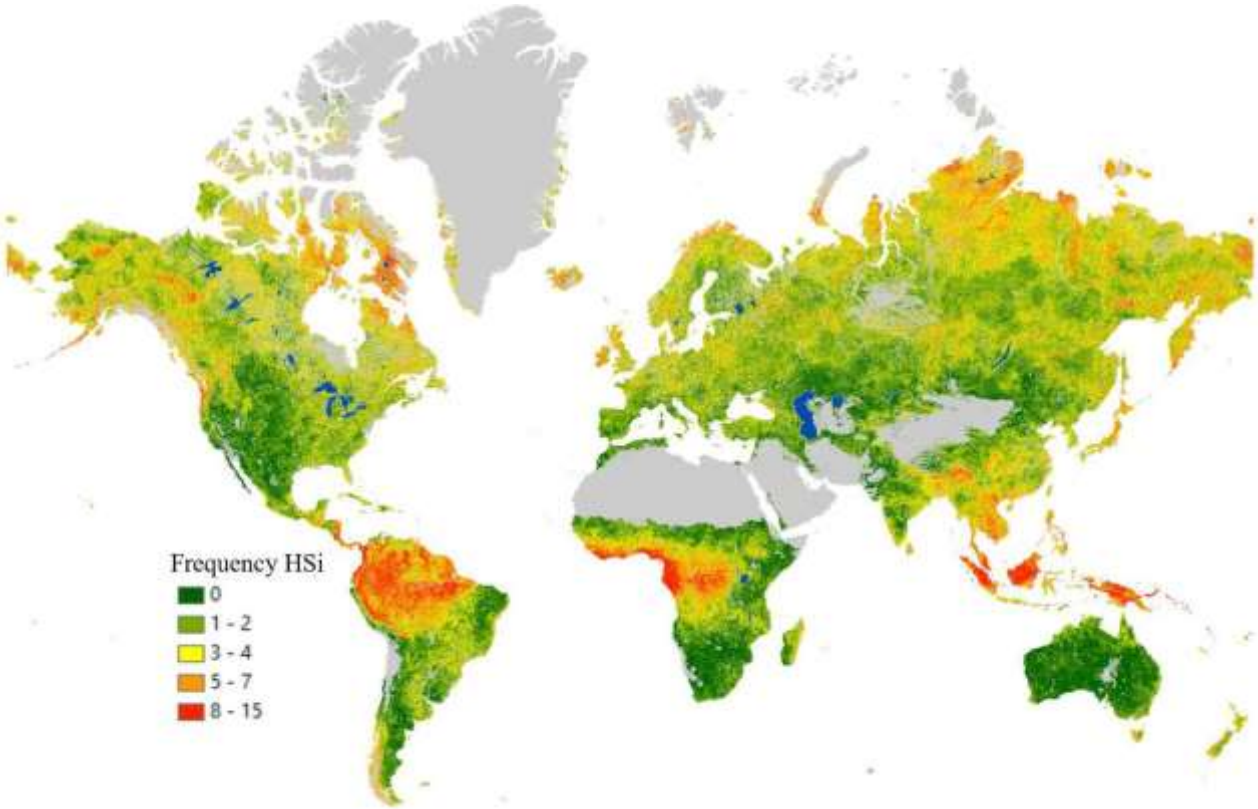

Figure 7: Frequency of Hydrologic Sensitivity. Tendency to high hydrologic response to climate variability (based on the recurrence of HSi ≥1). The index ranges from 0 (no frequency, dark green) to 15 (high frequency, red). Areas with dominant barren land and permanent ice (no data) are shown in grey. Wetland areas, as identified by the Global Lakes and Wetlands Database, are mapped in blue. Pixel resolution, 500m; period, 2001–2016. Map created in Google Earth Engine and modified with continental outline shapefile in ArcGIS 10.7 software

The areas where no hydrologic sensitivity is detected during the period of study (2001-2016) are regions with large interannual variability in climatic conditions. A map showing the coefficient of variation (CV) of the Dryness Index (DI) reveals that the regions of the world where this coefficient is large (values close to 1 show locations with high variability) closely match those with no hydrologic sensitivity (0 frequency of HSi >1; Figure 8. a). In those places, the interannual variability of the DI outweighs any moderate or even large variabilities in Evaporative Index (EI; Figure 8. b). By contrast, the areas where the highest frequency of hydrologic sensitivity is observed, correspond to locations with low or moderate interannual variability in DI and EI (i.e. CV of DI and EI < 0.4). This suggests that hydrologic sensitivity, as measured by HSi, is largely dependent on the prevailing interannual variability of the fluctuations in climatic conditions

expressed by the DI. This finding gives confidence in the ability of the HSi to detect those locations where in spite of having low year-to-year variations in climatic conditions, relatively large variations in the evaporative index are occurring.

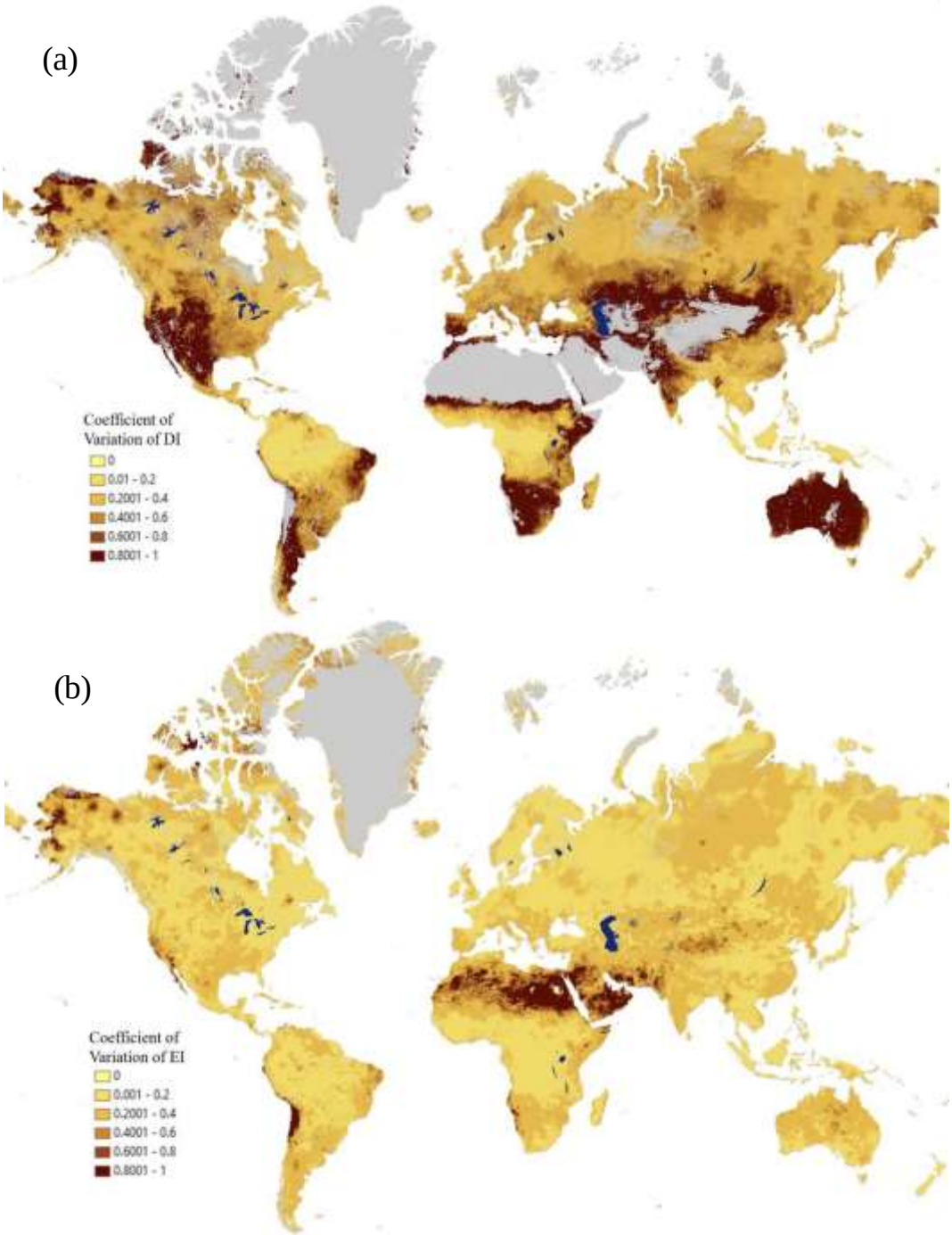

Figure 8. Coefficient of Variation of (a) Dryness Index (DI) and (b) Evaporative Index (EI) for the study period (2001-2016). The coefficient ranges from 0 (low variability, light yellow) to 1 (high variability, red). Areas with dominant sterile soil and permanent ice (no data) are shown in gray. Wetland areas, identified by Global Lakes and Wetlands Database, are mapped in blue. Pixel resolution is 500m. Map created in Google Earth Engine and modified

to include continental schema basemap and lakes in ArcGIS 10.7 software.

3.3 Mean sensitive area per biome w/climate and water yield direction

Figure 9 displays the mean sensitive area per biome arranged from largest to least hydrologic sensitive. The biomes displaying the largest sensitive area in descending order are tropical rainforests, the Arctic tundra, tropical and subtropical coniferous forests, and boreal forests. Tropical and subtropical rainforests and coniferous forests display decreasing water yields, while tundra and boreal systems display increasing water yields. Relative to global land, boreal forests have the greatest actual areal extent of hydrologic sensitive land followed by tropical rainforests and grasslands (tropical and subtropical grassland, savannas, and shrublands). The hydrologic-sensitive area in the majority of the biomes (12 out of 14 biomes) has a clear tendency towards decreasing water yield conditions with the exception of the Arctic tundra and temperate broadleaf mixed forests (mixed forests) which display a neutral behavior. Although the climate direction is roughly neutral for most biomes, the hydrologic sensitive area in 9 out of 14 biomes is slightly inclined toward drier conditions with the exception of the Arctic tundra, mixed forests, temperate coniferous forests, tropical & subtropical coniferous forests, and tropical rainforests, which lean toward wetter/colder conditions.

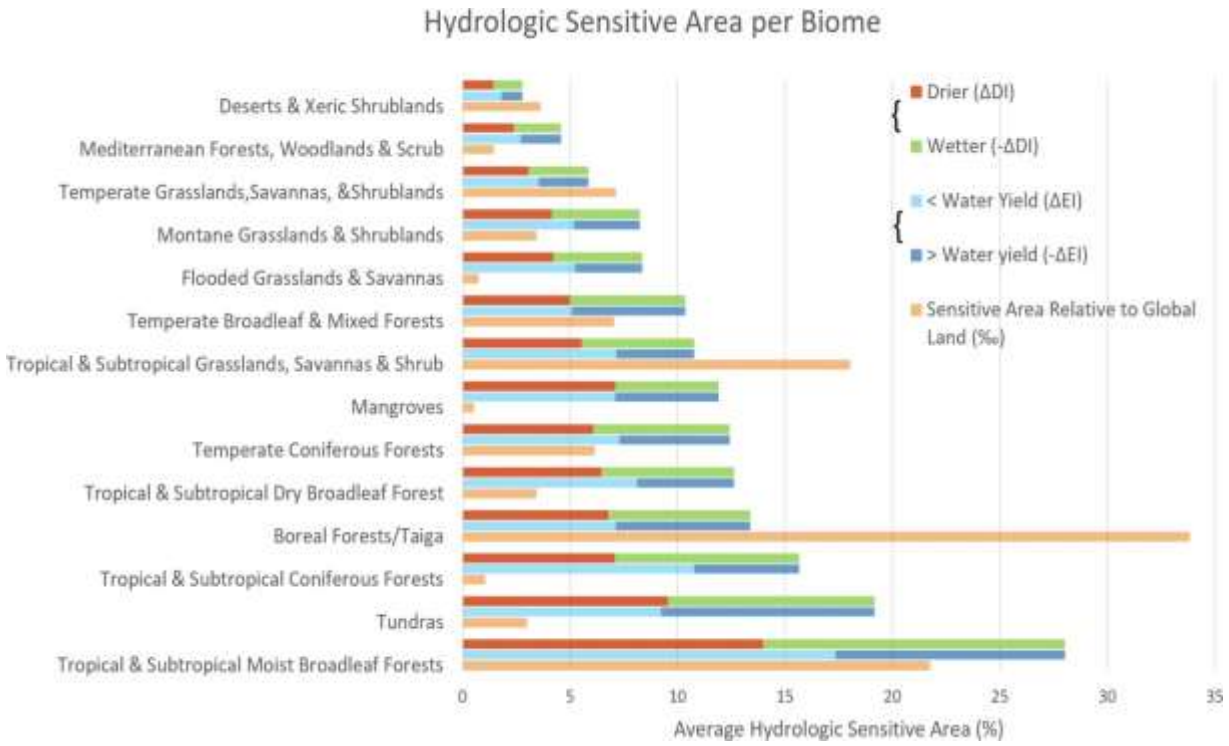

Figure 9: Hydrologic Sensitive Area. Average sensitive area per biome (relative to biome area) with portion indicating direction of change, where drier (red) and wetter (green) conditions refer to the climate direction; less (light blue) and greater water yield (dark blue) refers to the hydrologic direction; average sensitive area relative to the global land area (orange) refers actual extent of sensitivity. Values are computed on Google Earth Engine platform at ~1000m resolution.

3.4 Water yield and climate direction for regions with high HSi frequency

Focusing on only those regions where HSi frequency >7 (mainly equatorial and northern high latitudes) the median direction in water yield (ΔEI) and climate direction (ΔDI) is displayed in Figure 10 and Figure 11 respectively. In particular, Figure 10 displays dominant decreasing water yield (light orange) for the majority of pixels within the tropical forest (equatorial zones) while increasing water yields (blue) are evident in the northern high latitude regions, particularly along Alaskan, easternmost Canadian and Eurasian arctic regions and boreal forests. Figure 11 displays a general neutral tendency in climate conditions in dry (red) versus wet (blue) for these same regions. Nonetheless, the map displays drying/warmer conditions along the southern part of and the southern edge of the Amazon basin, the western and central Congo Basin, and the northeastern part of the Canadian and Eurasian

continents. Colder/wetter conditions are seen along the northern part of the Amazon basin and northmost Siberia.

Figure 10: Water yield direction of hydrologically sensitive regions. For display purposes, observed results are based on median values of interannual change in evaporative index, ΔEI, only for regions where the frequency of HSi≥7. The values range from less water yield (+ΔEI, light orange) to greater water yield (-ΔEI, dark blue) conditions. Areas with dominant sterile soil and permanent ice (No Data) and non-sensitive areas are shown in gray. Pixel resolution is 500m. Map created in Google Earth Engine and modified to include continental schema basemap in ArcGIS 10.7 software.

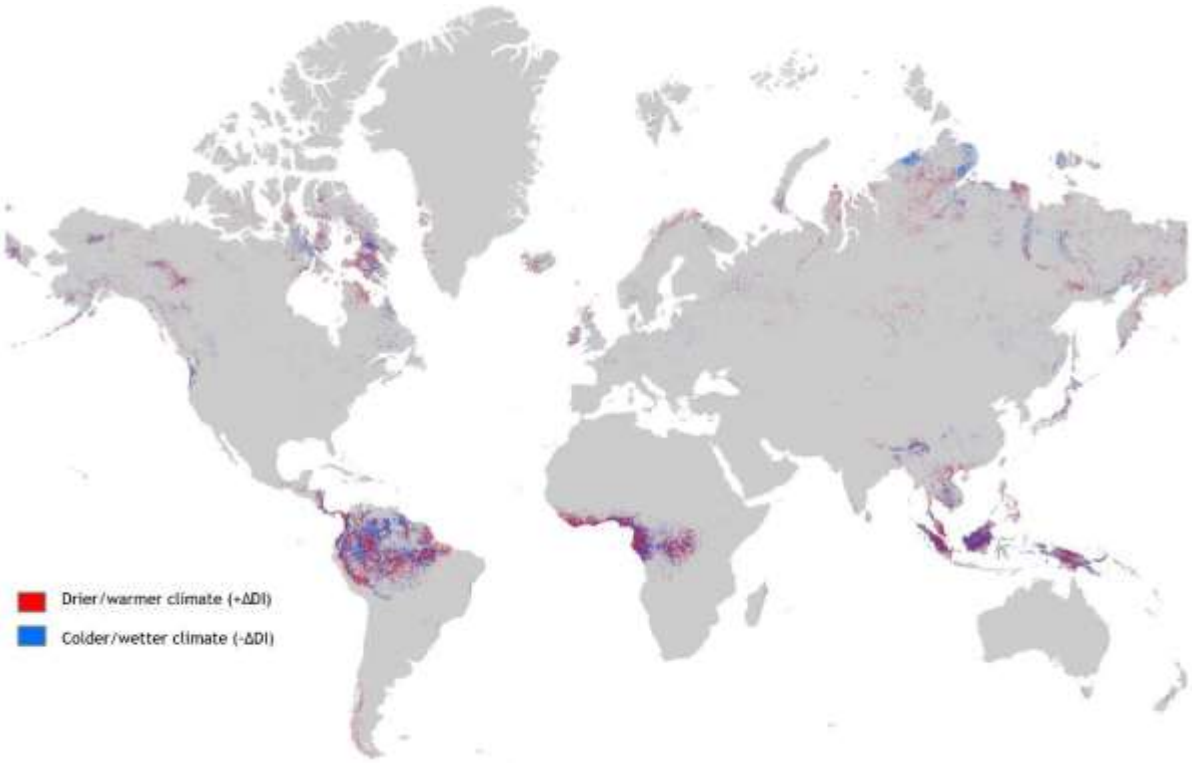

Figure 11: Climatic direction of hydrologically sensitive regions. For displaying purposes observed results are based on median values of interannual change in dryness index, ΔDI, only for regions where the frequency of HSi≥7. The index ranges from colder/wetter (-ΔDI, blue) to drier/warmer (+ΔDI, red) climate conditions. Areas with dominant sterile soil and permanent ice (no data) and non-sensitive areas are shown in gray. Pixel resolution is 500m. Map created in Google Earth Engine and modified to include continental schema base map in ArcGIS 10.7 software.

3.5 Effect of topographic parameters on HSi

The topographic effects on hydrologic sensitive areas are most apparent along high latitude regions, particularly at mountainous locations in both hemispheres, including the Tibetan Plateau (33°N) as seen in Figure 12a-c. For example, in Figure 12a elevation appears to be a defining parameter driving hydrologic sensitivity beyond 45° latitudes in both the Northern and Southern hemispheres. Conversely, midlatitude regions (between 20° and 40°) in both South and North hemispheres appear to be somewhat hydrologically insensitive to changes in elevation, but most markedly and for a larger latitudinal stretch in the Southern hemisphere. The latitudinal stretch in the Northern Hemisphere where HSi values are low across all elevation ranges is 5°shorter than in the Southern Hemisphere (20° to 40° vs -30° to -45° respectively). Along

the equatorial belt, in between 15° S and 7° N, high HSi values appear at the lowlands (0-500 m.a.s.l) and above ~1500 m.a.s.l throughout all the elevation ranges, with the highest sensitivity above 2000 m.a.s.l. In the same latitudes, where high HSi is found across elevation gradients, steep slopes (slopes greater than 30°) display high HSi values in Figure 11b, mainly attributed to the various effects of mountainous landscapes that are generally associated with having steep-sloped topography compared to low elevations (Riebe et al., 2015). Along the equatorial zone (~7°N and ~10°S) high HSi values are found at the majority of slope angles but with the highest sensitivity at slopes greater than 15°. In the Northern hemisphere, HSi gradually increases beginning at latitude 45° and beyond, but has specific thin latitudinal stretches (~2°) of higher sensitivity at slopes greater than 30° around 50°, 60°, 70°, and 80°. In the Southern hemisphere, HSi increases abruptly at higher latitudes beginning at -40° and beyond with the highest sensitivity for very steep slopes (slope>60 °). HSi in regions between latitudes of -20° and -40° (location of arid lands) appear to be insensitive at all slope angles and elevations. In our analysis, the aspect (orientation of the terrain) did not show an effect on HSi (Figure 12c). This is possibly due to the inability of the HSi data to capture the fine-scale microclimatic variability in areas with complex terrain due to the native spatial resolution of the data (>500m). There is evidence that varying aspects in complex terrain modulate the hydrologic response to extreme hydroclimatic events (Gutiérrez-Jurado et al., 2007) and could potentially amplify or mute the HSi of headwater catchments constituting some of the largest inland water-yielding areas. Further studies addressing this shortcoming in the analysis with the use of higher-resolution data, should provide a clearer picture of the impact of terrain attributes on the HSi of these regions.

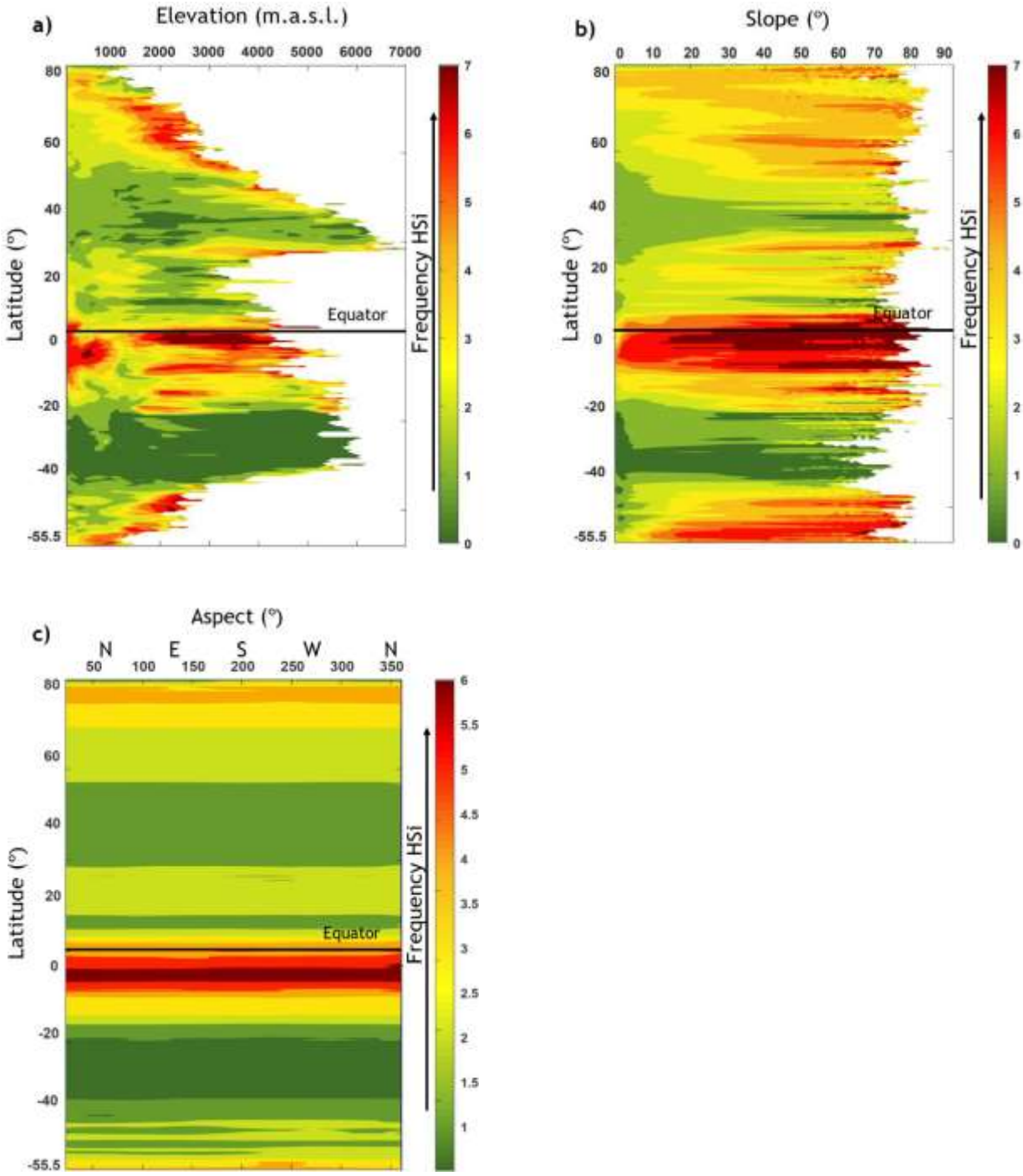

Figure 12: Frequency HSi [0,7+] at varying values of **a) elevation** [100,7000] in m.a.s.l. **b) slope steepness** [0,90] in degrees, and **c) aspect**[0,359**]** in degrees against latitudinal change from 80N to -55.5S from low frequency (blue) to high frequency (red). Graphs created in MATLAB 2019 software using pixel resolution at 90m for each variable.

4. Discussion

4. Discussion

In this study we showed a global map displaying excess storage water. These regions agree with locations of some of the world's groundwater-dependent ecosystems and groundwater-fed irrigated croplands (Rodell et al., 2018, Aeschbach-Herring & Gleeson, 2012). Regions displaying no excess water storage such as northern high latitude regions and equatorial tropical zones are mostly explained by being energy-limited regions and receiving large amounts of precipitation resulting in larger moisture influxes relative to evapotranspiration outfluxes. The relatively simple computation of y_0 can provide the first insight into out-of-water-balance areas that can alter the estimates of hydrologic sensitivity by raising AET totals substantially at the annual scale. Our analyses indicate that the majority of the regions detected as hydrologic sensitive areas are changing towards drier conditions with decreasing water yields. This observation coincides with a phenomenon suggested by Cook et al., (2014), in which vast regions of land on the planet are experiencing at least moderate drying as a warmer climate—generally more able to evaporate moisture from the land surface– in combination with hotter temperatures will favor increasing dryness.

Our results showed that the locations with the highest HSi can be clustered in two regions: (1) tropical zones across all elevation ranges (2) along arctic tundra and boreal zones. For the first region, at equatorial latitudes, we found hydrologic sensitivity in tropical rainforests associated with changing water yields. A majority of tropical regions show decreasing water yields while fewer regions show increasing trends (Figure 8). There is still no consensus as to whether reduced forest cover will increase or decrease water yields across these regions (Bruijinzeel et al., 2004, Zhoue et al., 2013, Roudier et al., 2014, Reyer et al., 2017, Deb et al., 2018). Reduced forest cover, which has shown to alter precipitation patterns (Ellison et al., 2011, van der Ent et

al., 2010) resulting in reductions in leaf gas exchanges (Seddon et al., 2016, Clark et al., 2003, Staal et al., 2018, Wu et al., 2019) along these regions is a potential explanation to the observed reductions in water yields. Placed in a large-scale context, a great portion of tropical forests' rainfall is water recycled within these basins by forest evapotranspiration (van der Ent et al., 2010, Lenton et al., 2008). For instance, approximately one-third of rainfall in the Amazon (Staal et al., 2018, van der Ent et al., 2010, Lenton et al., 2008), Congo (van der Ent et al., 2010, Dyer et al., 2017), and northern Indonesia and Papua New Guinea basins is regional recycled precipitation (van der Ent et al., 2010). Hence, a reduction in tropical forest cover leads to decreases in forest evapotranspiration which in turn results in reduced precipitation. Consequently, reduced regional recycled precipitation at large scales implies a tendency toward decreasing water yields. This highlights the hydrologic sensitivity of tropical regions to forest cover changes. Continuing deforestation and human land use and disturbances at the continental scale, currently highest in this terrestrial biome (Crowther et al., 2015), have the potential to amplify the negative impact observed in water yields (Davidson et al., 2012). In contrast, regions south of Indonesia and Papua New Guinea where ocean moisture is the main precipitation source, show the areas where forest cover loss is accompanied by increasing water yield trends (van der Ent et al., 2010). In addition, there is evidence that regional recycling ratios are amplified in mountainous regions globally since these areas are able to block moisture from entering continents or easily capture moisture from the atmosphere (van der Ent et al., 2010). Accelerating vegetation changes involving biodiversity loss and reduction of tropical alpine areas (Buytaert et al., 2011) is therefore a plausible cause for decreased water yields within these regions.

For the second region, at high latitudes, in the past three decades, temperatures have increased rapidly, mainly in the northern hemisphere (Hartmann et al, 2013). As a consequence, rapid rates of snow melt have been observed in Arctic tundra and boreal forests in response to

warming temperatures (López-Moreno et al., 2020, Najafi et al., 2015, Pepin et al., 2015, Myers-Smith et al., 2015, Lamprecht et al., 2015). These regions are warming more rapidly than lower latitudes due to polar amplification of temperature, water vapour, and surface albedo feedbacks (Myers-Smith et al., 2015, Chapin et al., 2005, Hinzman et al., 2013). There is also evidence that this effect is enhanced at high-elevation regions where snow accumulation is greatest and changes in precipitation patterns are occurring (e.g regions in the Tibetan Plateau, Rocky Mountains, Greater Alpine Region) (Pepin et al., 2015, Ohmura, 2012, Zhang et al., 2013, Yan et al., 2016, Palazzi et al., 2019). For example, recent findings have shown increases in lake levels and volumes in the Tibetan Plateau related to temperature amplification resulting in enhanced precipitation from a faster warming rate compared to the mean global warming (Zhang et al., 2020). Also, high latitude and mountainous regions of Siberian and Canadian Arctic and boreal zones have seen increasing water yield trends due to ice-sheet loss, increasing precipitation, thawing, and shrub growth in steep slopes (Rodell et al., 2018, Myers-Smith et al., 2015, Zhang et al., 2013). These lines of evidence are consistent with our findings of high HSi areas leaning toward higher water yields in these regions, particularly those along the Siberian and easternmost Canadian and Eurasian Arctic.

5. Conclusions

We identified regions with hydrologic sensitivity to climate variability globally and at high spatial and temporal resolution within high and low latitudes. At high latitudes, boreal and arctic zones show heightened hydrologic sensitivity accompanied by increasing water yields, while at low latitudes, tropical rainforests show the largest hydrologic sensitivity with the majority of their sensitive area trending towards decreasing water yields. We found that hydrologic sensitivity is amplified at high elevations and in steep-sloped terrain, outlining the importance of topography in modulating these effects with strong implications for high water-yielding headwater catchments. We direct the attention toward climate warming resulting in increasing snow melt and precipitation in Arctic tundra and boreal forests and increasing tree cover loss in tropical forests, as possible mechanisms driving the observed patterns. Although there is no clear consensus yet on the direction surface water yields would take in tropical zones as a result of climate variability, our findings suggest that hydrologic sensitivity may be linked to vegetation changes. Other land cover changes associated with altered climatic patterns across high-latitude regions may be contributing to changing hydrologic dynamics (Myers-Smith et al., 2015) in areas displayed in our HSi analysis as highly sensitive locations. Globally, boreal and tropical forests, the two biomes producing the greatest water yields also display the greatest extent of hydrologic sensitive land. This makes them hotspots for hydrologic surveillance of expected impacts from further increases in climatic shifts with the potential to significantly alter the global water cycle. Future work should determine if the hydrologic sensitivity patterns found in this study represent tipping points in changing hydrologic dynamics within each biome, and assess at the regional and local scale their cascading impacts on ecosystems and human settlements.

Code Availability

Code and datasets used to conduct this analysis are available online from our Google Earth

Engine link https://code.earthengine.google.com/9efbe6a3ccfb488eef80a903d923a30f. A MATLAB code and associated data to reproduce the topographic analyses is available for download in the following open access repository: http://doi.org/10.5281/zenodo.4479716.

Author Information

Marisol Domínguez and Hugo A. Gutiérrez-Jurado: These authors contributed equally to this work.

Marisol Domínguez-Tuda

Present address: Department of Earth, Environmental, and Resource Sciences, University of Texas at El Paso, Texas, United States

Hugo A. Gutiérrez-Jurado

Present address: Department of Earth, Environmental, and Resource Sciences, University of Texas at El Paso, Texas, United States

Contributions

H.A.G. conceived and designed the study. M.D. prepared and processed the data including writing the Google Earth scripts. Both M.D. and H.A.G performed the data analysis, writing and editing of the paper.

Corresponding Author

Correspondence to M. Domínguez and H. A. Gutiérrez-Jurado

Ethics Declaration

The authors declare no competing interests.

Additional Information

Marisol Dominguez, & Hugo A. Gutiérrez-Jurado. (2021). Global dataset for evaluating impact of topographic factors on hydrologic response to climate variability (Version 1) [Data set]. Zenodo. http://doi.org/10.5281/zenodo.4479716

Acknowledgments

M.D. acknowledges funding from a National Science Foundation Graduate Research Fellowship Award #1848741, H.A.G. acknowledges funding from a Rising Stars Award from the University of Texas System and a DECRA Award #DE150101981 from the Australian Research Council.

References

Aeschbach-Hertig, W., & Gleeson, T. (2012). Regional strategies for the accelerating global

problem of groundwater depletion. *Nat. Geosci.*, 5 (12), 853-861.

Beck, H. E., et al (2019a). MSWEP V2 global 3-hourly 0.1 precipitation: methodology and quantitative assessment. *Bull. Am. Meteorol. Soc*. 100.3, 473-500.

Beck, H. E. et al. (2019b). Daily evaluation of 26 precipitation datasets using Stage-IV gauge-radar data for the CONUS. *Hydrol. and Earth Syst. Sci*, 23(1), 207-224.

Bruijnzeel, L. A. (2004). Hydrological functions of tropical forests: not seeing the soil for the trees? *Agric. Ecosyst. Environ.*, 104(1), 185-228.

Budyko, M. I. (1974). Climate and life. *New York: Academic Press.*

Burrough, P. A. et al. *Principles of Geographical Information Systems*. (Oxford university press, New York, 2015).

Buytaert, W. et al. (2011). Potential impacts of climate change on the environmental services of humid tropical alpine regions. *Glob. Ecol. and Biogeogr*., 20(1), 19-33.

Chapin, F. S. et al. (2005). Role of land-surface changes in Arctic summer warming. *Science*, 310, 657–660.

Clark, D. A. et al. (2003). Tropical rain forest tree growth and atmospheric carbon dynamics linked to interannual temperature variation during 1984–2000. Proceedings of the national academy of sciences, 100(10), 5852-5857.

Cook, B. I. et al. (2014). Global warming and 21st century drying. *Clim. Dyn*., 43(9-10), 2607-2627.

Creed, I. et al. (2014). Changing forest water yields in response to climate warming: Results from long-term experimental watershed sites across North America. *Glob. Chang. Biol*, 20 (10), 3191-3208.

Crowther, T. et al. (2015) Mapping tree-density at global scale. *Nature*. 525,201-205.

Davidson, E. et al. (2012). The Amazon basin in transition. *Nature* 481, 321–328.
Deb, J. C. et al. (2018). Climate change impacts on tropical forests: identifying risks for tropical Asia. J. *Trop. For. Sci.*, 30(2), 182-194.

Dyer, E. L. et al. (2017). Congo Basin precipitation: Assessing seasonality, regional interactions, and sources of moisture. *J. Geophys. Res. Atmos.*, 122(13), 6882-6898.

Easterling, D.R. et al. Precipitation change in the United States. in: *Climate Science Special Report*: *Fourth National Climate Assessment, Volume I* (eds. Wuebbles, D.J., D.W. Fahey, K.A.

Hibbard, D.J. Dokken, B.C. Stewart, and T.K. Maycock) 207-230 (U.S. Global Change Research Program, Washington, D.C., 2017).

Ellison, D.N. et al. (2012). On the forest cover–water yield debate: from demand-to supply-side thinking. *Glob. Change Biol.*, 18(3), 806-820.

Gao, G. et al. (2016). Determining the hydrological responses to climate variability and land use/cover change in the Loess Plateau with the Budyko framework. *Sci. Total Environ.*, 557, 331-342.

Giorgi, F. et al. (2011). Higher hydroclimatic intensity with global warming. *J.Clim*. 24(20), 5309-5324.

Gorelick, N. et al. (2017). Google Earth Engine: planetary-scale geospatial analysis for everyone. *Remote Sens. Environ*. 202, 18–27.

Greve, P. et al. (2016). A two-parameter Budyko function to represent conditions under which evapotranspiration exceeds precipitation. *Hydrol. Earth Syst. Sci.*, 20(6), 2195-2205.

Gudmundsson, L. et al. (2016).The sensitivity of water availability to changes in the aridity index and other factors—A probabilistic analysis in the Budyko space, *Geophys. Res. Lett.*, 43, 6985–6994.

Gutiérrez-Jurado, H. A. et al. (2006). Ecohydrology of root zone water fluxes and soil development in complex semiarid rangelands. *Hydrol. Process*., 20(15), 3289-3316.

Gutiérrez-Jurado, H.A., et al. (2007). Ecohydrological response to a geomorphically significant flood event in a semiarid catchment with contrasting ecosystems. *Geophys.Res.Lett*., 34(24).

Gutiérrez-Jurado. et al. (2013). On the observed ecohydrologic dynamics of a semiarid basin with aspect-delimited ecosystems. *Water Resour. Res*., 49(12), 8263-8284.

Hartmann, D. L.et al. Observations: Atmosphere and Surface. in *Climate change 2013 The Physical Science Basis: Working Group I Contribution to the Fifth Assessment Report of the Intergovernmental Panel on Climate Change: Volume 9781107057999* 159-254 (Cambridge University Press, Cambridge, 2013).

Held, I. M., & Soden, B. J. (2006). Robust responses of the hydrological cycle to global warming. *J. Clim.*, 19(21), 5686-5699.

Helman, D., et al. (2017). Forests growing under dry conditions have higher hydrological resilience to drought than do more humid forests. *Glob. Change Biol.*, 23(7), 2801-2817.

Hinzman, L. D. et al. (2013). Trajectory of the Arctic as an integrated system. *Ecol. Appl.*, 23(8), 1837-1868.

Huntington, T. G. (2006). Evidence for intensification of the global water cycle: review and synthesis. *J. Hydrol.*, 319(1-4), 83-95.

Jarvis, A. et al. (2008). Hole-filled SRTM for the Globe Version 4. *available from the CGIAR-CSI SRTM 90m Database (http://srtm.csi.cgiar.org)*, 15, 25-54

Lamprecht, A. et al. (2018). Climate change leads to accelerated transformation of high-elevation vegetation in the central Alps. *New Phytol.*, 220(2), 447-459.

Lenton, T. M. et al. (2008). Tipping elements in the Earth's climate system. *Proc. Natl Acad. Sci.*, 105(6), 1786-1793.

Li, C.et al. (2019). Larger increases in more extreme local precipitation events as climate warms. *Geophys. Res. Lett.*, 46(12), 6885-6891.

López-Moreno, J. I., et al. (2010). Decoupling of warming mountain snowpacks from hydrological regimes. *Environ. Res. Lett.*, 15(11), 114006.

Martens, B. et al. (2018). Terrestrial evaporation response to modes of climate variability. *NPJ Clim. Atmos. Science*, 1(1), 1-7.

Milly, P. C. et al. (2005). Global pattern of trends in streamflow and water availability in a changing climate. *Nature*, 438(7066), 347-350.

Motew, M. M., & Kucharik, C. J. (2013). Climate-induced changes in biome distribution, NPP, and hydrology in the Upper Midwest US: A case study for potential vegetation. J. *Geophys. Res. Biogeosci.*, 118(1), 248-264.

Myers-Smith, I. H. et al. (2015). Climate sensitivity of shrub growth across the tundra biome. *Nat. Clim. Change*, 5(9), 887-891.

Najafi, M. R. et al. (2015). Attribution of Arctic temperature change to greenhouse-gas and aerosol influences. *Nat.Clim. Change*, 5(3), 246-249.

Novick, K. A., et. al. (2018). The AmeriFlux network: A coalition of the willing. *Agricultural and Forest Meteorology*, *249*, 444-456.

Ohmura, A. (2012). Enhanced temperature variability in high-altitude climate change. *Theor. Appl. Climatol.*, 110(4), 499-508.

Olson, D. M. et al. (2001). Terrestrial ecoregions of the world: a new map of life on Earth. *Bioscience* 51(11):933-938.

Palazzi, E., et al. (2019). Elevation-dependent warming in global climate model simulations at high spatial resolution. *Clim. Dyn.*, 52(5-6), 2685-2702

Padron, R. S., et al. (2017). Large Scale controls of the surface water balance over land: Insights from a systematic review and meta-analysis. *Wat. Resour. Res.*, 53, 9659– 9678.

Pecl, G. T. et al. (2017). Biodiversity redistribution under climate change: Impacts on ecosystems and human well-being. *Science*, 355(6332).

Pepin, N. et al. (2015). Elevation-dependent warming in mountainous regions of the world. *Nat. Clim. Change*, 5, 424-430.

Reyer, C.P. et al. (2017). Climate change impacts in Latin America and the Caribbean and their implications for development. *Reg. Environ. Change*, 17.6, 1601-1621.

Riebe, C. S. et al. (2015). Climate and topography control the size and flux of sediment produced on steep mountain slopes. *Proc. Natl. Acad. Sci.*, 112(51), 15574-15579.

Risser, M. D., & Wehner, M. F. (2017). Attributable human-induced changes in the likelihood and magnitude of the observed extreme precipitation during Hurricane Harvey. *Geophys. Res. Lett*., 44.

Rodell, M. et al. (2018). Emerging Trends in Global Freshwater. *Nature*, 557, 651–659.

Roderick, M. L., F. et al. (2014). A general framework for understanding the response of the water cycle to global warming over land and ocean, *Hydrol. Earth Syst. Sci.*, 18(5), 1575–1589.

Roudier, P. et al. (2014). Climate change impacts on runoff in West Africa: a review. *Hydrol. Earth Syst. Sci.*, 18, 2789-3801.

Running, S. et al. (2017). MOD16A2 MODIS/Terra Net Evapotranspiration 8-Day L4 Global 500 m SIN Grid V006. NASA EOSDIS Land Processes DAAC.

Salmoral, G. et al. (2015). Drivers influencing streamflow changes in the Upper Turia basin, Spain. *Sci. Total Environ.*, 503, 258-268.

Seddon, A.W.R. et al. (2016). Sensitivity of Global Terrestrial Ecosystems to Climate Variability, *Nature*, 531, 229–232.

Siler, N. et al. (2018). Insights into the zonal-mean response of the hydrologic cycle to global warming from a diffusive energy balance model. *J. Clim.*, 31(18), 7481-7493.

Sinha, J. et al. (2018). Assessment of the impacts of climatic variability and anthropogenic stress on hydrologic resilience to warming shifts in Peninsular India. *Sci. Rep.*, 8(1), 1-14.

Staal, A. et al. (2018). Forest-rainfall cascades buffer against drought across Amazon. *Nat. Clim. Change.*, 8, 539–543.

Sterling, S. M. et al. (2013). The impact of global land-cover change on the terrestrial water cycle. *Nat. Clim. Change*, 3(4), 385.

Srivastava, A. et al. (2020). The Role of Landscape Morphology on Soil Moisture Variability in Semi-arid Ecosystems. *Hydrol. Process.*

Stott, P. (2016).How climate change affects extreme weather events. *Science*, 352(6293), 1517-1518

Tabari, H. (2020). Climate change impact on flood and extreme precipitation increases with water availability. *Sci. Rep.*, 10(1), 1-10.

Reyer, C.P. et al. (2017). Climate change impacts in Latin America and the Caribbean and their implications for development. *Reg. Environ. Change*, 17.6, 1601-1621.

Riebe, C. S. et al. (2015). Climate and topography control the size and flux of sediment produced

on steep mountain slopes. *Proc. Natl. Acad. Sci.*, 112(51), 15574-15579.

Risser, M. D., & Wehner, M. F. (2017). Attributable human-induced changes in the likelihood and magnitude of the observed extreme precipitation during Hurricane Harvey. *Geophys. Res. Lett*., 44.

Rodell, M. et al. (2018). Emerging Trends in Global Freshwater. *Nature*, 557, 651–659.

Roderick, M. L., F. et al. (2014). A general framework for understanding the response of the water cycle to global warming over land and ocean, *Hydrol. Earth Syst. Sci.*, 18(5), 1575–1589.

Roudier, P. et al. (2014). Climate change impacts on runoff in West Africa: a review. *Hydrol. Earth Syst. Sci.*, 18, 2789-3801.

Running, S. et al. (2017). MOD16A2 MODIS/Terra Net Evapotranspiration 8-Day L4 Global 500 m SIN Grid V006. NASA EOSDIS Land Processes DAAC.

Salmoral, G. et al. (2015). Drivers influencing streamflow changes in the Upper Turia basin, Spain. *Sci. Total Environ.*, 503, 258-268.

Seddon, A.W.R. et al. (2016). Sensitivity of Global Terrestrial Ecosystems to Climate Variability, *Nature*, 531, 229–232.

Siler, N. et al. (2018). Insights into the zonal-mean response of the hydrologic cycle to global warming from a diffusive energy balance model. *J. Clim.*, 31(18), 7481-7493.

Sinha, J. et al. (2018). Assessment of the impacts of climatic variability and anthropogenic stress on hydrologic resilience to warming shifts in Peninsular India. *Sci. Rep.*, 8(1), 1-14.

Staal, A. et al. (2018). Forest-rainfall cascades buffer against drought across Amazon. *Nat. Clim. Change.*, 8, 539–543.

Sterling, S. M. et al. (2013). The impact of global land-cover change on the terrestrial water cycle. *Nat. Clim. Change*, 3(4), 385.

Srivastava, A. et al. (2020). The Role of Landscape Morphology on Soil Moisture Variability in Semi-arid Ecosystems. *Hydrol. Process.*

Stott, P. (2016).How climate change affects extreme weather events. *Science*, 352(6293), 1517-1518

Tabari, H. (2020). Climate change impact on flood and extreme precipitation increases with water availability. *Sci. Rep.*, 10(1), 1-10

Trenberth, K. E. (2011). Changes in precipitation with climate change. *Clim. Res.*, 47(1-2), 123-138.

Uuh-Sonda, J. M., Gutiérrez-Jurado, H. A., Figueroa-Espinoza, B., & Méndez-Barroso, L. A. (2018). On the ecohydrology of the Yucatan Peninsula: Evapotranspiration and carbon intake

dynamics across an eco-climatic gradient. *Hydrol. Proc.*, 32(18), 2806–2828. https://doi.org/10.1002/hyp.13230

van der Ent, R. J. et al. (2010). Origin and fate of atmospheric moisture over continents. *Wat. Resourc. Res.*, 46(9).

van Oldenborgh, G. J. et al. (2017). Attribution of extreme rainfall from Hurricane Harvey, August 2017. *Environ.Res. Lett.*, 12(12), 124009.

Wu, J., Miao, C., Zhang, X., Yang, T., & Duan, Q. (2017a). Detecting the quantitative hydrological response to changes in climate and human activities. Science of the Total Environment, 586, 328-337.

Wu, J. et al. (2017b). Contribution analysis of the long-term changes in seasonal runoff on the Loess Plateau, China, using eight Budyko-based methods. *J. Hydrol.*, 545, 263-275.

Wu, T. et al. (2019). Warming effects on leaf nutrients and plant growth in tropical forests. *Plant Ecol.*, 220(7-8), 663-674.

Yan, L., et al. (2016). Mechanisms of elevation-dependent warming over the Tibetan plateau in quadrupled CO 2 experiments. *Clim. Change*, 135(3-4), 509-519.

Yeh, P. J. F., & Wu, C. (2018). Recent acceleration of the terrestrial hydrologic cycle in the US Midwest. *J. Geophys. Res. Atmos.*, 123(6), 2993-3008.

Zhan, C. et al. (2012). Hydrologic response to climate variability and human activities in the Chao River catchment near Beijing. *Water Int.*, 37(5), 585-597.

Zhang, X. et al. (2013). Enhanced poleward moisture transport and amplified northern high-latitude wetting trend. *Nat. Clim. Change*, 3(1), 47-51.

Zhang, Y. et al. (2019). Coupled estimation of 500 m and 8-day resolution global evapotranspiration and gross primary production in 2002–2017. *Remote Sens. of Environ.*, 222, 165-182.

Zhang, G. et al. (2020). Response of Tibetan Plateau lakes to climate change: Trends, patterns, and mechanisms. *Earth-Science Reviews*, 208, 1-22. doi.org/10.1016/j.earscirev.2020.103269

Zhou, X. et al. (2013). An imperative need for global change research in tropical forests. *Tree Physiol.*, 33(9), 903-912.

Appendix

Equation A1: Formula and subformulas to compute potential evapotranspiration

$$\boldsymbol{\lambda E_{pot}} = \lambda E_{wetc} + \lambda E_{pottrans} + \lambda E_{wetsoil} + \lambda E_{soilpot} \quad \left(\frac{W}{m2}\right)$$

$$\boldsymbol{\lambda E_{wetc}} = \frac{\Delta \cdot R_n + \boldsymbol{p_a} \cdot \boldsymbol{C_a} \cdot F_c \left(\frac{e_s^* - e_a}{rhrc}\right) F_{wet}}{\Delta + \frac{p_a \cdot C_a \cdot rvc}{\lambda_v \cdot \varepsilon \cdot rhrc}}$$ **Wet canopy evaporation**

$$\boldsymbol{\lambda E_{pottrans}} = \frac{\alpha \cdot \Delta \cdot R_n (1 - F_{wet})}{\Delta + \gamma}$$ **Potential plant transpiration**

$$\boldsymbol{\lambda E_{wetsoil}} = \frac{\Delta \cdot R_n + p_a \cdot C_a \cdot (1 - F_c) \cdot \left(\frac{VPD}{r_{as}}\right) F_{wet}}{\Delta + \gamma \frac{r_{tot}}{r_{as}}}$$ **Wet soil evaporation**

$$\boldsymbol{\lambda E_{soilpot}} = \frac{\Delta \cdot A_{soil} + p_a \cdot C_a \cdot (1 - F_c) \cdot \left(\frac{VPD}{r_{as}}\right) (1 - F_{wet})}{\Delta + \gamma \frac{r_{tot}}{r_{as}}}$$ **Potential soil evaporation**

$\boldsymbol{F_c}$ = fraction of incoming radiation absorbed by plant (MOD15A2H.006 : Fraction of Photosynthetic Active Radiation)

$\boldsymbol{\Delta}$= slope between SVP and temp. $\Delta = \frac{\mathrm{de}^*}{\mathrm{d}T} = \frac{e_s{}^* - e_a}{T_s - Ta}$, As T increases so does kinetic energy of molecules. Hence pressure is higher.

$\boldsymbol{p_a}$= air density (1.22 $\frac{kg}{m^3}$ at sea level)

$\boldsymbol{c_a}$= air heat capacity ($1005\ J/K \cdot C^0$)

$\boldsymbol{R_n}$=Net incoming radiation W/m2

$$\boldsymbol{e_a} = actual\ vapor\ presure\ (e_a{}^* \cdot RH,\ kPa)$$

$$\boldsymbol{e_a^*} = (kPa\ ) saturation\ vapor\ pressure\ air\ Temperature\ Ta; (\boldsymbol{e_a^*}) = \mathbf{0.611} \times \mathbf{10}^{\left(\frac{\mathbf{17.3} \cdot \boldsymbol{Ta}}{\mathbf{237.3} + \boldsymbol{Ta}}\right)},$$

$$\boldsymbol{e_s^*} = (kPa\ ) saturation\ vapor\ pressure\ at\ \ surface\ \ Temperature,\ \boldsymbol{T_s}; (\boldsymbol{e_s^*}) = \mathbf{0.611} \times \mathbf{10}^{\left(\frac{\mathbf{17.3} \cdot \boldsymbol{Ts}}{\mathbf{237.3} + \boldsymbol{Ts}}\right)},$$

$$\boldsymbol{VPD} = Vapor\ Pressure\ Deficit\ (kPa)$$

$\boldsymbol{F_{wet}} = \begin{cases} 0 & RH < 70\% \\ RH^4 & 70\% \leq RH \leq 100\% \end{cases}$ =water cover fraction

rvc=latent heat transfer (rtot=$r_a + r_s$; aerodynamic resistance +surface resistance s/m)

$$\boldsymbol{rhrc} = \boldsymbol{r_{as}} = \frac{rhs * rrs}{rhs + rs}$$

$$\boldsymbol{rhs} = \boldsymbol{rtot} = \boldsymbol{rvc} = r_a + r_s$$

$\boldsymbol{r_a} = \frac{208}{Ws} = aerodynamic\ resistance\ in\ ,\ s/m\ \left(\boldsymbol{Ws} = winspeed\ \left(\frac{m}{s}\right)\right)$, force exerted by air on liquid

$$\boldsymbol{r_s} = 70\frac{s}{m}$$

$$= \left(\frac{RI}{LAI_{active}}\right)$$

RI=stomatal resistance (100s/m for well-watered grass)

$\boldsymbol{LAI_{active}}$=0.5*LAI

LAI=24*z_{veg} (z_{veg}= 0.12m for well-watered grass),leaf area/ground area

$\boldsymbol{rrs} = \frac{p_a \cdot c_a}{4\sigma(T_a+273.15)^3}$,resistance to radiative heat transfer

$\boldsymbol{\sigma} = \text{Stefan} - \text{Boltzman constant}\ (5.670373319 \times 10^{-8}\ W\ /\ m^2K^4)$, total intensity radiated by a blackbody

$\boldsymbol{A_C} = F_C R_n$= part of net radiation allocated to the canopy ($W\ /\ m^2$)

$\boldsymbol{A_{soil}} = (1 - F_c)R_n - G$=part of net radiation partitioned on the soil surface ($W\ /\ m^2$)

G= soil heat flux ($W\ /\ m^2$)

$\boldsymbol{\alpha} = \text{equilibrium ET (rate of ET)over a wide range of conditions.}$

$\boldsymbol{\gamma}$= relates pressure of water in air to Ta.

Conversion of units to mm/min $= \frac{W}{m2} = \frac{J}{m2*s} * \left(\frac{1\ kg}{2454000\ J}\right) * (60*30)\ \frac{mm}{min} = \frac{mm}{30min}$

Chapter 2: Global forest tipping points leading to changing hydrologic responses.

Abstract

Global forest cover is decreasing at an unprecedented rate, bringing alterations to the

water cycling of large freshwater-producing regions of the world. However, the critical thresholds before these alterations become irreversible are currently unknown across different forest types. Here, we document critical thresholds of deforestation in regions that underwent extensive forest cover loss induced by either drought, fire, or clear-cutting during the 2001-2016 period and report if these trends lead to increasing or decreasing water yield and warmer or cooler climate conditions. Our analysis shows substantial decreases in water yield at the early stages of tree cover loss in tropical rainforests, particularly in the Congo, Borneo, Sumatra, and Chilean Andean forests (<19%) compared to the Amazonia (~27%), with profound implications for their biodiversity and the global-scale ecosystem services that these forests provide. Boreal forests also show low thresholds of tree cover loss (~32%) leading to unstable hydrologic behavior although without a clear trend in water yield conditions. On the other hand, temperate forests display higher thresholds of tree cover loss (~46-53%) leading to changing hydrologic regimes but occurring rapidly once the threshold is surpassed. This study provides quantitative evidence of the tipping points of tree cover loss under which forests can maintain a stable hydrologic behavior. The thresholds and the speed of the alterations they induce should be useful to predict rapid hydrologic changes in forests expected to experience more frequent droughts, wildfires, and human-driven deforestation. Thus, results from this study could help inform (reassess) new (current) policies designed to contain further deforestation in areas close to surpassing their tipping points.

1. Background

Droughts, wildfires, and related deforestation events in the past two decades (2001-2021) have resulted in 437 million hectares of tree cover loss globally, an area measuring approximately one-half the size of Brazil (equivalent to an 11% global tree cover reduction since 2000) (Hansen et al., 2013; Watch, 2020) with local, regional and large-scale impacts on the water cycle and regional climate

(Goeking & Tarboton, 2020; Marengo et al., 2018; Sheil, 2018; Zhang et al., 2017). For example, tree cover loss, in general, decelerates the water cycle by weakening evapotranspiration processes, leading to changing precipitation and temperature patterns in large forested regions (Ellison et al., 2012). Increases in climate variability patterns, in turn, have an impact on the amount of precipitation reaching the landscape affecting the quantity of surface streamflow (water yield) that varies in magnitude across continents (Ellison et al., 2012). However, the extent to which forests may continue to maintain stable water yields despite losing significant portions of tree cover and their impact on regional climate is currently unknown.

Although there is evidence of changing water yield under forest disturbance, the direction of these changes remains unclear (Ellison et al., 2012; Goeking & Tarboton, 2020). For example, a comprehensive review of multiple studies evaluating the effects of tree cover loss on water yield reports no clear consensus and consistent direction of hydrologic changes; in some cases, water yield is increasing, in others decreasing and in some no significant changes have been detected (Goeking & Tarboton, 2020). The same work concludes that most of these studies were evaluated categorically and not quantitatively and points to the fact that the majority of those studies focused on Temperate Coniferous Forests, highlighting the need for a quantitative approach across and a synthesis effort on different forests types that could reveal the directions that major water resources are headed at a global scale.

Human-driven deforestation and wildfires are major causes of tree cover loss. Many of these events occur in highly threatened-biodiverse tropical rainforests (Crowther et al., 2015) and boreal ecosystems (Hansen et al., 2013). However, their impacts on hydrologic processes have not been systematically studied and the directions in which hydrologic changes may be occurring are still unclear. For example, although the Amazon basin has been extensively studied (Chambers & Artaxo, 2017; Lawrence & Vandecar, 2015; Leite-Filho et al., 2021; Malhi et al., 2008; Spracklen Xu et al.,

2022 & Garcia-Carreras, 2015), other important tropical basins that have a major influence on global climates, such as the Central African and Southeast Asian forests have received less attention (Lawrence & Vandecar, 2015). Furthermore, the frequency of fire and forest exploitation leading to forest clearing in boreal systems is proportionally second to that in tropical ecosystems (Hansen et al., 2013), but only a few studies evaluate these impacts on boreal hydrology (Pimentel & Arheimer, 2021). Compounded with the loss of tree cover, changes in land surface properties reinforce current climatic trends such as rising temperatures leading to increasing snowmelt in high-latitude regions. Studies evaluating the role of forest clearing on these dynamics are missing, or at best fragmented (te Wierik et al., 2021; Valeo et al., 2003). Given the lack of clarity on the effects of forest disturbance on hydrologic responses and the thresholds driving changes in water yield and regional climate, reporting the tipping points leading to significant changes in the hydrologic sensitivity in the world's major forests is critical to aid in forest management strategies to prevent irreversible or permanent changes in freshwater resources.

A region's fragility to experiment with changes in its hydrologic behavior to climatic perturbations can be assessed by means of a hydrologic sensitivity analysis (Domínguez-Tuda & Gutiérrez-Jurado, 2021). The Hydrologic Sensitivity Index (HSi), is a metric conceived to detect changes in hydrologic responses to climate variability and it is based on the changes of actual evapotranspiration (AET) against changes in the potential evapotranspiration (PET) normalized by precipitation (P), where HSi>1 show disproportionate hydrologic responses to changing climatic conditions(Domínguez-Tuda & Gutiérrez-Jurado, 2021). HSi is used in this study to evaluate departures in historic hydrologic behavior in the face of land cover disturbances such as tree cover loss using 3-year HSi averages of before and after-disturbance periods (see Methods). To do this, we compute Hydrologic Sensitive area (HSia) as the percentage of deforested area with high HSi (>1) and plot against percent tree cover loss (TCL,%) in 45 selected regions across 5 different forest types

(Tropical Rainforests, Boreal forests and Temperate Coniferous, Mediterranean, and Mixed forests) which have undergone extensive tree cover loss due to either drought, wildfire, or deforestation during the period 2001-2016 (Figure 1) (see Appendix Table A1-A5 for details of each deforestation event)**.** We report global forest tipping points (c = critical thresholds) of tree cover loss leading to rapid shifts in hydrologic behavior, the speed (β = sensitivity rate) at which this occurs once the threshold is surpassed and the initial mean HSi of the forest under undisturbed conditions (δ = inherent mean hydrologic sensitivity). Also, through the same methodological approach, we find and report the effect of tree cover loss on increasing vs decreasing water yield and warming vs cooling trends for each forest type.

2. Methods

2.1 Concept of Hydrologic Sensitivity

Changes in the water cycling of ecosystems that have undergone disturbances altering the physical properties of the landscape can be assessed using hydrologic metrics (Creed et al., 2014; Helman et al., 2017; Sinha et al., 2019) that are able to identify deviations from normal average climate conditions. For instance, the Hydrologic Sensitivity Index (HSi), a metric that has been used to evaluate changes in hydrologic response to climate variability can also be used to evaluate departures in historic hydrologic behavior in the face of land cover disturbances such as tree cover loss (Domínguez-Tuda & Gutiérrez-Jurado, 2021).

Hydrologic sensitivity to climate variability can be understood by how responsive water cycling behaves to large or small perturbations in climatic conditions in any given region. That is if a region disproportionally changes its hydrologic functioning (becomes hydrologically unstable) when exposed to a climate disturbance or extreme weather, it is considered hydrologically sensitive (Domínguez-Tuda & Gutiérrez-Jurado, 2021). In this work, to understand the effects of forest conditions on hydrologic responses, the HSi metric (Equation 1) is used to evaluate the relationship

between hydrologic sensitive areas and tree cover loss resulting from human and/or climate-induced disturbances.

The HSi is based on the widely used Budyko framework (Creed et al., 2014; Helman et al., 2017; Roderick et al., 2014; Sinha et al., 2019), which plots hydrologic responses relative to climate providing a reference on the behavior of the long-term mean water balance as a function of the average climatic conditions (i.e., Budyko's Curve: dashed line) of an area (Budyko, 1974; Greve et al., 2016; Helman et al., 2017; Roderick et al., 2014; Trenberth, 2011) (Figure 1). The Budyko framework evaluates the relationship between annual values of Actual Evapotranspiration and Potential Evapotranspiration (AET and PET respectively) normalized by Precipitation (P, total water available for ET in a closed water balance scenario). In simple terms, the Budyko framework captures the hydrologic behavior, known as the Evaporative Index (EI; AET/P) of any location under a given climatic condition, and the Dryness Index (DI; PET/P).

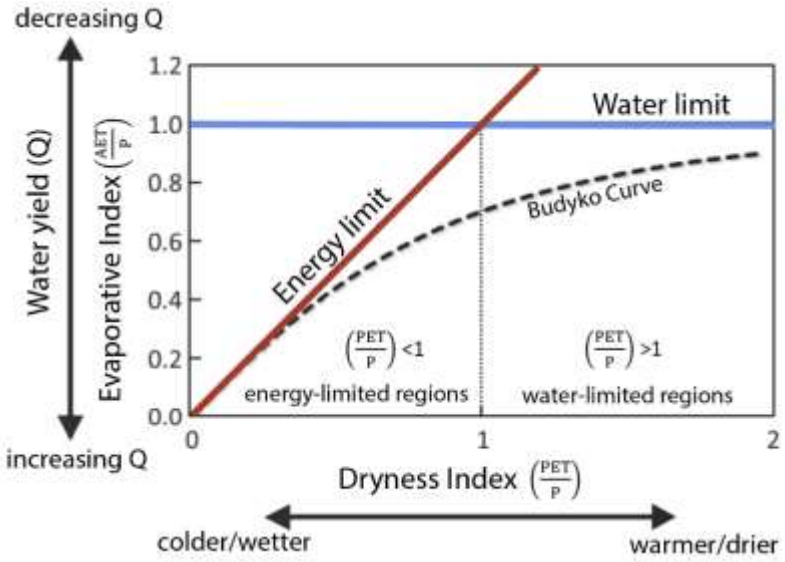

Figure 1. Budyko's Framework. The framework plots the evaporative index against the dryness index. When the evaporative index increases (decreases) the water yield decreases (increases). The solid lines represent the energy (red) and water limit (blue) lines, and the dashed line represents the historical average of where regions would plot given information on their climate (known as the original Budyko curve) (Budyko, 1974; Domínguez-Tuda & Gutiérrez-Jurado, 2021).

Therefore, a region's EI can be obtained along the curve given information on its DI (climate). HSi is quantified by how far the EI deviates from Budyko's curve (the normal) relative to the change

in DI. Thus, HSi is defined as the ratio between the interannual change in the evaporative index relative to the curve (ΔEI_R) and the interannual change in the range of the dryness index (ΔDI) (Domínguez-Tuda & Gutiérrez-Jurado, 2021). It is important to point out that HSi evaluates the absolute difference between DI and EI_R, as the first step to evaluating the overall hydrologic response to variations in the climate. Afterward, the respective signs of the dryness index ($\pm \Delta DI$) and evaporative index ($\pm\Delta EI_R$) are used to explore the impact of tree cover loss on climate and water yield direction, respectively.

For the purpose of this study, we utilize HSi as the ratio between the change in the 3-year averages of pre-disturbance (gray dot) and post-disturbance (black dot) periods for each forest clearing event to evaluate hydrologic responses to tree cover loss (Figure 2). We conceive forested areas as being hydrologically sensitive if the pixel values within a disturbed region (tree cover loss>0%) display HSi>1. That is, high sensitivity occurs when a small change in DI leads to a large change in EI_R (HSi >1 = $\Delta EI_R > \Delta DI$, sensitive) and low sensitivity (i.e. resilient) occurs when a large change in DI results in a small change of EI_R (HSi<1=|$\Delta DI<\Delta EI_R$|, resilient) before and after the event.

The HSi metric uses the adapted Budyko formulation (Greve et al., 2016), B_A, which accounts for changes in storage water terms (y0=AET-P/PET only when AET-P>0) making this metric useful to compute hydrologic responses at any spatiotemporal scale (Domínguez-Tuda & Gutiérrez-Jurado, 2021). Thus, by tracking the changes in hydrologic response (ΔEI_R) of a location or region relative to Budyko's curve (B_A), that is, its water yield deviation to climatic variability before and after tree cover loss (ΔDI), we can calculate the hydrologic sensitivity in disturbed regions in the following manner:

$$\mathbf{HSi} = \frac{\mathbf{\Delta EI_R}}{\mathbf{\Delta DI}} = \left|\frac{EI_{R_{disturbed(3-yr)}} - EI_{R_{undisturbed(3-yr)}}}{(DI_{disturbed(3-yr)} - DI_{undisturbed(3-yr).})}\right|, \quad (1)$$

$$\text{where } EI_R = EI - B_A$$

where sensitive regions will display HSi>1, and resilient locations will show HSi ≤1. All computations leading to HSi are carried out in the Google Earth Engine platform (Gorelick et al.,

2017)

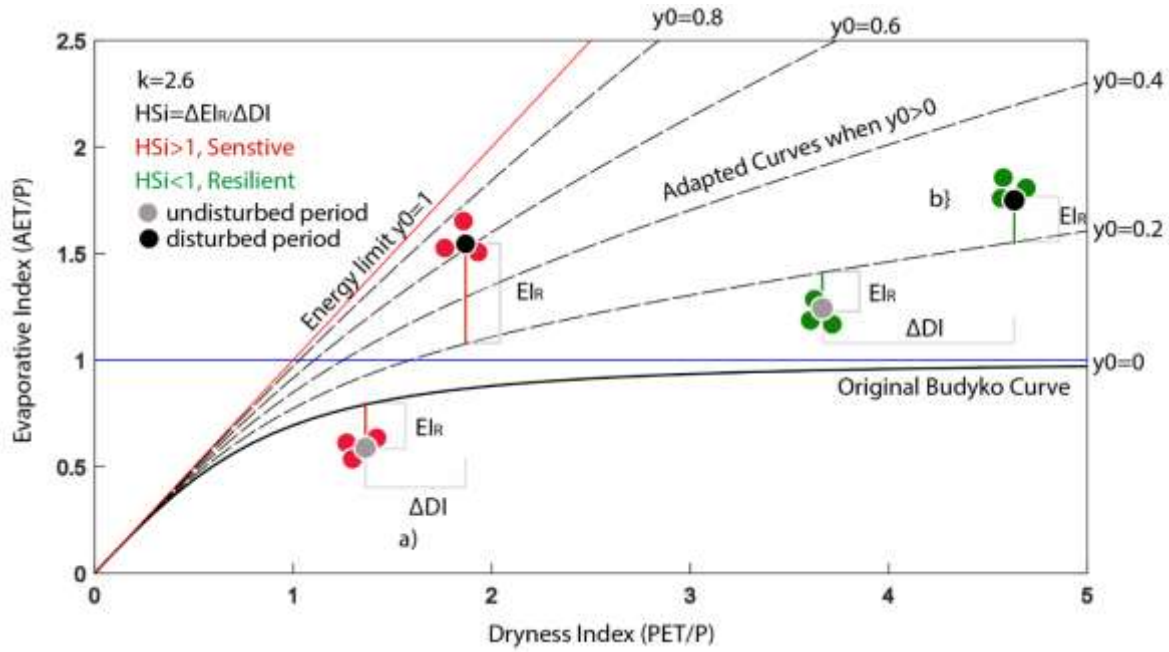

Figure 2. Adapted Budyko Curve. The Budyko framework accounts for changes in storage for regions where y0= AET-P>0, so that the range in EI_R is in reference to the adjusted curve, while the range in DI is not affected. HSi is calculated as the ratio of a catchment's range in 3-year average in EI to its range in DI prior (gray dot) and post (black dot) the deforestation event: HSi= $(\Delta DI)/(\Delta EI_R)$, where a) high sensitivity (HSi > 1, red) (i.e., approximating theoretical behavior), and (b) low hydrologic sensitivity (HSi<0, green) (i.e., deviating from theoretical behavior).

2.2 List of disturbed forested regions

Increasing wildfire activity, drought, and other deforestation events have been reported in many regions of the world (Allen et al., 2010; Watch, 2020). This study evaluates 45 regions encompassing five different climate types (9 Boreal forests, 14 Temperate Coniferous Forests, 5 Mixed Forests, 5 Mediterranean Forests, and 12 Tropical Rainforests) from the period 2001-2016. The selected regions underwent in aggregate a total of 28 wildfires, 9 deforestation, and 8 droughts. Figure 3 shows the location of each one of the events and their characteristics are described in detail in the Appendix (Tables A1-A5).

Figure 3. Map ID events. The location of 45 events that underwent either drought, wildfire, and/or a deforestation event leading to severe tree cover loss during 2001-2016 period. Each number corresponds to one event (detailed descriptions for each event are listed in Appendix Table A1-A5). Map created in ArcGIS 10.7.1 software.

2.3 Variables for computing HSia

We use annual values of AET, PET, and P, along with the percent tree cover for the period of January 2001 to December 2016 due to the availability of datasets. The satellite products used for this analysis are described in Table 1. AET is derived from Penman-Monteith Leuning version 2 (PML-V2) at 500m resolution and is noticeably better than major state-of-the-art AET products including PML-V1, MOD16, and GLEAM (Zhang et al., 2019). PET is derived from the Moderate-Resolution Imaging Spectroradiometer (MOD16A2) Version 6 onboard the Terra satellite at 500m resolution (Running et al., 2017). P is derived from the Multi-Source Weighted-Ensemble Precipitation dataset (MSWEPv2) at 0.1-degree resolution combining gauge and satellite products, and multiple corrections for regional differences making it of the most high-quality P products available with spatial resolution

≤0.1° (Beck et al., 2019; Domínguez-Tuda & Gutiérrez-Jurado, 2021).

Percent tree cover defined as a vertically projected area of vegetation (including leaves, stems, branches, etc.) of woody plants above a given height is obtained from Global Forest Cover Change (GFCC) (Feng et al., 2016) with 30m resolution and available for four epochs every 5 years: 2000, 2005, 2010 and 2015. This tree cover dataset is the highest-resolution multi-temporal depiction of Earth's tree cover available demonstrating global accuracy (Feng et al., 2016) in depicting the extent of wildfire events with more precision than the Burned Area dataset obtained from MODIS (MCD64A1.006) (Giglio et al., 2018) at 500m resolution is used along with the GFCC dataset. Overall, these products used in this study have been tested worldwide for their accuracy with ground-based sampling and span a variety of climates and land cover types providing confidence in applying these datasets for studies of global terrestrial water and energy cycles and environmental changes (Table 1).

Table 1: Data Collection. Variables and datasets used to compute HSi and tree cover loss with their temporal and spatial resolution

Variable	Product	Temporal resolution	Spatial resolution	Reference
AET (April 4, 2002-present)	**PML-V2** (Penman-Monteith-Leuning Version 2)	8-day	**500m**	Zhang et al.(2019)
PET (2001-present) AET(2001)	**MODIS** (MOD16A2.006 Modeling Imaging Spectroradiometer)	8-day	**500m**	https://doi.org/10.5067/MODIS/MOD16A2.006
P (1979-Oct. 2017)	**MSWEP-v2** (Multi-Source Weighted Ensemble Precipitation Dataset Version 2)	Daily	**0.1**◦ (11,100m)	Beck et al. (2019)
Tree Cover (%)	**GFCC** (Global Forest Cover Change)	5-yr (2000,2005,2010,2015)	**30m**	Sexton et al.(2013)
Burned Area (Burn day of year)	**MODIS** (MCD64A1.006)	Monthly (2000-present)	**500m**	Giglio et al. (2018)

2.4 Hydrologic Sensitive Area against tree cover loss

The affected area was located on a global map using the annual values of percent tree cover and Burned Area from MODIS for wildfire events. The percent tree cover loss (TCL) was obtained by computing the difference in percent tree cover between the year prior and the year post disturbance according to the availability of the dataset. For example, TCL for a wildfire event occurring in 2004 was obtained by computing the difference between the percent tree cover in 2000 and 2005 (%tree $cover_{2005}$ - %tree $cover_{2000}$=$\%TCL_{2005\text{-}2000}$). Once the area where TCL>0% is located for each event, we compute HSia on those grid cells. These locations are verified with the coordinates reported for each event (See references in Appendix Table A1-A5). HSi values were computed by taking the difference EI_R and DI between the 3-year average prior and post-disturbance (Equation 1). The Hydrologic Sensitive Area (HSia) was obtained by computing the ratio of grid cells with values of HSi>1 relative to the total number of grid cells in the encircled disturbed area (grid cells with TCL>0%). The HSia was computed for every 10% TCL and plotted. When plotting HSia [0,100] against TCL [0,100] for each event, the trend of data points for the majority of the events shows a sigmoidal trajectory. For instance, Figure 4 illustrates the data points (red dots) for Event No. 1 (Appendix A1), where the growth in HSia remains low until a critical tree cover loss is reached and a sudden exponential increase in the relationship leads to 100% of the area being hydrologically sensitive (HSi area=100%, see Appendix A6-A9). To define this trend mathematically, this behavior is modeled using Richard's Curve Growth function (black line in Figure 4) with 5 parameters and is computed as follows:

$$f(x;\alpha,\beta,\gamma,\boldsymbol{\delta}) = \boldsymbol{\delta} + \frac{\boldsymbol{\alpha-\delta}}{1+\exp(-\beta*(x-\gamma))}, \qquad (2)$$

where, α represents maximum sensitive area (α=100%, upper asymptote), β= growth rate of sensitivity area, γ = percent tree cover loss (x) when y= α-δ/2 , and δ= initial sensitive area (given

value, lower asymptote) (Birch, 1999).

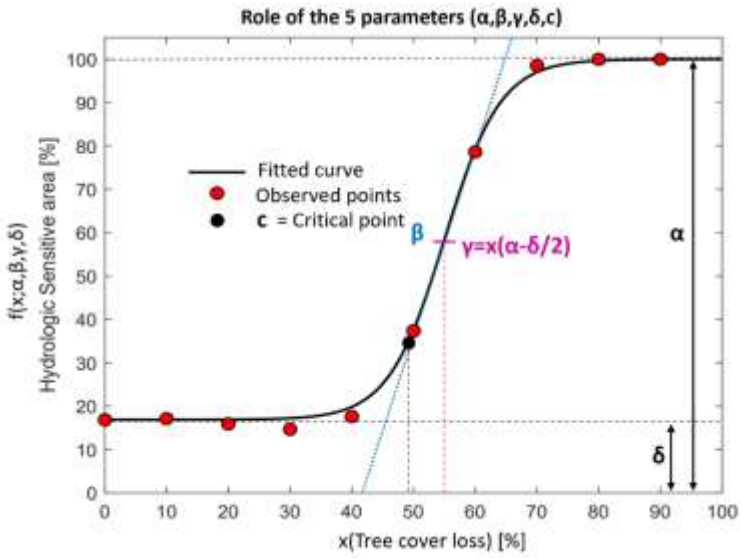

3

Figure 4. Richard's Growth function of 5 parameters. Diagram displays Richard's curve (black line) for Event ID 1 during a severe drought in northwestern Russia (2004-2006) approximating the observed data points (red dots). The 5 parameters used to fit the observations were: $\delta = 16.87\%$ (initial value), $\beta = 0.22$ (growth rate of sensitive area, c=49% (critical point of acceleration), and $\gamma = 55\%$ (x value when $\alpha - \delta/2$).

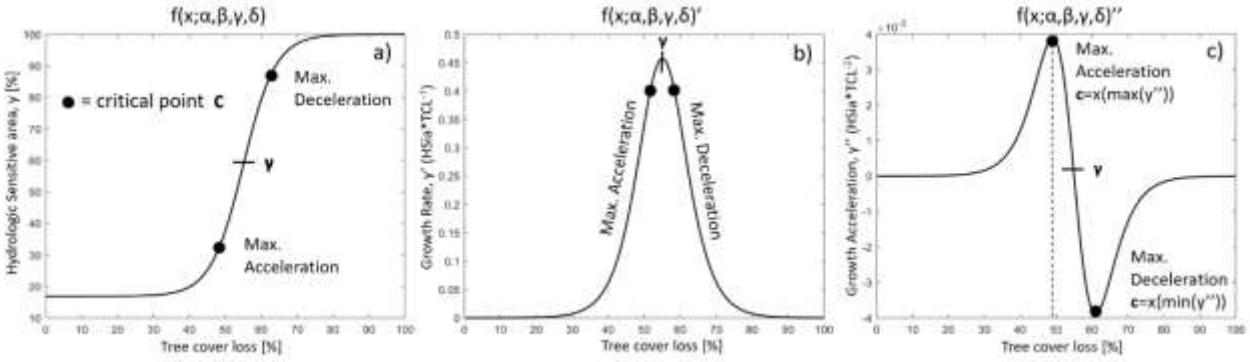

Figure 5. (a-c) Critical threshold step-by-step computation. Illustration showing how critical points were obtained by numerically computing Richard's function derivatives using Event #1 as an example. 5a) Original Richard's Curve function, 5b) first derivative of Richard's function; 5c) second derivative of Richard's function: The critical points used in this study are those in which maximum growth acceleration is attained [y" value on c)].

The critical threshold, *c*, is obtained by plotting the second derivative of the Richards curve function. In Figure 5c, the critical points are defined as the x value that corresponds to the maximum or minimum y'' value (maximum HSia acceleration and minimum HSia deceleration). For this study, the *c* of interest is the maximum HSia acceleration (black dot) that is the x value corresponding to maximum y'' value (Figure 5c). In this case, Event No. 1, TCL above 49%, constitutes a critical point

resulting in rapidly growing hydrologic responses.

Richards curve function is computed for each event to obtain c, where β and γ parameters are inferred by observing which values best adjust the curve to the data points while α and δ are given values (α=100% and δ =initial value) (Figure 5). Events 7, 12, 18, 29, and 31 are discarded for this part of this analysis since irregular patterns in their diagrams could not be reasonably adjusted by Richard's growth function. For these events, however, the water yield and climate direction were attainable and included in the analysis. The resulting functions for each event are grouped into forest type (see Appendix: Figure A1-A5) and are plotted along with the average trend (Figure 7). Violin plots are used to plot the variability in c and β parameters (Figure 8).

2.5 Computing climate and water yield direction

Additionally, Figure 6 plots ΔEI_R against ΔDI conceptually showing how climate and water yield direction can be obtained from HSi. For instance, all colored areas represent hydrologic sensitivity ($HSi>1=|\Delta EI_R|>|\Delta DI|$). For obtaining the climate and water yield direction, the signs of the numerator and denominator in the HSi metric (non-absolute values, ±) are considered since changes in the evaporative index ($\pm\Delta EI_R$) and dryness index ($\pm\Delta DI$) give us information of less water yield vs greater water yield and warmer vs cooler conditions, respectively. For instance, figure 6a displays the climate direction scenario where the warmer climate ($+\Delta DI$) is indicated by yellow, and the cooler state ($-\Delta DI$) is represented by red color. Similarly, figure 6b displays the water yield direction, where decreasing water yield ($+\Delta EI_R$ or -Q) is in yellow color and increasing water yield ($-\Delta EI_R$ or +Q) is in blue color. The diagram is split into 4 quadrants indicating the possible climate and water yield directions: Each quadrant is read as follows:

Quadrant I = less water yield and warmer climate;

Quadrant II = less water yield and cooler climate;

Quadrant III = greater water yield and cooler climate;

Quadrant IV = less water yield and warmer climate.

The sum of the sensitive grid cells (colored region) in Quadrant I and II indicate the total HSia that is decreasing in water yield ($+\Delta EI_R$). Similarly, the sum of sensitive grid cells in Quadrant III and IV indicate the total HSia that is increasing water yield ($-\Delta EI_R$). The sum of sensitive grid cells in Quadrant I and IV indicate the total HSia that is increasing in warmer conditions ($+\Delta DI$). The sum of sensitive grid cells in Quadrant II and III indicate the total HSia that is decreasing in water yield ($-\Delta DI$). For each event, the HSia is plotted against tree cover loss along a colored grid indicating the directions in climate and water yield (Results: Figure 9 and 10).

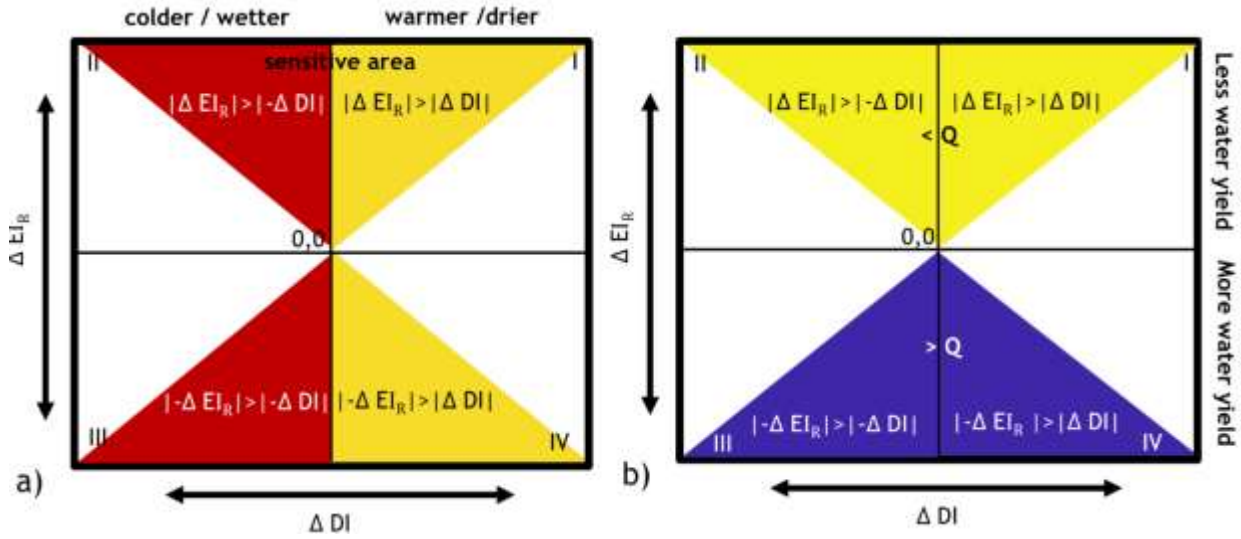

Figure 6. Mean Hydrologic Sensitive Area Concept. The diagrams show how the hydrologically sensitive area is computed and how it is partitioned in its climate and water yield direction. All deforested areas have pixel values, where each pixel represents a point that can be either hydrologically sensitive or resilient. All colored areas represent the case when a point or pixel value would fall in a sensitive area (HSi>1) since $|\Delta EI_R| > |\Delta DI|$ over line 1:1 (slope=1), while white or uncolored regions in the diagram represent points that would fall resilient areas (HSi≤ 1) since $|\Delta EI_R| < |\Delta DI|$ on or below the 1:1 line. However, the quadrant they fall in represents the climate and water yield direction. For instance, the diagram on the left a) Climate direction concept: Quadrant I and IV represent the case where hydrologic sensitive areas are becoming drier/warmer (yellow) so that the change in $+\Delta DI$ is positive, while in quadrants II and III represents the areas which have become cooler/wetter the change in $-\Delta DI$ is negative (red). The diagram on the right) Water yield direction concept: Quadrants I and II represent the condition where hydrologic sensitive areas show decreasing water yield tends so that the change in $+\Delta EI_R$ is positive (yellow), while quadrants III and IV represent the areas that show increasing water yield trends so that the change in $-\Delta EI_R$ is negative (blue).

3. Results

To identify global forest tipping points of tree cover loss leading to high hydrologic sensitivity and speed at which this occurs, we analyzed 45 areas affected by drought, wildfire, and deforestation leading to extensive tree cover loss. In Figure 7, we synthesized the results by grouping the average trend in hydrologic behavior as a function of tree cover loss for each forest type. Tropical rainforests display the lowest critical thresholds, and average sensitivity rate values (c =~19-27%, β= 0.17, respectively). This is followed by Boreal forests that display the second-lowest critical values and lowest sensitivity rate (c =32%, β= 0.14, respectively). Mixed Forest displays high critical values, and high sensitivity rates (c =46%, β= 0.21). Temperate Coniferous Forests and Mediterranean Woodlands display the highest critical threshold, and highest sensitivity rate (c =52-53%, β= 0.23-0.29). The initial value of HSia (δ) on the y-axis, represents the inherent hydrologic sensitivity value for each forest, where Tropical rainforest (δ=49%) and Boreal forest (δ =25%) have the highest value followed by the Temperate forest group (Temperate Coniferous, Mixed, and Mediterranean forests). The shaded area shows +/- one standard deviation for all ecosystems indicating that the majority of events in each ecosystem are slightly more or less sensitive than the average value.

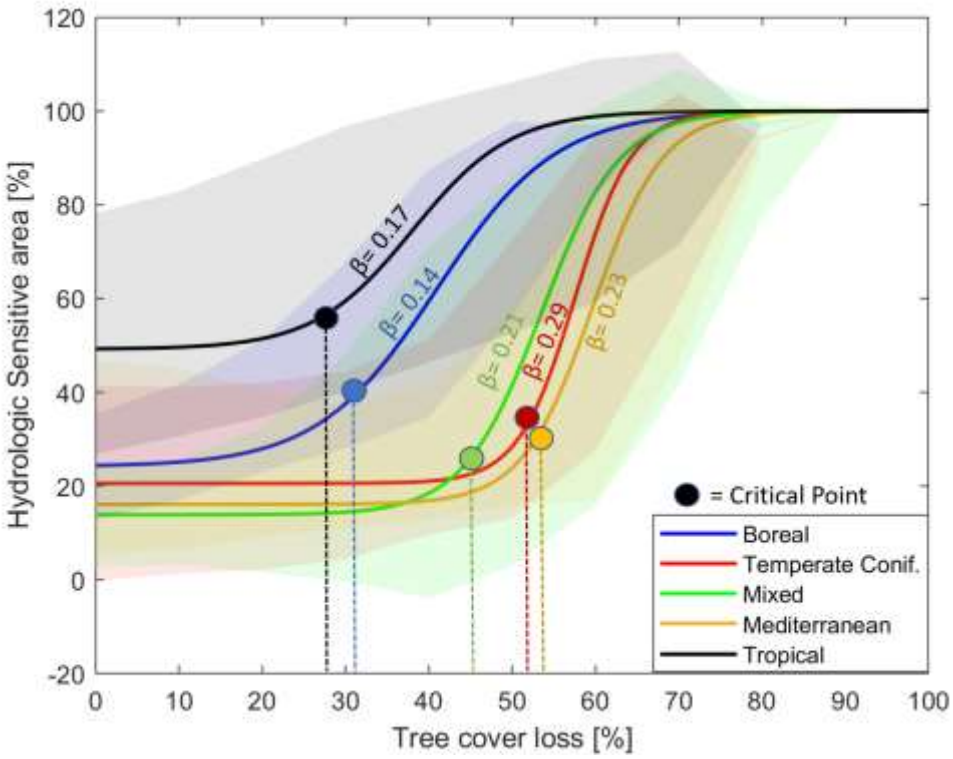

Figure 7. Hydrologic Sensitive Areas against tree cover loss. Defined as the average values of Richard's curve parameters per biome (with standard deviation shade) and plotted against percent tree cover loss. Labels represent the sensitivity rates (β) and critical points, (c) where: Tropical Rainforests (c=27%, black), Boreal forests (c=32%, blue), Temperate Broadleaf and Mixed Forests (c=46%, green), Temperate Coniferous Forest (c=52%, red), Mediterranean Woodlands and Scrub (c=53%, yellow). Diagram created in MATLAB R2019a.

The relationship between critical points and sensitivity rates (Figure 8a) varies for each forest type. In general, the critical threshold is positively proportional to the increase in sensitivity rate; particularly, Mediterranean (R^2=0.97) and Mixed (R^2=0.88), forests display a strong correlation, Tropical forests (R^2=0.50) show a moderate correlation, and Boreal (R^2=0.25) and Temperate Coniferous forests (R^2=0.22) show a weak correlation. Tropical and Mixed forests show the largest variability in critical thresholds (Figure 8b). Tropical forests have a higher probability at low values. Figure 8c shows that Tropical and Temperate Coniferous forests have high variability in sensitivity rates. Critical points and sensitivity rates are high in Temperate Coniferous, Mixed and Mediterranean forests, while the lowest is displayed in Tropical and Boreal forests. Overall, tropical and boreal forests are most hydrologically sensitive to tree cover loss since they display the lowest

critical thresholds. Particularly, the forests of Borneo, Sumatra, Congo, and Chile (subtropical) have lower-than-average critical thresholds compared to the rest of the affected tropical events (see Appendix Table A6). Also, the sensitivity rates increase (decrease) with increasing (decreasing) critical thresholds and when initial values of HSia are low (high).

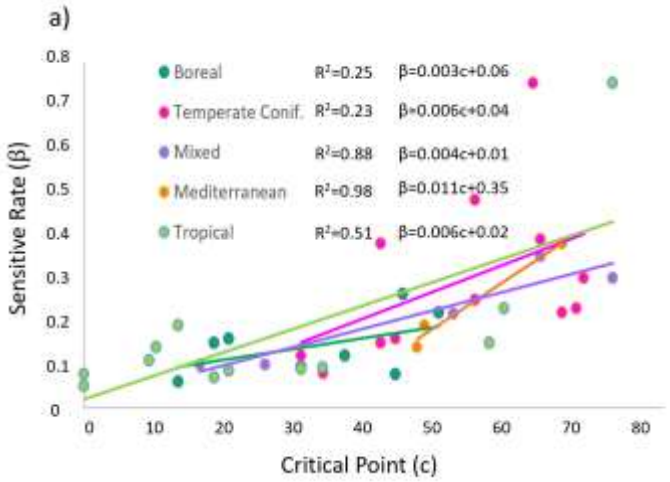

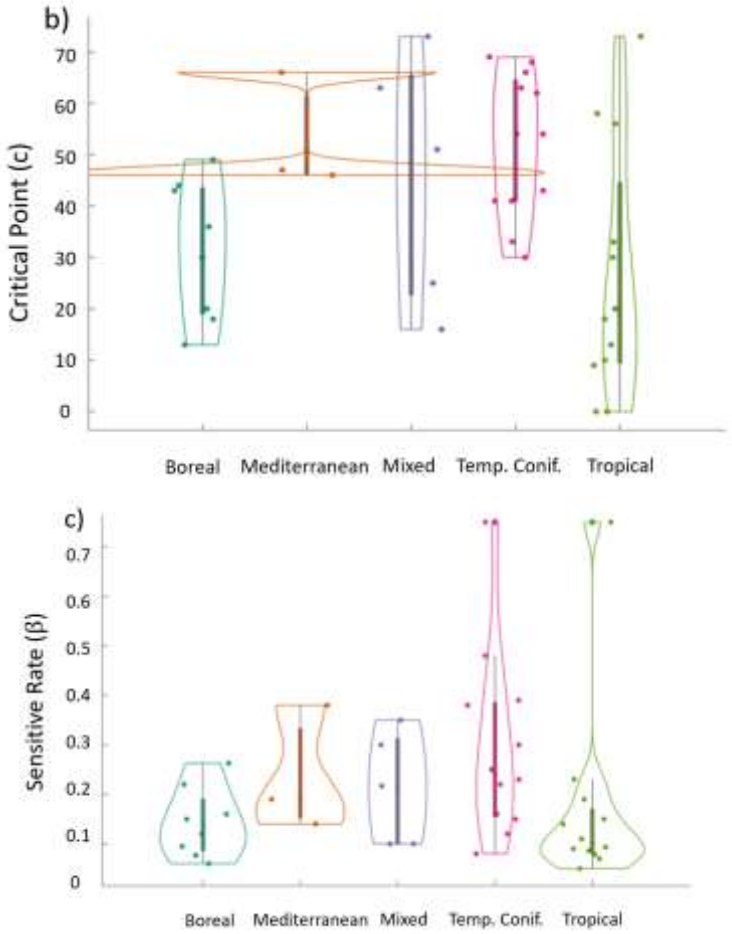

Figure 8a-c. Critical threshold values and sensitivity rates. Violin plots where a) Correlation of sensitivity rates (β) and critical points (c) across different forest types. The distribution of c and β per biome is shown with violin plots in (b) and (c) respectively. The violin plots show the median values (dashed line in thick colored line), the interquartile range (thick colored line), and the thin gray line represents the rest of the distribution, except for outliers. The area of the violin that is wide indicates high probability. The longer (shorter) the violin the higher (lower) the variability in values.

Second, for all 45 events, we document whether tree cover loss led to increasing or decreasing water yield (Figure 9) and if this resulted in a cooler or warmer climate state in the affected areas (Figure 10). The results show 42% of events resulted in a warmer climate with decreasing water yield due to forest cover loss. Of this total, 47% occurred in Tropical rainforests; 36% occurred in Temperate Coniferous, Mixed, and Mediterranean forests, and 21% occurred in Boreal forests. On the other hand, 33% of the total events resulted in a cooler climate and greater water yield. Of this total, 73% occurred in Temperate forests and 26.7% occurred in either Boreal or Tropical forests.

Finally, 11% of events resulted in neutral conditions. Opposite trends were seen in 13.4 % of events where 6.7% of events resulted in warmer climates accompanied by increasing water yield and the other 6.7% of events resulted in cooler climates with decreasing water yields.

In general, Tropical Rainforests display a clear tendency toward decreasing water yield and warmer climate states at the early stages of tree cover loss. Boreal forests display a clear tendency towards warming conditions but no clear tendency in direction of water yield. Results show both increasing and decreasing water yield trends. Temperate Coniferous forests display a tendency toward a cooler climate and increasing water yield. However, there are also minor regions with a tendency toward the opposite direction: warmer states and decreasing water yield. Mixed forests display a tendency toward a warmer climate direction and decreasing water yield. Mediterranean forests display a tendency towards increasing water yield and an increase in cooler climate conditions.

In Tropical Rainforest, only events 37 and 38 display a cooler climate and increasing water yield due to disturbance, while events 34, 35, 36, 39, 40, 41, 42, 43, and 44 display a warmer climate accompanied by decreasing water yield. Event 45 is neutral for both parameters. In Boreal forests, events 1, 3, 4, and 8, display a warmer climate with less water yield; Events 5 and 6 display warmer conditions but with an increase in water yield; Event 2 displays a cooler climate with a decrease in water yield, and events 7 and 9 display cooler conditions with increasing water yield. In Temperate Coniferous forests, Events 10, 13, 15, 17, 19, 20, and 22, display cooler conditions with increasing water yield (dominant trend); Events 18, 21, and 23 display warmer conditions with decreasing water yield; events 11 and 17 display neutral climate conditions with increasing water yields; Event 12 displays cooler conditions with decreasing water yield; Event 14 displays a neutral trend in both climate and water yield direction.

In Mixed forests, events 24 and 26 display a warmer climate with less water yield; Event 25

displays a cooler climate with increasing water yield; event 28 displays a cooler climate with decreasing water yield, and Event 26 displays a warmer climate with a neutral water yield direction. In Mediterranean forests, events 30, 31, and 32 display a cooler climate with increasing water yield; event 29 displays a warmer climate with increasing water yield; Event 33 displays a warmer climate with decreasing water yield.

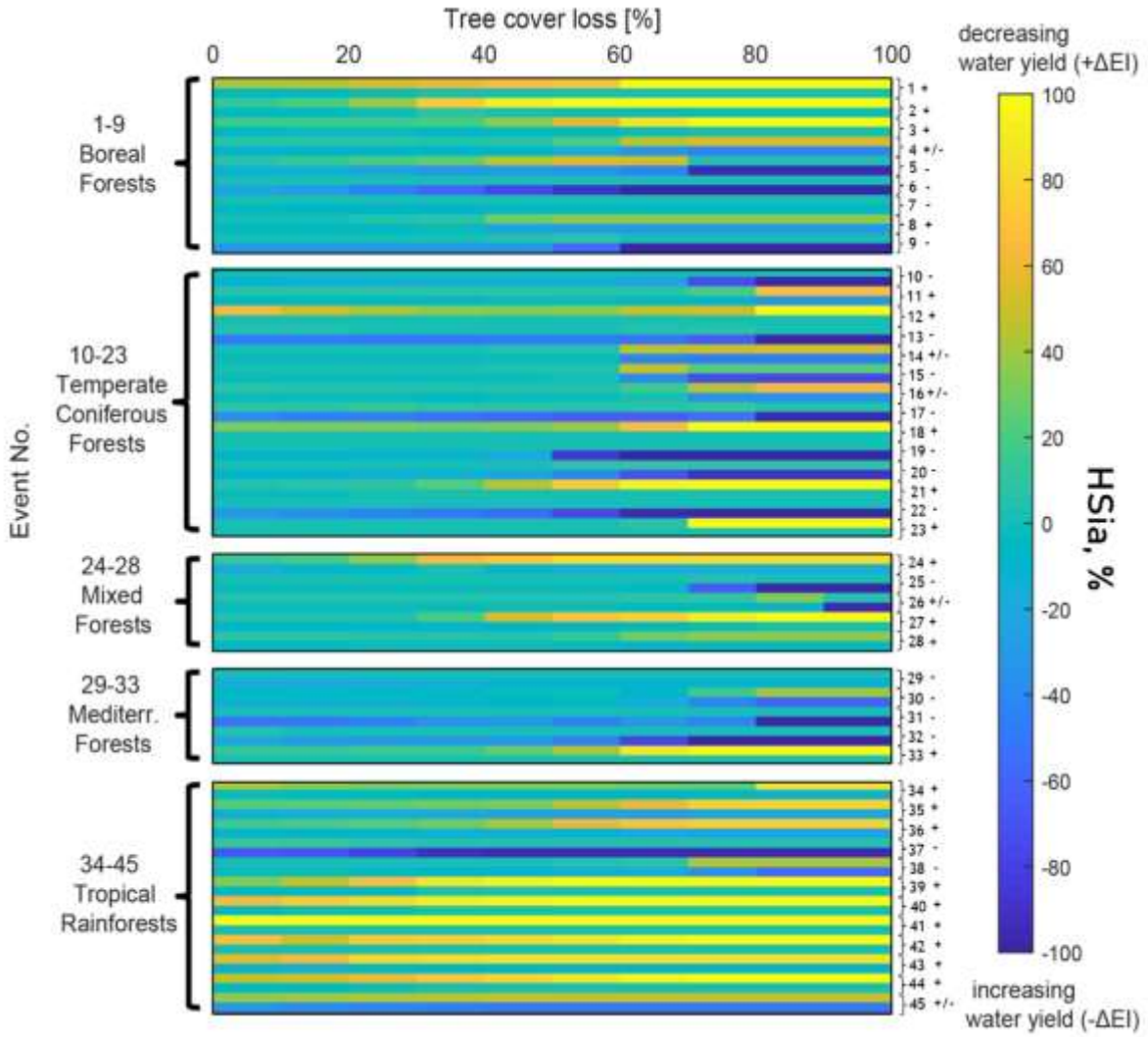

Figure 9. Water yield direction. Hydrologic sensitive areas are partitioned into decreasing water yield (based on the portion of disturbed area with +ΔEI) or increasing water yield (based on a portion of disturbed area with -ΔEI) as a function of tree cover loss (for intervals of 10%). The absolute sum of each pair of rows equals the total HSia. Events 1-45 are grouped by forest type and next to each event is the event number and the dominant direction for each event: +, for less water yield, - for increased water yield, and +/- for neutral direction. The first row for each pair equals the portion of total HSia towards decreasing water yield [0,100] (blue-green to yellow), while the second row of each pair equals the portion of the HSia towards increasing water yield [0,-100] (blue-green to dark blue). Data is computed in Google Earth Engine and the diagram is created in MATLAB R2019a software

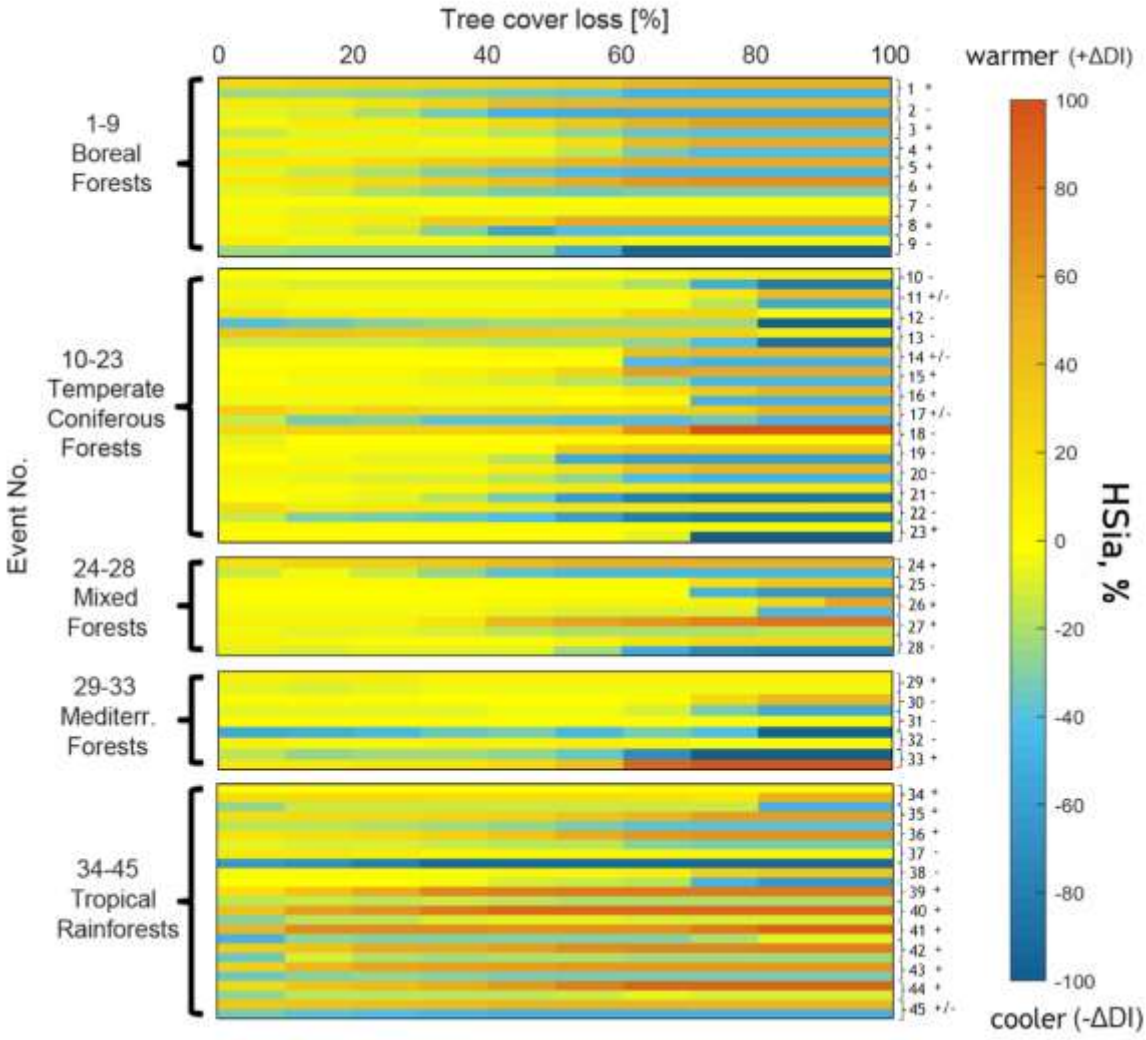

Figure 10. Climate direction. Hydrologic sensitive areas are partitioned into drier climate conditions (based on the portion of disturbed area with +ΔDI) or wetter/colder states (based on the portion of disturbed area with -ΔDI) as a function of tree cover loss (for intervals of 10%). The absolute sum of each pair of rows equals the total HSia. Events 1-45 and area grouped by forest type and next to each event is the event number and the dominant direction for each event: +, for drier/warmer climate, - for colder/wetter climate, and +/- neutral direction. The first row for each pair equals the portion of total HSia towards decreasing water yield [0,100] (yellow to red), while the second row of each pair equals the portion of the HSia towards increasing water yield [0,-100] (yellow to blue). Data is computed in Google Earth Engine and the diagram is created in MATLAB R2019a software.

4. Discussion

Our analysis shows that tree cover loss leads to changes in the hydrologic behavior in all forests and that for each type, a mean critical threshold can be found, leading to changes in the hydrologic regime. This study also shows the speed at which the disturbed area attains complete sensitivity once a threshold in forest cover loss is surpassed, while also detecting if the observed changes in hydrologic

regime increase or decrease water yield and if they are accompanied by warmer or cooler climate conditions. Overall, tropical and boreal forests were among the most hydrologically sensitive to tree cover loss as compared to temperate forests. The former show hydrologic changes occurring at very early stages of tree cover loss (low critical threshold), while temperate forests had to reach around ~50% tree cover loss to surpass the critical threshold, but the speed at which these forests attained complete hydrologic sensitivity occurred much faster compared to boreal and tropical forests. At lower critical thresholds, there is a higher density of tree cover and therefore it will take longer to reach complete hydrologic sensitivity (gradual slope and low speed), while at high critical thresholds, there is lower tree cover left and escalation to full hydrologic sensitivity proceeds abruptly (steep slope and high speed).

In the last decades, deforestation and other land use changes have significantly reduced global terrestrial evapotranspiration resulting in warmer and drier climate conditions (te Wierik et al. 2021) and a reduction in rainfall (Chambers and Artaxo 2017b; Crompton et al. 2021; Kumagai, Kanamori, and Yasunari 2013; Leite-Filho et al. 2021b) and surface water yields for some regions (Domínguez-Tuda and Gutiérrez-Jurado 2021). The most notorious case of this feedback between forest cover loss and water yields is found in tropical rainforests. In those regions, vast canopies pump water from the land into the atmosphere through transpiration which together with surface evaporation from open water bodies contributes to maintaining high atmospheric moisture. This atmospheric vapor returns to the landscape as rainfall in a process known as rainfall recycling that can account for about 30% of the annual precipitation in those areas (Staal et al. 2018). Hence, lower tree cover due to deforestation diminishes the amount of rainfall (Leite-Filho et al. 2021b) and surface water yields in tropical basins. This study shows a mean critical threshold of TCL before significant reductions in water yields occur in tropical forests of ~27% TCL, in agreement with recent reports of a similar threshold (25-30%) for the Amazonia (Leite-Filho et al. 2021b). However, lower than the average critical thresholds are observed

in the Central African (~11% TCL) and Southeast Asian tropical rainforests (~20% TCL), as well as in the Chilean subtropical rainforest (Appendix: Table A6). Possible causes for those extremely low critical thresholds are discussed next.

Low critical thresholds in Tropical and Sub-Tropical Forests.

The mechanisms by which the Congo, Borneo, Sumatra, and sub-tropical Chile forests attain hydrologically sensitive conditions so rapidly after low values of TCL are not well understood. Various leads point to the unique physiographic conditions of such forests making them highly vulnerable to TCL. For example, it has been shown that mountainous terrains with steep slopes are hotspots of hydrologic sensitivity (Domínguez-Tuda and Gutiérrez-Jurado 2021), where high elevation traps atmospheric moisture, enhancing rainfall recycling(van der Ent et al. 2010). These elements coincide with high rates of deforestation of tropical forests in mountainous regions (Zeng et al. 2020) and may explain the low critical threshold values observed in Sumatra (Barisan Mountains) (Zeng et al. 2020), and extratropical tropical Andean Chilean forests (Pabón-Caicedo et al. 2020). Borneo island is also highly mountainous, but low thresholds can also be attributed to the basin having the largest recent increase in forest cover loss rates globally(Hansen et al. 2013b). Borneo has lost half of its forest cover reducing precipitation and leading to drier conditions (Kumagai, Kanamori, and Yasunari 2013). The Congo basin has been identified as one of the regions of the globe where the effects of land surface conditions on regional climate and dynamics are most pronounced (Koster et al. 2004). In this region, deforestation has led to significant decreases in evapotranspiration resulting in increases in surface temperatures and annual precipitation reductions of up to 50% (Nogherotto et al. 2013), explaining the significant reduction in surface water yield. Generally, these results suggest that slight forest perturbations in tropical ecosystems in high-elevation and complex terrain, lead to heightened hydrologic responses and regional warming with some of the greater effects in forests outside the Amazon.

Boreal Forests

Various studies have reported that high-latitude, snow-dominated regions are becoming warmer, changing the length of the growing season in boreal ecosystems and consequently their hydrologic behavior and other important processes for land cover conditions such as forest fire dynamics (Buermann et al. 2013; Debeer et al. 2021; Du et al. 2019). As forest fires increase in boreal forests, changes in their hydrologic behavior are rapidly occurring and recent as well as past works(Valeo, Beaty, and Hesslein 2003; te Wierik et al. 2021) documenting them provide important clues to the observed alterations in their water cycling. However, in this study the impacts of a forest clearing on the direction in which hydrologic changes occur in these ecosystems have not shown a consistent trend: in some cases, water yield increased while in others decreased. Despite showing no clear direction in water yields, these ecosystems report low mean critical thresholds of tree cover loss at ~32% TCL and in most cases resulting in warmer climatic conditions. In general, the contrasting responses in water yield and climate conditions in boreal forests can be a result of multiple factors including bio-physiographic conditions, scale, the intensity of disturbance, and time rates of recovery. For example, variations in the heterogeneity of the different elements of the landscape such as topography, the composition of tree species, stand age, structure, and forest change patterns all affect their hydrologic response; differences in topography where higher elevation slopes with equator-facing aspects are more hydrologically sensitive than lower elevations with polar-facing aspects because ET rates are higher and snow melting is enhanced (M. Zhang et al. 2017b); differences in precipitation regimes where rain-dominated areas are more sensitive than snow-dominated areas to forest cover loss since tree cover loss can produce less impact on runoff on snow-dominated areas. It is also important to consider that TCL's short versus longer-term effects might result in mixed directions in hydrologic trends of boreal forests. For example, the immediate effects of forest clearing leading to warmer trends with increasing water yield can be attributed to significant reductions in

albedo and larger portions of land being directly exposed to incoming solar radiation after the removal of tree cover. Both processes lead to rising surface temperatures, enhancing snowmelt and permafrost thawing favoring runoff conditions (Valeo, Beaty, and Hesslein 2003; Yoshikawa et al. 2003). Additionally, if TCL was the result of a forest fire, this may increase water yield in the short term as some of the immediate impacts of forest clearings result in decreases in canopy interception and evapotranspiration, increases in soils' hydrophobicity, and large reductions in soil water infiltration, thus increasing net precipitation, base-flow, and surface water yield (Valeo, Beaty, and Hesslein 2003). However, depending on their rate (speed) of recovery, water losses due to younger emerging forests with higher ET rates (Aguilos et al. 2021) than mature undisturbed stands can result in decreasing water yields (Valeo, Beaty, and Hesslein 2003). Also, at large scales albedo changes play a major role in defining climate conditions despite the high latitude amplification of CO_2-induced warming. Deforestation and post-replacement of the trees by emerging grasses and shrubs may increase surface albedo resulting in cooler temperatures by up to 0.25 [-] (Bala et al. 2007). The inconsistent trends in water yield directions after TCL of boreal forests beg for more detailed and focused analysis beyond the scope of this current work.

Temperate Forests

Temperate Coniferous, Mediterranean, and Mixed forests have been reported to consistently display increasing water yields as a result of tree cover loss (Gimeno-García, Andreu, and Rubio 2007; Goeking and Tarboton 2020b; Soulis et al. 2021; Vieira et al. 2016; M. Zhang et al. 2017b). This agrees with a review of many studies concluding that water yield increases in these forests after wildfire events. Our study found that wildfire-induced tree cover loss in temperate forests mainly leads to increasing water yield and cooler climate conditions. Cooler temperatures can be attributed to an increase in surface albedo in the disturbed area with higher fractions of terrain exposing brighter surfaces or brighter emerging vegetation (Bala et al. 2007). Similar to previous studies, increasing

water yields in temperate forests following a wildfire are attributed to reduced plant tran, interception-related losses, and decreases in infiltration (from hydrophobic soils) resulting in a higher proportion of rainfall becoming runoff (Goeking and Tarboton 2020b). However, a decrease or no change in water yield in response to wildfire-induced tree cover loss is also reported and can occur when trees are replaced with shrubs with higher leaf area index and higher transpiration rates (Goeking and Tarboton 2020b).

Differences in water yield after TCL in these forests can also be a result of differences in topography, climate, and vegetation patterns. For instance, the topographic aspect controls the effects of trees on snowmelt via their modulation of shortwave radiation (Gutiérrez-Jurado and Vivoni 2013). Wildfires can result in earlier snowmelt relative to unburned stands (Maxwell, Call, and st. Clair 2019). Climate can affect water yield since warmer climate results in more precipitation falling as rainfall rather than snow (Jacobs 2015). Also, warmer temperatures can lead to tree die-off, affecting evapotranspiration patterns and rates.

In general, temperate systems display relatively slow changes to their hydrologic sensitivity to forest cover loss before reaching their critical threshold (~46-53%). However, once they surpass this threshold, the speed at which the forest attains complete hydrologic sensitivity escalates quickly, and in the majority of cases leads to increasing water yield and cooler climate conditions. This agrees with studies that report low hydrologic sensitivity in large temperate forested watersheds (Havel, Tasdighi, and Arabi 2018; M. Zhang et al. 2017b). Similarly, to boreal forests, evidence suggests that variability in hydrologic response in these forests similar to forest types depends on a combination of factors such as vegetation structure, climate, and topography which may result in either an increase or decrease in water yield (Goeking and Tarboton 2020b).

5. Conclusions

Analyses of changes in the hydrologic sensitivity of forests around the world to various degrees of deforestation provided evidence of significant shifts in hydrologic responses to climate variability. We documented hydrologic-regime tipping points in 45 regions across various forest types that underwent extensive tree cover loss induced by either drought, fire, or deforestation during the 2001-2016 period and reported whether the observed changes lead to increasing or decreasing water yield and warmer vs cooler climate conditions. Notably, rapid and substantial changes in the hydrologic regimes of tropical and boreal forests have been detected after TCL events. Tropical systems were the most hydrologically sensitive to tree cover loss and its impact on water yield and climate occurs at the very early stages of tree cover loss (~27%; warmer climate and reduced water yield) followed by Boreal (~32%; warmer climate with both increase and decrease in water yield), and Temperate forests (46-53%; cooler climate and increasing water yield). Our study shows that tree cover loss leads to a decrease in surface water yield and warmer climates in tropical regions with lower-than-average thresholds in Congo, Borneo, Sumatra, and Chilean Andean regions. Since both boreal and tropical forests are hydrologically highly sensitive to tree cover loss and they influence the global climate in multiple ways (Bala et al. 2007), further studies should focus on assessing the effects of forest clearing on hydrologic processes and accounting for different landscape factors.

Code Availability

Code and datasets used to conduct this analysis are available online from our Google Earth Engine link https://code.earthengine.google.com/bb4f526633f21f5a7a68f456090279f8. A MATLAB code and associated data to reproduce the results is available for download in the following open access http://doi.org/10.5281/zenodo.4479716

Author Information

Marisol Domínguez and Hugo A. Gutiérrez-Jurado: These authors contributed equally to this work.

Marisol Dominguez-Tuda

Present address: Department of Earth, Environmental, and Resource Sciences, University of Texas

at El Paso, Texas, United States

Hugo A. Gutiérrez-Jurado
Present address: Department of Earth, Environmental, and Resource Sciences, University of Texas at El Paso, Texas, United States

Contributions
H.A.G. conceived and designed the study. M.D. prepared and processed the data including writing the Google Earth scripts. Both M.D. and H.A.G performed the data analysis, writing and editing of the paper.

Corresponding Author
Correspondence to M. Domínguez and H. A. Gutiérrez-Jurado

Ethics Declaration
The authors declare no competing interests.

References

Aguilos, M., Sun, G., Noormets, A., Domec, J. C., McNulty, S., Gavazzi, M., & Minick, K. (2021). Effects of land-use change and drought on decadal evapotranspiration and water balance of natural and managed forested wetlands along the southeastern US lower coastal plain. *Agricultural and Forest Meteorology*, *303*.

Allen, C. D., Macalady, A. K., Chenchouni, H., Bachelet, D., McDowell, N., Vennetier, M., & Kitzberger, T. (2010). A global overview of drought and heat-induced tree mortality reveals emerging climate change risks for forests. *Forest Ecology and Management*, *259*(4).

Bala, G., Caldeira, K., Wickett, M., Phillips, T. J., Lobell, D. B., Delire, C., & Mirin, A. (2007). Combined climate and carbon-cycle effects of large-scale deforestation. *Proceedings of the National Academy of Sciences of the United States of America*, *104*(16).

Beck, H. E., Wood, E. F., Pan, M., Fisher, C. K., Miralles, D. G., van Dijk, A. I. J. M., & McVicar, T. R. (2019). MSWep v2 Global 3-hourly 0.1° precipitation: Methodology and quantitative assessment. *Bulletin of the American Meteorological Society*, *100*(3).

Birch, C. P. D. (1999). A new generalized logistic sigmoid growth equation compared with the Richards growth equation. *Annals of Botany*, *83*(6).

Budyko, M. (1974). Climate and Life. *Academic Press*.

Buermann, W., Bikash, P. R., Jung, M., Burn, D. H., & Reichstein, M. (2013). Earlier springs decrease peak summer productivity in North American boreal forests. *Environmental Research Letters*, *8*(2).

Chambers, J. Q., & Artaxo, P. (2017). Deforestation size influences rainfall. *Nature Climate Change*, *7*(3).

Creed, I. F., Spargo, A. T., Jones, J. A., Buttle, J. M., Adams, M. B., Beall, F. D., & Booth, E. (2014). Changing forest water yields in response to climate warming: Results from long-term experimental watershed sites across North America. *Global Change Biology*, *20*(10).

Crompton, O., Correa, D., Duncan, J., & Thompson, S. (2021). Deforestation-induced surface warming is influenced by the fragmentation and spatial extent of forest loss in Maritime Southeast Asia. *Environmental Research Letters*, *16*(11).

Crowther, T. W., Glick, H. B., Covey, K. R., Bettigole, C., Maynard, D. S., Thomas, S. M., & Smith, J. R. (2015). Mapping tree density at a global scale. *Nature*, *525*(7568).
Debeer, C. M., Wheater, H. S., Pomeroy, J. W., Barr, A. G., Baltzer, J. L., Johnstone, J. F., & Turetsky, M. R. (2021). Summary and synthesis of Changing Cold Regions Network (CCRN) research in the interior of western Canada - Part 2: Future change in cryosphere, vegetation, and hydrology. *Hydrology and Earth System Sciences*, *25*(4).

Domínguez-Tuda, M., & Gutiérrez-Jurado, H. A. (2021). Global analysis of the hydrologic sensitivity to climate variability. *Journal of Hydrology*, *603*.

Du, J., Watts, J. D., Jiang, L., Lu, H., Cheng, X., Duguay, C., & Farina, M. (2019). Remote sensing of environmental changes in cold regions: Methods, achievements and challenges. In *Remote Sensing*, *11*(16).

Ellison, D., Futter, M. N., & Bishop, K. (2012). On the forest cover-water yield debate: From demand- to supply-side thinking. In *Global Change Biology*, *18*(3).

Feng, M., Sexton, J. O., Huang, C., Anand, A., Channan, S., Song, X. P., & Song, D. X. (2016).

Earth science data records of global forest cover and change: Assessment of accuracy in 1990, 2000, and 2005 epochs. *Remote Sensing of Environment*, *184*.

Giglio, L., Boschetti, L., Roy, D. P., Humber, M. L., & Justice, C. O. (2018). The Collection 6 MODIS burned area mapping algorithm and product. *Remote Sensing of Environment*, *217*.

Gimeno-García, E., Andreu, V., & Rubio, J. L. (2007). Influence of vegetation recovery on water erosion at short and medium-term after experimental fires in a Mediterranean shrubland. *Catena*, *69*(2).

Global Forest Watch. (2018). *Forest monitoring designed for action | Global Forest Watch*. Global Forest Watch.

Goeking, S. A., & Tarboton, D. G. (2020). Forests and water yield: A synthesis of disturbance effects on streamflow and snowpack in Western coniferous forests. In *Journal of Forestry*, *118*(2).

Gorelick, N., Hancher, M., Dixon, M., Ilyushchenko, S., Thau, D., & Moore, R. (2017). Remote Sensing of Environment Google Earth Engine : Planetary-scale geospatial analysis for everyone. *Remote Sensing of Environment*, *202*.

Greve, P., Gudmundsson, L., Orlowsky, B., & Seneviratne, S. I. (2016). A two-parameter Budyko function to represent conditions under which evapotranspiration exceeds precipitation. *Hydrology and Earth System Sciences*, *20*(6).

Gutiérrez-Jurado, H. A., & Vivoni, E. R. (2013). Ecogeomorphic expressions of an aspect-controlled semiarid basin: I. Topographic analyses with high-resolution data sets. *Ecohydrology*, *6*(1).

Hansen, M. C., Potapov, P. v., Moore, R., Hancher, M., Turubanova, S. A., Tyukavina, A., & Thau, D. (2013). High-resolution global maps of 21st-century forest cover change. *Science*, *342*(6160).

Havel, A., Tasdighi, A., & Arabi, M. (2018). Assessing the hydrologic response to wildfires in mountainous regions. *Hydrology and Earth System Sciences*, *22*(4).

Helman, D., Lensky, I. M., Yakir, D., & Osem, Y. (2017). Forests growing under dry conditions have higher hydrological resilience to drought than do more humid forests. *Global Change*

Jacobs, B. F. (2015). Restoration of degraded transitional (piñon-juniper) woodland sites improves ecohydrologic condition and primes understory resilience to subsequent disturbance. *Ecohydrology*, *8*(8).

Koster, R. D., Dirmeyer, P. A., Guo, Z., Bonan, G., Chan, E., Cox, P., & Gordon, C. T. (2004). Regions of strong coupling between soil moisture and precipitation. *Science*, *305*(5687).

Kumagai, T., Kanamori, H., & Yasunari, T. (2013). Deforestation-induced reduction in rainfall. *Hydrological Processes*, *27*(25).

Lawrence, D., & Vandecar, K. (2015). Effects of tropical deforestation on climate and agriculture. In

Nature Climate Change, *5*(1)

Leite-Filho, A. T., Soares-Filho, B. S., Davis, J. L., Abrahão, G. M., & Börner, J. (2021). Deforestation reduces rainfall and agricultural revenues in the Brazilian Amazon. *Nature Communications*, *12*(1).

Malhi, Y., Roberts, J. T., Betts, R. A., Killeen, T. J., Li, W., & Nobre, C. A. (2008). Climate change, deforestation, and the fate of the Amazon. *Science*, 319 (5860).

Marengo, J. A., Souza, C. M., Thonicke, K., Burton, C., Halladay, K., Betts, R. A., & Alves, L. M. (2018). Changes in Climate and Land Use Over the Amazon Region: Current and Future Variability and Trends. In *Frontiers in Earth Science*, *6*.

Maxwell, J. D., Call, A., & st. Clair, S. B. (2019). Wildfire and topography impact on snow accumulation and retention in montane forests. *Forest Ecology and Management*, *432*.

Nogherotto, R., Coppola, E., Giorgi, F., & Mariotti, L. (2013). Impact of Congo Basin deforestation on the African monsoon. *Atmospheric Science Letters*, *14*(1).

Pabón-Caicedo, J. D., Arias, P. A., Carril, A. F., Espinoza, J. C., Borrel, L. F., Goubanova, K., & Lavado-Casimiro, W. (2020). Observed and Projected Hydroclimate Changes in the Andes. In *Frontiers in Earth Science*, *8*.

Pimentel, R., & Arheimer, B. (2021). Hydrological impacts of a wildfire in a Boreal region: The Västmanland fire 2014 (Sweden). *Science of the Total Environment*, *756*.

Roderick, M. L., Sun, F., Lim, W. H., & Farquhar, G. D. (2014). A general framework for understanding the response of the water cycle to global warming over land and ocean. *Hydrology and Earth System Sciences*, *18*(5).

Running, S., Mu, Q., Zhao, M., & Moreno, A. (2017). MOD16A2 MODIS/Terra Net Evapotranspiration 8-Day L4 Global 500m SIN Grid V006 [Data set]. *NASA EOSDIS Land Processes DAAC*, *1.5*.

Sheil, D. (2018). Forests, atmospheric water and an uncertain future: the new biology of the global water cycle. In *Forest Ecosystems*, *5*(1).
Sinha, J., Jha, S., & Goyal, M. K. (2019). Influences of watershed characteristics on long-term annual and intra-annual water balances over India. *Journal of Hydrology*, *577*.

Soulis, K. X., Generali, K. A., Papadaki, C., Theodoropoulos, C., & Psomiadis, E. (2021). Article hydrological response of natural mediterranean watersheds to forest fires. *Hydrology*, *8*(1).

Spracklen, D. v., & Garcia-Carreras, L. (2015). The impact of Amazonian deforestation on Amazon basin rainfall. *Geophysical Research Letters*, *42*(21).

Staal, A., Tuinenburg, O. A., Bosmans, J. H. C., Holmgren, M., van Nes, E. H., Scheffer, M., Zemp, D. C., & Dekker, S. C. (2018). Forest-rainfall cascades buffer against drought across the Amazon.

Nature Climate Change, *8*(6).

te Wierik, S. A., Cammeraat, E. L. H., Gupta, J., & Artzy-Randrup, Y. A. (2021). Reviewing the Impact of Land Use and Land-Use Change on Moisture Recycling and Precipitation Patterns. *Water Resources Research*, *57*(7), 1–19.

Trenberth, K. E. (2011). Changes in precipitation with climate change. *Climate Research*, *47*(1–2). Valeo, C., Beaty, K., & Hesslein, R. (2003). Influence of forest fires on climate change studies in the central boreal forest of Canada. *Journal of Hydrology*, *280*(1–4).

van der Ent, R. J., Savenije, H. H. G., Schaefli, B., & Steele-Dunne, S. C. (2010). Origin and fate of atmospheric moisture over continents. *Water Resources Research*, *46*(9).

Vieira, D. C. S., Malvar, M. C., Fernández, C., Serpa, D., & Keizer, J. J. (2016). Annual runoff and erosion in a recently burn Mediterranean forest – The effects of plowing and time-since-fire. *Geomorphology*, *270*.

Watch, G. F. (2020). *Forest monitoring designed for action*. https://www. globalforestwatch. org, 2020.

Xu, X., Zhang, X., Riley, W. J., Xue, Y., Nobre, C. A., Lovejoy, T. E., & Jia, G. (2022). Deforestation triggering irreversible transition in Amazon hydrological cycle. *Environmental Research Letters*, *17*(3).

Yoshikawa, K., Bolton, W. R., Romanovsky, V. E., Fukuda, M., & Hinzman, L. D. (2003). Impacts of wildfire on the permafrost in the boreal forests of interior Alaska. *Journal of Geophysical Research: Atmospheres*, *108*(1).

Zeng, Z., Wang, D., Yang, L., Wu, J., Ziegler, A. D., Liu, M., & Ciais, P. (2020). Deforestation-induced warming over tropical mountain regions regulated by elevation. *Nature Geoscience 2020 14:1*, *14*(1), 23–29.

Zhang, M., Liu, N., Harper, R., Li, Q., Liu, K., Wei, X., & Ning, D. (2017). A global review on hydrological responses to forest change across multiple spatial scales: Importance of scale, climate, forest type and hydrological regime. *Journal of Hydrology*, *546*.

Zhang, Y., Kong, D., Gan, R., Chiew, F. H. S., McVicar, T. R., Zhang, Q., & Yang, Y. (2019). Coupled estimation of 500 m and 8-day resolution global evapotranspiration and gross primary production in 2002–2017. *Remote Sensing of Environment*, *222*.

APPENDIX

TABLE A1: Documented cases of drought and or wildfire induced tree cover loss in Boreal Forests.

ID	Event/Location	Years of Mortality	Biome Type	Dominant Taxa	Cimate Anomally	Scale of Impact (ha)	Reference
1	Russia (Northwest)	2004-2006	Boreal Forest	*Picea obovata*	Multi-year drought;high temperatures	1.9 M	Krotov 2007, Tvetkov and Tvetkov., 2007
2	Taylor Complex Fire/Alaska	2004	Boreal Forest	*Picea mariana (Mill.)*	Wildfire	53,000	Ge et al., 2014
3	Caribou Hills Fire/Alaska	2007	Boreal Forest	*Picea mariana (Mill.)*	Wildfire	22,400	Makoto et al., 2013
4	Minto Flats Fire/ Alaska	2009	Boreal Forest	*Picea mariana (Mill.)*	Wildfire	120,000	Madden, 2015
5	Quebec Wildfires/Canada (La Tuque)	2010	Boreal Forest	*Picea glauca; bies balsamea*	Wildfire	90,000	Gaudreau, 2016
6	Richardson Backcountry Fire/Fort Mcmurray Alberta, Canada	2011	Boreal Forest	*Picea glauca;Populus tremuloides;Populus balsamifera;*	Wildfire	700,000	Bytnerowicz et al., 2016
7	Slave Lake Fire/ Alberta, Canada	2011	Boreal Forest	*Populus tremuloides;Populus balsamifera*	Wildfire	4,700	Kulig, 2012
8	Northwest Territories Fire/Canada	2014	Boreal Forest	*Picea mariana;Larix laricina;Pinus banksiana;Populus tremuloides*	Wildfire	3.5 M	Kochtubajada et al., 2019
9	Vastmandland Wildfire/ Sweden	2014	Boreal Forest	*P. sylvestris;P.abies*	Wildfire	15,000	Pimentel et al., 2020

TABLE A2: Documented cases of drought and or wildfire forest induced tree cover loss in Temperate Coniferous Forests.

ID	Event/Location	Years of Mortality	Biome Type	Dominant Taxa	Climate Anomaly	Scale of Impact	Reference
10	Tripod Complex Fire/ Washington, USA	2006	Temperate Coniferous Forests	*Abies lasiocarpa;L. lyallii;P. albicaulis*	Wildfire	71,000	Prichard, 2009
11	Bugaboo Scrub Fire/Florida, USA	2007	Temperate Coniferous Forests	*Lyonia lucida; Cupressus*	Wildfire	190,000	Lopiano, 2014
12	Cold Springs fire/Washington, USA	2008	Temperate Coniferous Forests	*Pinus contorta, Pseudotsuga menziesii,pinus ponderosa*	Wildfire	2,300	Hummel, 2013
13	Evans Road Fire/ North Carolina, USA	2008	Temperate Coniferous Forests	*Pinus ponderosa*	Wildfire	17,000	Reardon, 2011
14	Trigo New Mexico/ New Mexico,USA	2008	Temperate Coniferous Forests	*Pinus ponderosa;pinus(pinyon group);juniperus;quercus gambelii*	Wildfire	5,548	Amato, 2013
15	California wildfires/ N. California, USA	2008	Temperate Coniferous Forests plus Grasslands/Savanna	*Pinus ponderosa*	Wildfire	650,000	Reid, 2016
16	West Kelowna wildfires/ British Columbia, Canada	2009	Temperate Coniferous Forests	*Pinus ponderosa*	Wildfire	9,877	Jordan, 2011
17	Tumblebug Complex Fire/ Oregon, USA	2009	Temperate Coniferous Forests	*Pseudotsuga menziesii*	Wildfire	5,900	Kulseth, 2019
18	Binta Lake Fire/Bristish Columbia, Canada	2010	Temperate Coniferous Forests	*Pinus contorta var. latifolia*	Wildfire	40,000	Krawchuk, 2006
19	Wallow Fire/ Arizona, USA	2011	Temperate Coniferous Forests	*Pseudotsuga menziesii;Abies concolor var. concolor*	Wildfire	218,000	Kennedy, 2014
20	Colorado Wildfires/Colorado, USA	2012	Temperate Coniferous Forests	*Pinus ponderosa;Picea engelmannii*	Wildfire	99,800	Coen, 2015

21	USA(Colorado)	2005-2006	Temperate Coniferous Forest	*Populus tremuloides*	Multi-year drought	58,374	Worral et al., 2008
22	Whitewater-Baldy Complex/ New Mexico	2012	Temperate Coniferous Forests	*Pinus ponderosa;Populus tremuloides;Picedae and pinyon group*	Wildfire	120,500	Tillery, 2012
23	Beaver Creek Fire/ Fairfield, Idaho, USA	2013	Temperate Coniferous Forests	*Pinus ponderosa; Juniperus ssp.*	Wildfire	46,500	Skinner, 2013

TABLE A3: Documented cases of drought and or wildfire-induced tree cover loss in Temperate Broadleaf and Mixed Forests.

ID	Event/Location	Years of Mortality	Biome Type	Dominant Taxa	Climate Anomally	Scale of Impact	Reference
24	USA(Minnesota)	2004-2007	Temperate Broadleaf & Mixed Forest	*Populus tremuloides,Fraxinus spp.*	Multi-year drought	not reported	Minnesota Dept. Nat. Resources., 2007
25	Pulletop Bushfire/ New South Wales, Australia	2006	Temperate Broadleadf & Mixed Forests w/ Montane Grasslands	*Eucalyptus socialis, E. dumosa, and E. gracilis*	Wildfire	9,000	Rahman, 2018
26	Black Saturday bushfires/ Victoria, Australia	2009	Temperate Broadleaf & Mixed Forest	*Sclerophyllous Eucalyptus*	Wildfire	450,000	Cruz, 2012
27	Pagami Creek Fire/Minnesota, USA	2011	Temperate Broadleadf & Mixed Forests	*Pinus banksiana; Picea Mariana*	Wildfire	37,500	Kolka, 2017
28	Duck Lake Fire/ Michigan, USA	2012	Temperate Broadleadf & Mixed Forests	*Pinus banksiana;Picea glauca;Abies balsame*	Wildfire	8,900	White, 2018

TABLE A4: Documented cases of drought and or wildfire-induced tree cover loss in Mediterranean Woodlands and

Scrub.

ID	Event/Location	Years of Mortality	Biome Type	Dominant Taxa	Climate Anomaly	Scale of Impact	Reference
29	France (South, Maures Mtn)	2006-2008	Mediterranean Forest, Woodlands & Scrub	*Quercus suber*	Multi-year drought	120,000	Vennetier et al., 2008
30	Greek forest fires/Greece	2007	Mediterranean Woodlands & Scrub	*Sclerophyllous; Pinus halepensis, Pinus brutia*	Wildfire	271,000	Turquety, 2009
31	Kangaroo Island bushfires/Australia	2007	Mediterranean Woodlands & Scrub	*Eucalyptus cneorifolia*	Wildfire	95,000	Peace, 2012
32	Chios Island/ Greece	2012	Mediterranean Woodlands & Scrub	*Pinus halepensis, Olea europea; sclerophyllous; Pinus pinea*	Wildfire	7,000	Adaktylou, 2020
33	Spain (South)	2004-2006	Mediterranean Woodlands & Scrub	*Pinus sylvestris, Pinus nigra*	Multi-year drought	13,304	Navarro-Cerrillo et. al.,2007

TABLE A5: Documented cases of drought and deforestation-induced tree cover loss in Tropical Rainforests.

ID	Event/Location	Years of Mortality	Biome Type	Dominant Taxa	Disturbance mechanism	Scale of Impact (ha)	Reference
34	Brazil(Amazon basin)	2005	Tropical & Subtropical Moist Broadleaf forest	*Not reported*	Single-year drought and severe deforestation	subcontinental	Phillips et al., 2005 https://www.globalforestwatch.org/dashboards/country/BRA
35	Brazil(Amazon basin)	2010	Tropical & Subtropical Moist Broadleaf forest	*Not reported*	Single-year drought and severe deforestation	subcontinental	Lewis et al., 2011 https://www.globalforestwatch.org/dashboards/country/BRA
36	Brazil(Amazon basin)	2015-2016	Tropical & Subtropical Moist Broadleaf forest	*Not reported*	Multi-year drought and severe deforestation	subcontinental	Panisset et al., 2018; Jiménez-Muñoz, et al., 2016 https://www.globalforestwatch.org/dashboards/country/BRA
37	Equatorial Guinea	2014-2016	Tropical & Subtropical Moist Broadleaf forest	*Not reported*	Severe multi-year deforestation	36,140	https://www.globalforestwatch.org/dashboards/country/GNQ
38	Australia (Eastern Australia)	2007-2009	Tropical & Subtropical Moist Broadleaf forest	*Not reported*	Severe multi-year deforestation	777,000	https://www.globalforestwatch.org/dashboards/country/AUS
39	Democratic Republic of Congo (Congo Basin)	2014-2016	Tropical & Subtropical Moist Broadleaf forest	*Not reported*	Severe multi-year deforestation	3.6M	https://www.globalforestwatch.org/dashboards/country/COD
40	Sumatra (major provinces)	2011-2013	Tropical & Subtropical Moist Broadleaf forest	*Not reported*	Severe multi-year deforestation	2.04M	https://www.globalforestwatch.org/dashboards/country/IDN IDN8,24,30,31,32
41	Sumatra (Riau)	2014-2016	Tropical & Subtropical Moist Broadleaf forest	*Not reported*	Severe multi-year deforestation	827,000	https://www.globalforestwatch.org/dashboards/country/IDN/24
42	Cambodia	2010-2012	Tropical & Subtropical Moist Broadleaf forest	*Not reported*	Severe multi-year deforestation	626,000	https://www.globalforestwatch.org/dashboards/country/KHM
43	Indonesia and Malaysia (Borneo basin)	2012-2014	Tropical & Subtropical Moist Broadleaf forest	*Not reported*	Severe multi-year deforestation	3.13 M	https://www.globalforestwatch.org/dashboards/country/IDN

							IDN/11,12,13,14,15 MYS/13,14
44	Mekong Region (Laos, Cambodia, and Vietnam)	2010-2012	Tropical & Subtropical Moist Broadleaf forest	*Not reported*	Severe multi-year deforestation	1.5M	https://www.globalforestwatch.org/dashboards/country/ LAO , KHM, VNM
45	Chile	2012-2014	Tropical & Subtropical Moist Broadleaf forest	*Not reported*	Severe multi-year deforestation	396,000	https://www.globalforestwatch.org/dashboards/country/CHL

Figure A1-A5: Hydrologic sensitive area against tree cover loss for all 45 events. Grouped by forest

type with mean value (red dashed line).

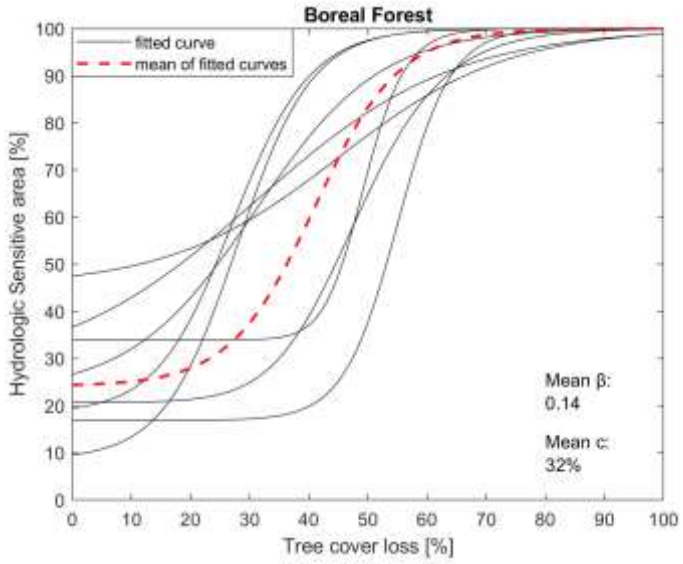

Figure A1: HSia against TCL for Boreal Forests.

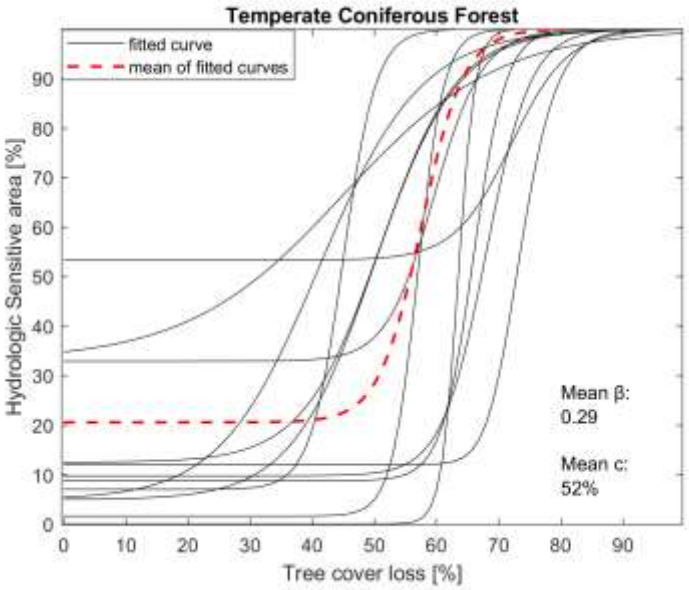

Figure A2: HSia against TCL for Temperate Coniferous Forests.

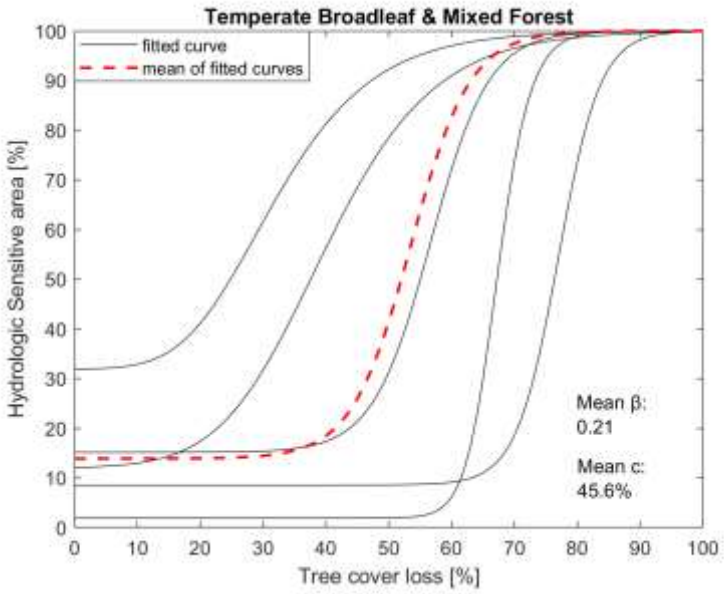

Figure A2: HSia against TCL for Temperate Broadleaf & Mixed Forests.

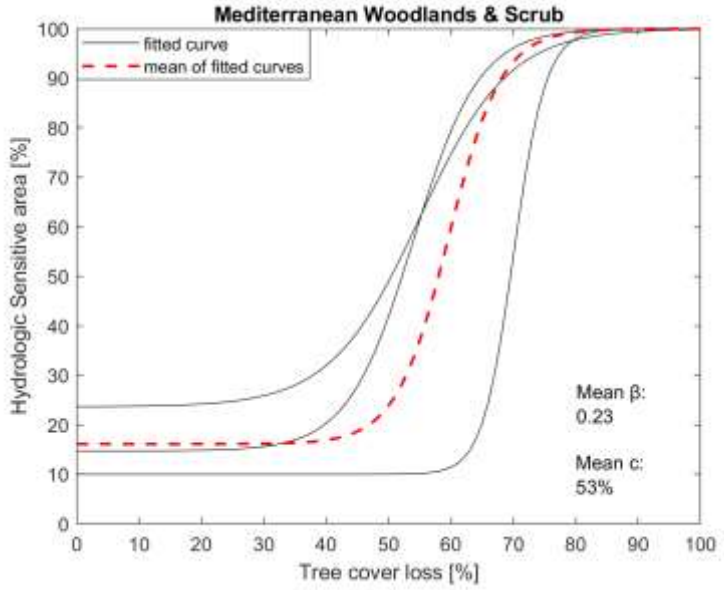

Figure A4: HSia against TCL for Mediterranean Woodlands and Scrub..

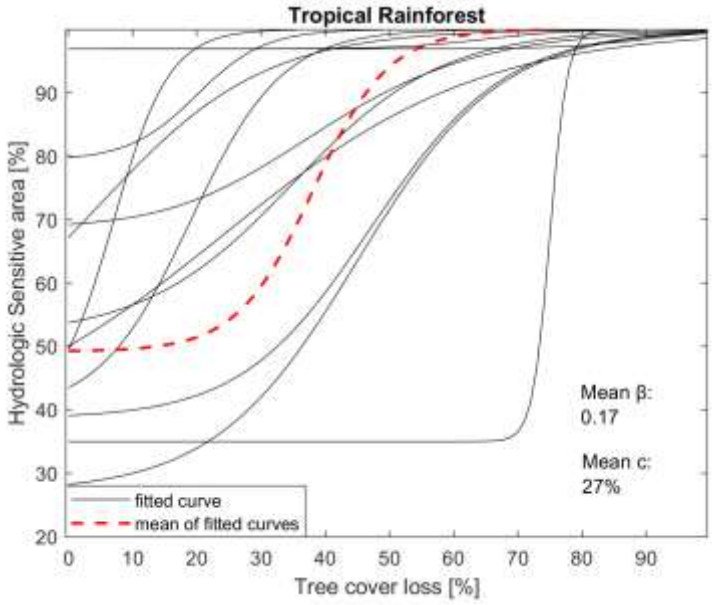

Figure A5: HSia against TCL for Tropical Rainforest..

TABLE A6: Richard's curve parameters for all events. Note: Event IDs with No Data values are due to irregular patterns in diagrams not approachable with Richards's growth function. α=100%

ID	δ (initial value, HSia, %)	γ	B (rate of sensitivity)	c (critical point, tree cover loss, %)
	Boreal Forests			
1	16.8704	55	0.22	49
2	22.81485	31	0.095	30
3	26.77	35	0.06	13
4	8.5426	28	0.16	20
5	33.92261	49	0.263	44
6	18.48	27	0.15	18
7	-	-	-	-
8	20.668	47	0.12	36
9	45.26	68	0.077	43
Mean	**24**	**42.5**	**0.14**	**31.625**
Median	**21.7**	**41**	**0.135**	**33**

	Temperate Coniferous Forest			
10	9.77	68	0.23	68
11	12.048	73	0.3	69
12	-	-	-	-
13	53.33641	72	0.22	66
14	1.652	57	0.48	54
15	4.6948	50	0.15	41
16	32.937	59.5	0.25	54
17	8.798915	60	0.39	63
18	-	-	-	-
19	7.03994	45	0.38	41
20	12.5	51	0.16	43
21	5	41	0.12	30
22	33.038	45	0.08	33

23	0.0467	63.5	0.75	62
Mean	**15.07**	**57.1**	**0.29**	**52**
Median	**9.28**	**58.25**	**0.24**	**54**
	Mixed Forests			
24	1.9426	67	0.35	63
25	8.58	77	0.3	73
26	11.93385	38	0.10	25
27	15.14295	56.7	0.217	51
28	31.88	29	0.1	16
Mean	**16.8**	**59.9**	**0.23**	**45.6**
Median	**11.93**	**567**	**0.217**	**51**

	Mediterranean Forests			
29	-	-	-	-
30	9.9811	70	0.38	66
31	-	-	-	-
32	23.6354	55	0.14	46
33	14.7\18	54	0.19	47
Mean	**13.9**	**53.5**	**0.21**	**53**
Median	**16.8**	**55**	**0.19**	**47**
	Tropical Rainforests			
34	44.6813	75	0.75	73
35	38.634899	47	0.093	33
36	26.99423	45	0.09	30
37	79.32848	20	0.19	13
38	1.39394	64	0.23	58
39	39.51665	19	0.14	10
40	70.12595	21	0.11	9
41	96.8998	65	0.15	56

42	68.70332	37	0.07	18
43	45	5	0.078	0
44	53.7	35	0.086	20
45	35	24	0.05	0
Mean	**50**	**38.1**	**0.17**	**26.6**
Median	**44.8**	**36**	**0.10**	**19**

Chapter 3: Hydrologic sensitivity in Amazonia ecoregions to drought-induced tree cover loss.

Abstract

We know that different ecosystems are affected differently by climate variability. However, the Amazon basin has been studied as a homogenous ecosystem, although it contains a heterogenous landscape divided up into 30 different ecoregions. Thus, the impacts of forest disturbance on hydrologic responses may vary across the basin. Identifying the impact of extreme drought in different Amazonia ecoregions leading to unstable hydrologic behavior is important to understanding the role different vegetation species have in water cycling dynamics and identify locations of hydrologic sensitivity under extreme climate events. Here, we use the hydrologic sensitivity index that measures hydrologic responses to climate variability, to document the most hydrologically sensitive ecoregions within the basin and report the differences in response to the most recent extreme Amazon drought events (Amazon droughts in 2005, 2010, and 2015). Also, we document anomalies in vegetation greenness as a proxy for the transpiration process for each drought event against a historical mean for sensitive ecoregions using the improved nonlinear-generalized version of the normalized difference vegetation index (kNDVI). We identify clusters of hydrologic sensitivity areas within north, northwestern, and southwestern ecoregions. We observe negative anomalous values of transpiration in the majority of ecoregions during the consequent year of drought. Ultimately, we identify which parts of the Amazon basin are closer to reaching a critical threshold that may lead to irreversible changes in ecosystem services and water dynamics and which vegetation communities need urgent conservation strategies.

1. Background

The Amazon is one of the most important elements maintaining the stability of the Earth system, and it constitutes the world's most biodiverse and water-yielding basin. However, climate warming and extreme weather events have led to forest cover loss resulting in decreasing water yields (Dominguez-Tuda & Gutierrez-Jurado, 2021). Moreover, the Amazon basin is divided into ecoregions characterized by different plant communities, which have been exposed to novel environmental conditions that are beyond the range to which they are adapted. Although specific plant communities may have evolved resilience to extreme weather events and climate change, the fact that water availability is highly dependent on the thriving of forest vegetation, since a major part of rainfall is recycled within the basin through plant transpiration (Ellison, 2012), an assessment evaluating their role in hydrologic responses in the Amazon basin has not been completed.

In the last two decades, the Amazon Rainforest has been impacted by increasingly intense and frequent droughts, leading to major forest cover loss with a slow rate of recovery. Specifically, the most recent and severe drought events in Amazon history occurred in 2005, 2010, and 2015, leading to tree death affecting 40% to 80% of the basin, with each event worse than the previous one (Panniset, 2018). Also, reduced rainfall or drought events have an amplifying effect resulting in further tree cover loss (reference of amplifying), and some species might be able to adapt better than others giving us information on which will thrive in the future and how patterns of migration may occur. Given the dependence of water security and ecosystems services on plant community evolution (Becklin, 2016) and the increasing droughts events, defining tipping points of tree cover loss leading to high hydrologic sensitivity across different ecoregions within the basin, will help in identifying the most vulnerable ecosystems that regulate Amazon services to prioritize and trigger specific solutions to maintaining forest health and productivity. Also, we will be able to understand the role that different vegetation species play in Amazon hydrology, and which are expected to thrive

in the future.

2. Methods

2.1 Defining the Amazon ecoregions

An ecoregion is defined as a large unit of land or water containing a geographically distinct assemblage of species, natural communities, and environmental conditions (WWF; Oslon, 2001). The Amazon basin contains ecoregions that include rainforests, seasonal forests, deciduous forests, flooded forests, bamboo stands, palm forests, savannas, dry forests, and cloud forests which are all included in this assessment. Figure 1 displays Amazon ecoregions that were obtained from the World Wildlife Fund (WWF; Oslon, 2001). Figure 2a-c displays the method for discriminating the Amazon ecoregions affected by drought. Figure 3a displays the reference images obtained from Panniset, 2018 that defines the drought or affected area based on values reporting negative anomalies in precipitation, higher than normal land surface temperatures, and solar radiation within the basin. Figure 3b, displays the same boundaries as in Figure 3a but is drawn out as a shapefile for data processing using ArcMap10.7.1. Figure 2c displays the intersection between the drought area (Figure 3b) and the Amazon ecoregion (Figure 1) so that the resulting shapefiles for data processing are the Amazon ecoregion portion affected by drought.

Table 1: Data Collection. List of products with temporal and spatial resolution used to evaluate HSi.

Figure 1: Amazon ecoregions. Obtained from the Forest Ecoregions World Wildlife Fund (WWF). Image created in ArcMap10.7.1.

2.2 Delimiting the affected area for each drought event.

Figure 3a-c displays the method used to define the affected area for each drought event in order to consider only that area for each ecoregion. Figure 3a displays the reference images obtained from a previous study that defines the drought or affected area based on values reporting negative anomalies in precipitation (Panniset, 2018), higher than normal land surface temperatures, and solar radiation within the basin. Figure 3b, displays the same boundaries as in Figure 3a but is drawn out as a shapefile for data processing using ArcMap10.7.1. Figure 3c displays the intersection between the drought area (Figure 3b) and the Amazon ecoregion so that the resulting shapefiles for data processing are the Amazon ecoregion portion affected by drought. Table 2 displays the characteristics of each of the 3 drought events and the meteorological variables and drivers of drought for each

extreme drought event.

2.3 Computing HSia and percent tree cover loss

To evaluate the effect of forest loss on hydrologic sensitivity in different vegetation types within the Amazon basin, we first compute the hydrologic sensitive area (HSia). The Hydrologic Sensitive Index (HSi) is used to evaluate hydrologic responses to climate variability within deforested areas. By taking the 3-yr average post- and 3-yr average pre-disturbance periods for the 3 different droughts occurring during 2005, 2010, and 2015, we are able to evaluate HSi for each grid cell. The Hydrologic Sensitive area (HSia) is defined by the portion of grid cells (with tree cover loss >0%) with HSi value>1 relative to the entire area of the affected ecoregion. Percent tree. The HSia is computed and plotted against intervals of 10% tree cover loss. Percent tree cover loss (TCL) is computed by taking the difference for each pair of available years of percent tree cover (every 5-years) globally. That is, TCL is computed by taking the difference in percent tree cover between the years 2000, 2005, 2010, and 2015. Depending on the year(s) of disturbance the pair of years of annual values are selected.

The HSi index is computed as a ratio of change hydrologic response (ΔEI_R) of a location or region relative to Budyko's curve or historical average (B_A), to climatic variability before and after tree cover loss (ΔDI). This index is computed in disturbed regions in the following manner:

$$\mathbf{HSi} = \frac{\mathbf{\Delta EI_R}}{\mathbf{\Delta DI}} = \left| \frac{EI_{R_{disturbed(3-yr)}} - EI_{R_{undisturbed(3-yr)}}}{(DI_{disturbed(3-yr)} - DI_{undisturbed(3-yr).})} \right|, \quad (1)$$

$$\text{where } EI_R = EI - B_A$$

$$\mathbf{HSia} = \left| \frac{\text{Grid Cells in disturbed area with HSi>1}}{\text{Total Grid Cells in disturbed area}} \right|, \quad (2)$$

where sensitive regions will display HSi>1, and resilient locations will show HSi ≤1 (Equation 2. All computations leading to HSi are carried out in the Google Earth Engine platform (Gorelick et al., 2017). More detail for equation (Chapter 2 Methods Section). By plotting HSia [0,100] against TCL

[0,100] for each ecoregion, these display a growth trend. This trend is approximated using Richards curve function (Chapter 2, Methods section). The critical threshold, *c*, is obtained by plotting the second derivative of the Richards curve function (Figure 2). Since the maximum acceleration critical threshold, c1, oscillates between similar values at around ~0-10 %, it is not used to distinguish the most sensitive ecoregions (Figure 4a-c). The maximum deceleration critical threshold, c2, is useful to identify the most sensitive ecoregions since values vary and it indicates those which regions that arrive at a complete HSia (y-axis) at very early stages of tree cover loss. The c2 is computed for all ecoregions and for each drought and is used to select the top 11 most sensitive ecoregions and is also used to list the ecoregions from least to greatest hydrologic sensitivity.

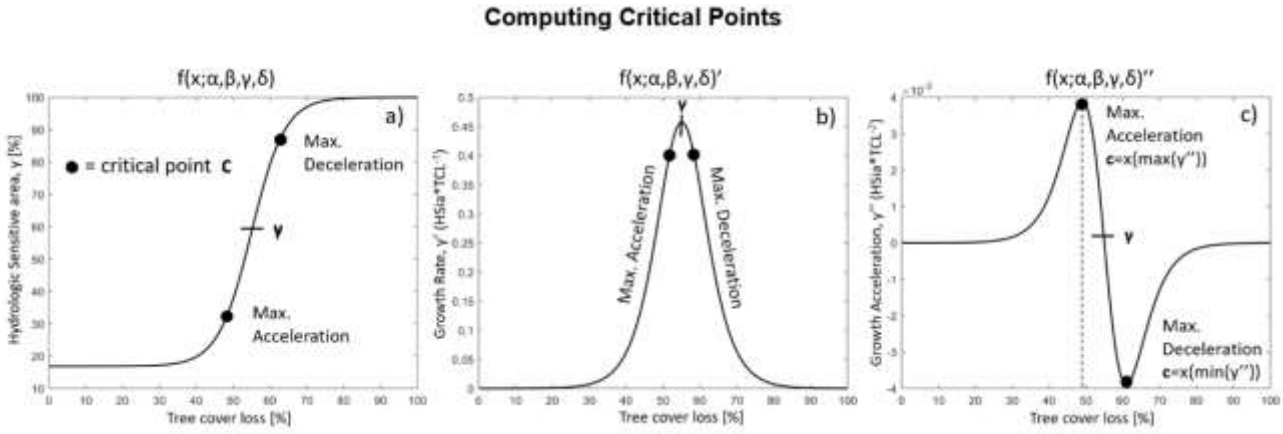

Figure 2. (a-c) Step-by-step computation of critical threshold. Illustration showing how critical points were obtained by numerically computing Richard's function derivatives. 2a) Original Richard's Curve function; 2b) First derivative of Richard's function; 2c) Second derivative of Richard's function: The critical points used in this study are those in which maximum deceleration is attained, the c2=x value when y'' is at its minimum.

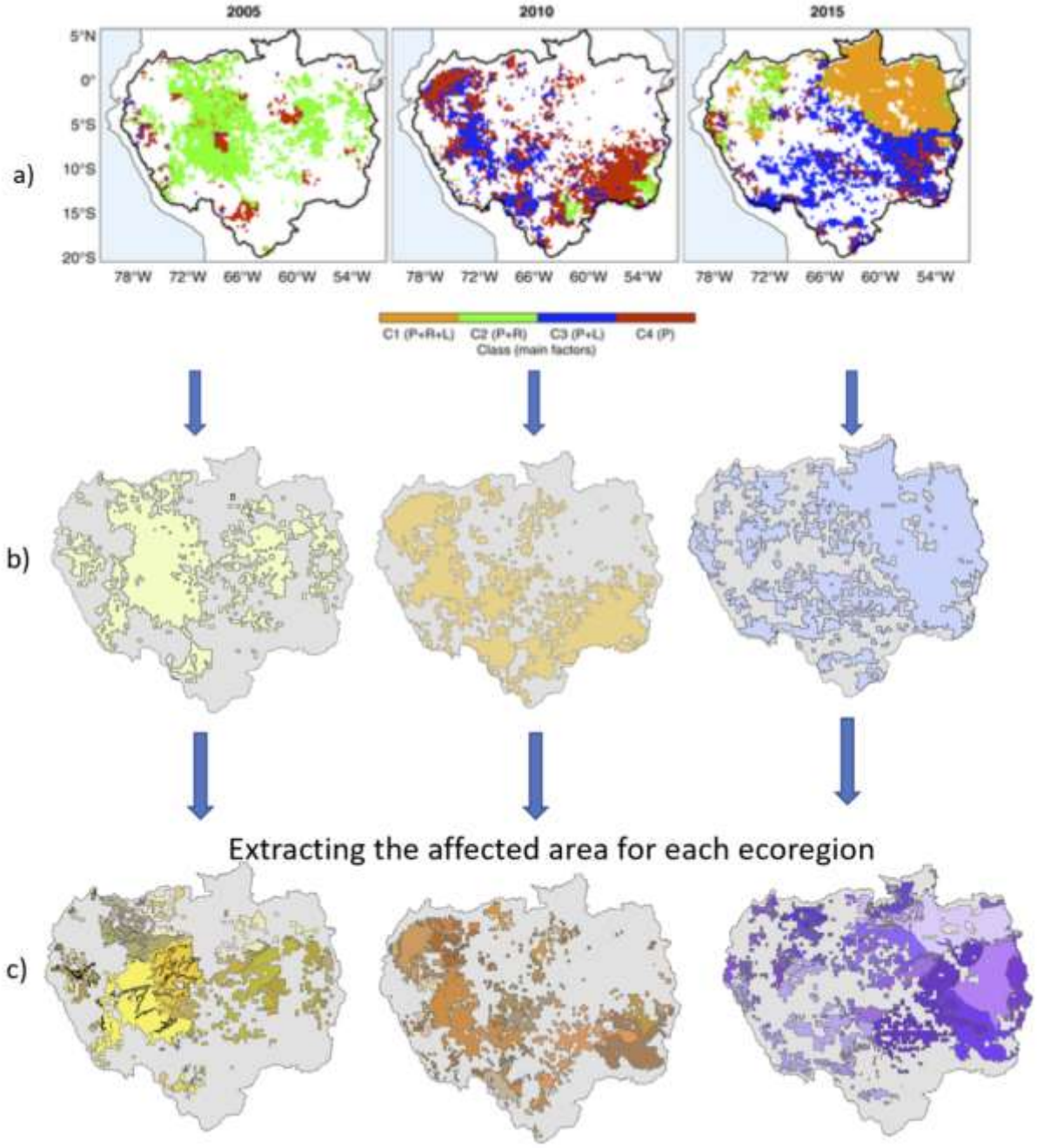
2005
2010
2015
a)
5°N
0°
5°S
10°S
15°S
20°S
78°W
72°W
66°W
60°W
54°W
C1 (P+R+L)
C2 (P+R)
C3 (P+L)
C4 (P)
Class (main factors)
b)
Extracting the affected area for each ecoregion
c)

Figure 3 a-c. Amazon drought area. Shapefiles created for data processing. From left to right displays the Amazon drought extent from 2005, 2010, and 2015 where **a)** displays the reference images where the drought area occurred; **b)** displays the polygons drawn out in ArcMap 10.7.1, and **c)** displays intersection of between the Amazon ecoregions and drought area and below the respective legends for each.

2.4 Time series for observing anomalies in Vegetation

After identifying the hydrologically sensitive ecoregions in the Amazonia basin, we evaluate the changes in vegetation for each system to distinguish the magnitude of response relative to the historical average during 2002-2019 period. We use the nonlinear generalization of the normalized difference vegetation index (kNDVI), which is the improved version of NDVI (Camps-Valls et al., 2021). We compute kNDVI as

$$kNDVI=\tanh(NDVI^2) \quad (3),$$

where NDVI is obtained from MODIS at 250m resolution (MOD13Q1.061 Terra Vegetation Indices 16-day Global). Since kNDVI is also a proxy for measuring the fraction of total solar radiation absorbed by living plants for photosynthetic activity (FAPAR), it is also useful for measuring changes in transpiration, as both of these parameters are coupled (occur at the same moment and their values are interrelated). Specifically, the opening of stomata (pores of leaves) is the process through which the plant can permit solar radiation to be absorbed, while at the same time, the water inside the stomata is released to the atmosphere (transpiration). Thus, a change in kNDVI also reflects a change in transpiration of the same magnitude. In other words, if kNDVI decreases, there is no photosynthetic activity, which in turn declines transpiration response. In the face of drought, we expect to detect negative anomalies in kNDVI for the majority of ecoregions. Thus, by plotting the time series of kNDVI for the sensitive ecoregions during drought years, relative to a historical mean, we are able to identify the magnitude of the changes in transpiration. We include three maps to display these anomalies at basin-wide scale (entire Amazon basin) for each drought event.

2.5 Data Collection

Table 1 displays the characteristics for each of the 3 drought events and the meteorological variables and drivers of drought for each extreme drought event. The drought of 2005/06 was mainly driven by the elevated warming in the tropical North Atlantic Ocean, with a precipitation deficit of +1.8 standard deviation (SD) during June-September period. The drought mainly affected the western and southwestern Amazon, representing 37.9% of the area and tree cover loss equivalent to a release of $1.6x10^{15}$ g of carbon (Panniset et al., 2018). The drought of 2010/11 was a result of elevated warming sea surface temperatures in the Atlantic and Pacific Ocean resulting in more severe conditions compared to 2005, with a precipitation deficit of +2.1 SD during June-September period (Panniset et al., 2018). The drought affected western, southwestern, and southeastern Amazon representing 43% of the area and tree cover loss equivalent to $2.2x10^{15}$ g of carbon. The drought of 2015/16 was driven by elevated warming of Atlantic and Pacific resulting in more severe conditions than 2005 and 2010 drought with a precipitation deficit of +3.5 SD. The drought affected 80% of the basin with higher concentration on eastern Amazon with tree cover loss of 30,000km^2 (Panniset et al., 2018).

Table 1: Drought comparison chart. Overview of the differences between the 3 major drought-induced forest cover loss in the Amazon basin

Conditions	2005 Drought	2010 Drought	2015 Drought
Driver of drought	Elevated warming in the Atlantic Ocean	Elevated warming in the Atlantic and Pacific resulting in more severe conditions than in 2005	Elevated warming in the Atlantic and Pacific resulting in more severe conditions than in 2005 and 2010
Precipitation deficit anomalies and temporal extent	Precipitation deficit anomalies of +1.8 SD during the JJAS period	Precipitation deficit of + 2.1 SD during JJAS period	Precipitation deficit of +3.4 SD during ONDJ period(almost more than double compared to 2005 & 2010.
The core of the precipitation deficit	W and SW Amazon (east less impact) Decreased cloudiness led to a surplus of solar radiation in the Central region covering 78.4 % area w/anomalous + values.	W and SW and SE Amazon	East Amazon and all the basin in general
Fraction of Amazon basin affected	37.9% of Amazon	42.5% of Amazon	80% Amazon
El Nino impact	Not due to El Nino, but to warming sea surface temperatures in the tropical North Atlantic Ocean	Successive to El Nino event and strong TNA-SST (sea-surface warming)	Strong El Nino episode 2015/2016 with a high P-deficit period. LST (land surface temp) exceeded +3.5 SD: warmest compared to mean temp. during 2000-2015
Main meteorological variables leading to drought	Precipitation+ Solar Radiation Water storage in the surface was 70% below 2003-2007 average (half of the anomaly of min terrestrial water stored in the basin)-Frappart,2012	Precipitation	Precipitation + land surface temperatures
Severity of drought	Worst drought at the time compared to the 1950s	More severe than 2005	Worst drought during 2000-2015 period
Tree cover loss	1.6x10*15 g of C	2.2x10*15 g of C	30,000km2

Table 2 describes the corresponding datasets used to compute HSi, tree cover percentage and vegetation index. Actual evapotranspiration is obtained from the Penman-Monteith Leunig Version

2 dataset with a 8-day temporal resolution and a 500 m spatial resolution (Zhang et al., 2019). This dataset stands out from previous AET datasets, since it measures AET coupled with gross primary productivity (GPP) which is linked to this parameter providing higher quality data. Also, this is the only product to date to provide evaporation, transpiration and interception as independent values which previous datasets do not provide. This dataset has been tested across different climates against multiple in site measurements displaying high correlation (Table 2, References). Potential evapotranspiration is obtained from MODIS product MOD16A2.006 at 8-day temporal resolution and 500m spatial resolution (https://doi.org/10.5067/MODIS/MOD16A2.006). Precipitation is obtained from Multi-Source Weighted Ensemble Precipitation dataset Version 2 at daily temporal resolution and 0.1-degree spatial resolution (11,100m) (Beck et al., 2019). Percent tree cover loss is obtained from Global Forest Cover Change at 5-year temporal resolution and at 30 m spatial resolution (Sexton et al., 2019). Normalized difference Vegetation Index is obtained from MODIS product MOD13Q1.061 Terra Vegetation Indices at 16-day temporal resolution and at 250 m spatial resolution (https://doi.org/10.5067/MODIS/MOD13Q1.061).

Table 2: Data Collection. Variables and datasets used to compute HSia and tree cover loss with their temporal and spatial resolution.

Data Collection

Variable	Product	Temporal resolution	Spatial resolution	Reference
AET (April 4, 2002-present)	**PML-V2** (Penman-Monteith-Leuning Version 2)	8-day	**500m**	Zhang et al.(2019)
PET (2001-present) AET(2001)	**MODIS** (MOD16A2.006 Modeling Imaging Spectroradiometer)	8-day	**500m**	https://doi.org/10.5067/MODIS/MOD16A2.006
P (1979-Oct. 2017)	**MSWEP-v2** (Multi-Source Weighted Ensemble Precipitation Dataset Version 2)	Daily	**0.1°** (11,100m)	Beck et al. (2019)
Tree Cover % 2000,2005,2010,2015	**GFCC** (Global Forest Cover Change)	5-yr	**30m**	Sexton et al. 2019
NDVI 2002-present	**MODIS** MOD13Q1.061 Terra Vegetation Indices	16-day	**250m**	https://doi.org/10.5067/MODIS/MOD13Q1.061

3. Results

By plotting percent Hydrologic Sensitive Area against tree cover loss percentage for all ecoregions, we are able to distinguish the ecoregions with lowest critical thresholds. In Figure 4, the critical threshold decreases between each event (steeper slope line). The top 11 ecoregions with lowest thresholds were color-coded, while the rest of the ecoregions (higher thresholds) were grayed out. These highly responsive ecoregions group along the northwestern, central, and southwestern areas. Many of these ecoregions are found in the eastern slopes of the Andes where elevation, rainfall, and vegetation growth is high compared to the rest of the basin (Weng et al., 2018) (Figure 5). Hydrologically sensitive ecoregions that appear to be sensitive in all three drought events and are found in the Southwest and part of the north-central Amazon include the Peruvian Yungas, Bolivian Yungas, and Negro Branco forests. Hydrologically sensitive regions that appeared both in the 2005 and 2010 drought are found in the Northwestern Amazon: Gurupa Varzea, Rio Negro Campirana, Japura Solimoes-Negro, and Jurua Purus Forest. Hydrologically sensitive ecoregions that appear both

in the 2010 and 2015 drought are Solimoes-Japura, Caquetá, and Eastern Cordillera Real. All other ecoregions only appeared as sensitive during a specific drought, in the 2005 drought: Marajo Varzea, Monte Alegre Varzea, Uatuma Trombetas and Ucayali forests; in the 2010 drought: Napo and Purus forests; and in 2015: Northwestern, Pantepui, Guianan Highlands, Guianan Piedmont forests. In figure 5a, the 2005 drought displays the sensitive ecoregions are clustered along the central and northern part of the basin. In figure 5b, the 2010 drought displays the sensitive ecoregions clustered mainly along northwest and southwestern part of the basin. In figure 5c, the 2015 drought display the sensitive ecoregions along the north and southwestern part of the basin. Figure 5d indicates all in one figure that the hotspot for sensitivity occurs within the pristine Amazon Forest in the western part of the basin, specifically the northwest and southwest, and central areas. All drought events impacted the southwest region. Apart from the southwest regions, the 2005 drought mainly impacted the central Amazon hydrology, the 2010 drought affected the northwestern edge of basin, while the 2015 drought affected the northern Amazon hydrology basin in general.

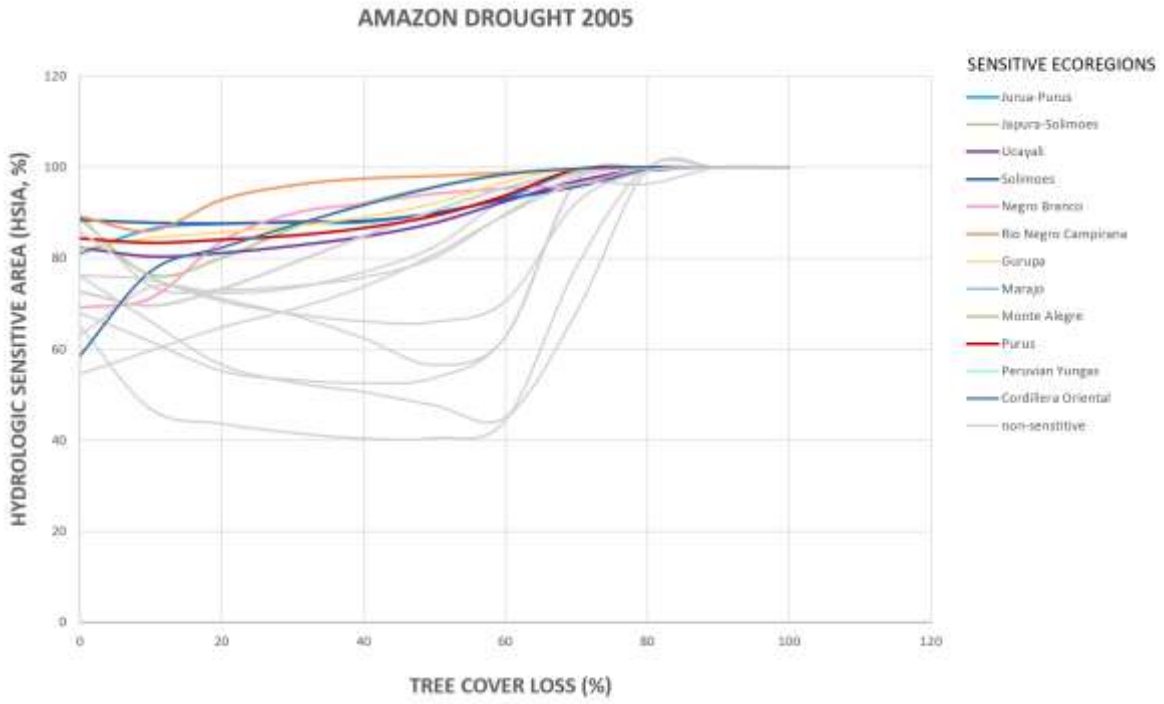
AMAZON DROUGHT 2005
HYDROLOGIC SENSITIVE AREA (HSIA, %)
TREE COVER LOSS (%)
SENSITIVE ECOREGIONS
Jurua-Purus
Japura-Solimoes
Ucayali
Solimoes
Negro Branco
Rio Negro Campirana
Gurupa
Marajo
Monte Alegre
Purus
Peruvian Yungas
Cordillera Oriental
non-senstitive

a)

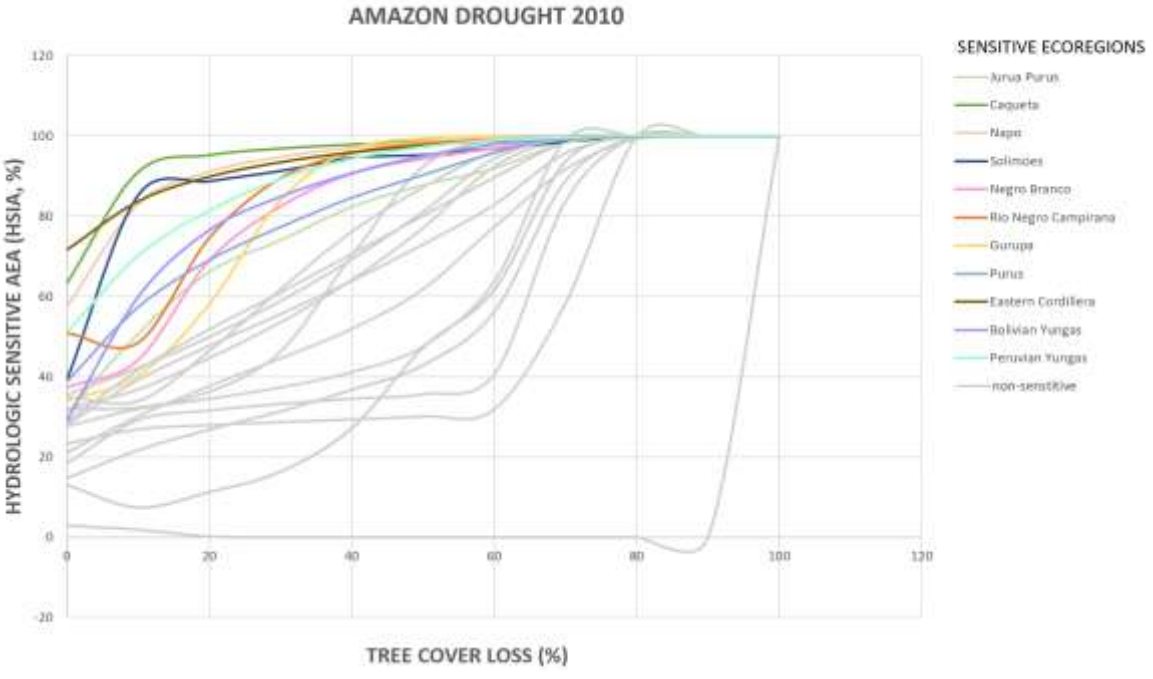
AMAZON DROUGHT 2010
HYDROLOGIC SENSITIVE AEA (HSIA, %)
TREE COVER LOSS (%)
SENSITIVE ECOREGIONS
Jurua-Purus
Caqueta
Napo
Solimoes
Negro Branco
Rio Negro Campirana
Gurupa
Purus
Eastern Cordillera
Bolivian Yungas
Peruvian Yungas
non-sensitive

b)

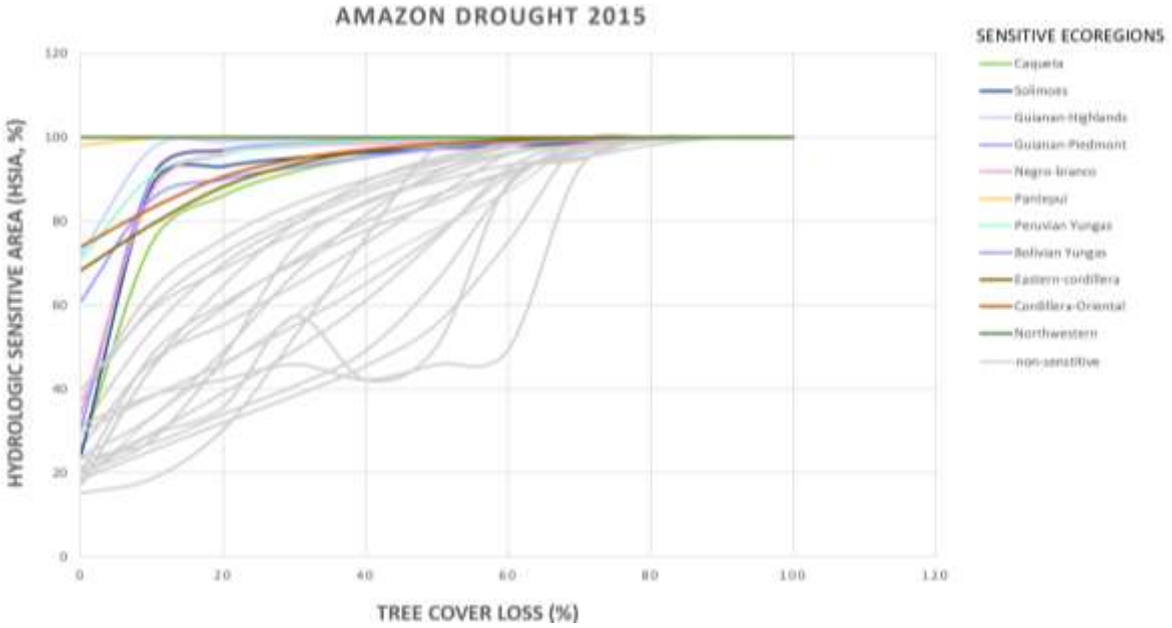

c)

Figure 4a-c: Sensitive Ecoregions for each drought event. Based on the trend of HSia plotted against percent TCL for each Amazonia ecoregion. Colored lines display the top 11 hydrologically sensitive ecoregions, while all other regions are grayed out.

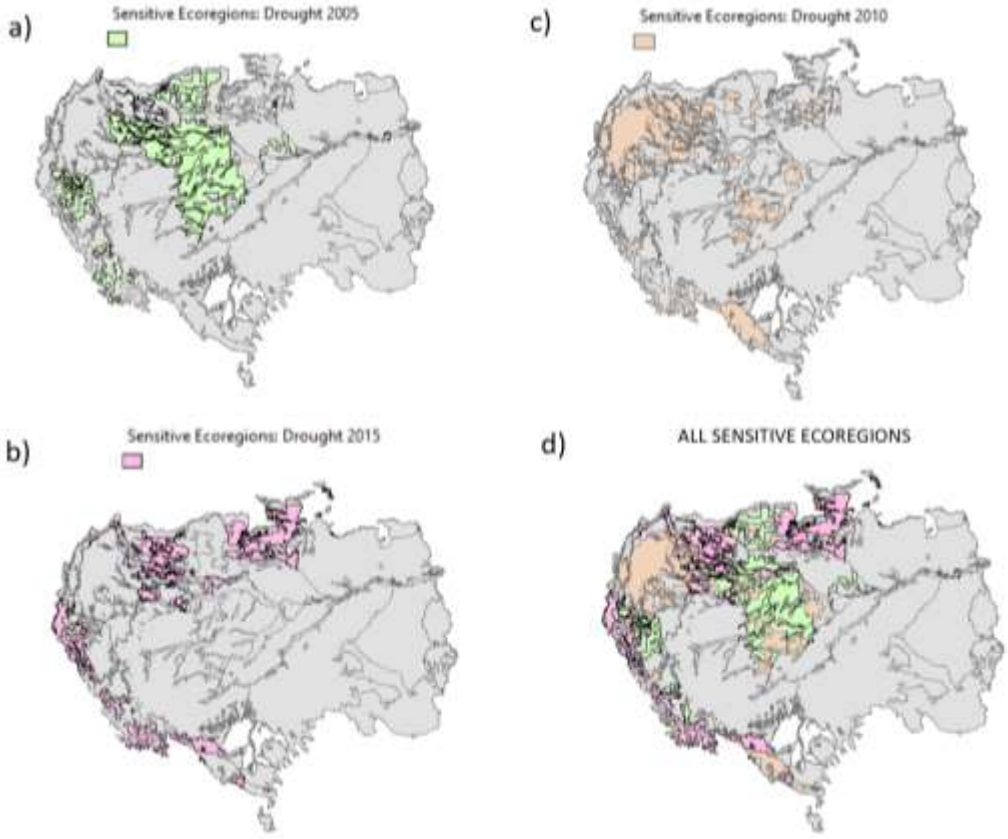

Figure 5 a-d: Hydrologically sensitive Amazon ecoregions. Results of sensitive regions for a) Drought 2005 (green); b) Drought 2010 (orange); c) Drought 2015 (pink) and d) All sensitive areas grouped together. Ecoregions with low sensitivity are grayed out.

We document times-series diagrams to observe changes in kNDVI for the 2005/06, 2010/2011, and 2015/16 drought years against the historical mean of the 2002-2019 period (the average does not include the latter drought years). The anomalies for kNDVI show a clear negative deviation from the historical mean in majority of ecoregions. In figure 6 for drought 2005/06, eight out of ten ecoregions display a clear negative anomaly between days 73 and 150 of year 2006. The highest anomalies are observed in Marajo Varzea (-0.34) and Rio Negro Campinarana (-0.24). In figure 7, for drought 2010/11, seven out of ten regions display anomalies at varying months during 2010 and 20111. The highest anomalies are observed in Bolivian Yungas (-0.201), Rio Negro Campinarana (-0.147), and Caqueta (-0.126). In figure 8, for drought 2015/16, all ecoregions display clear negative anomalies, with the most apparent during 2016. The highest anomalies are observed in Northwestern Andean Montane (-0.304), Eastern Cordillera Real (-0.213), and Pantepui (-0.18) ecoregions.

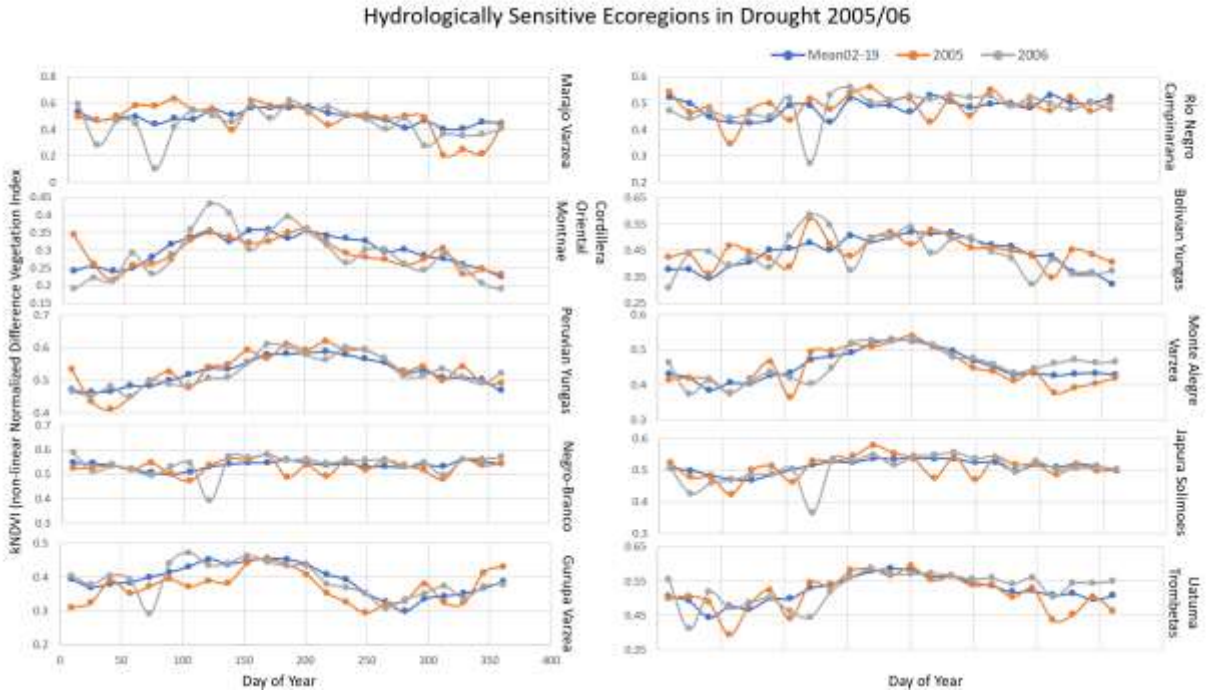

Figure 6: Time series of kNDVI for hydrologically sensitive ecoregions in Drought 2005/2006. Time series for 2005 (orange) and 2006 (blue) years are plotted relative to the historical mean 2002-2019 period. The historical mean does not include drought years.

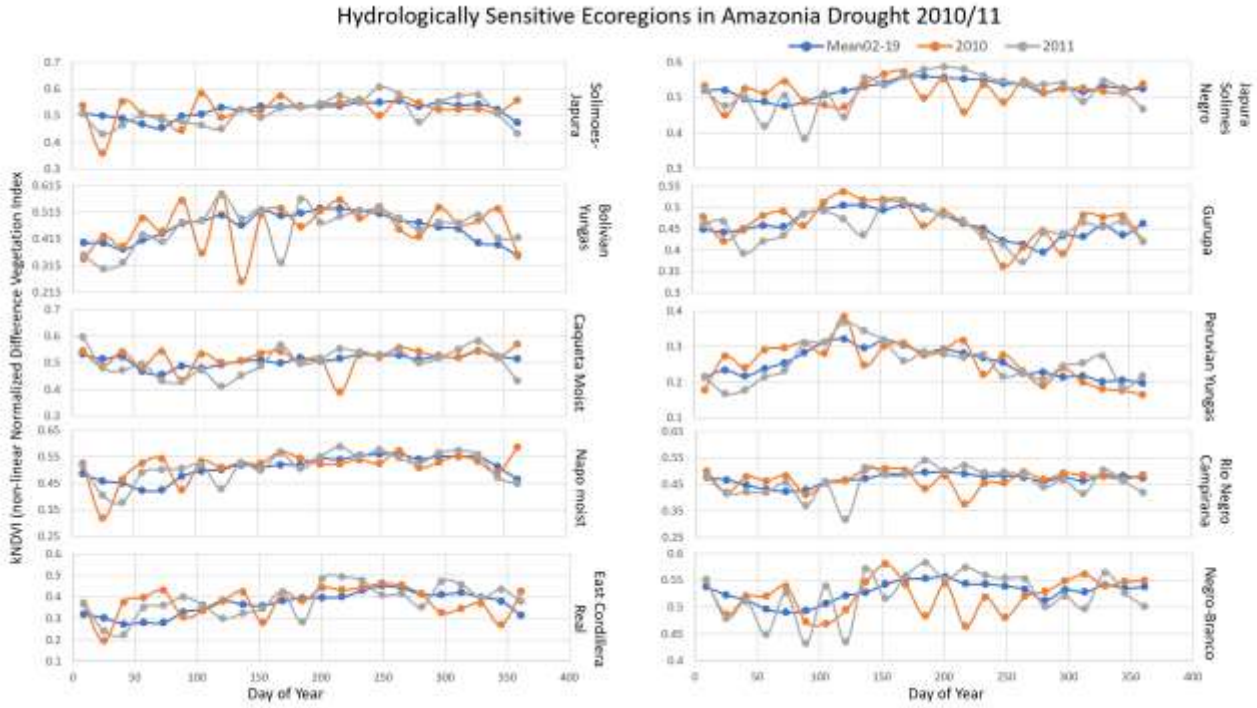

Figure 7: Time series of kNDVI for hydrologically sensitive ecoregions in Drought 2010/2011. Time series for 2010 (orange) and 2011 (blue) year are plotted relative to the historical mean 2002-2019 period. The historical mean does not include drought years.

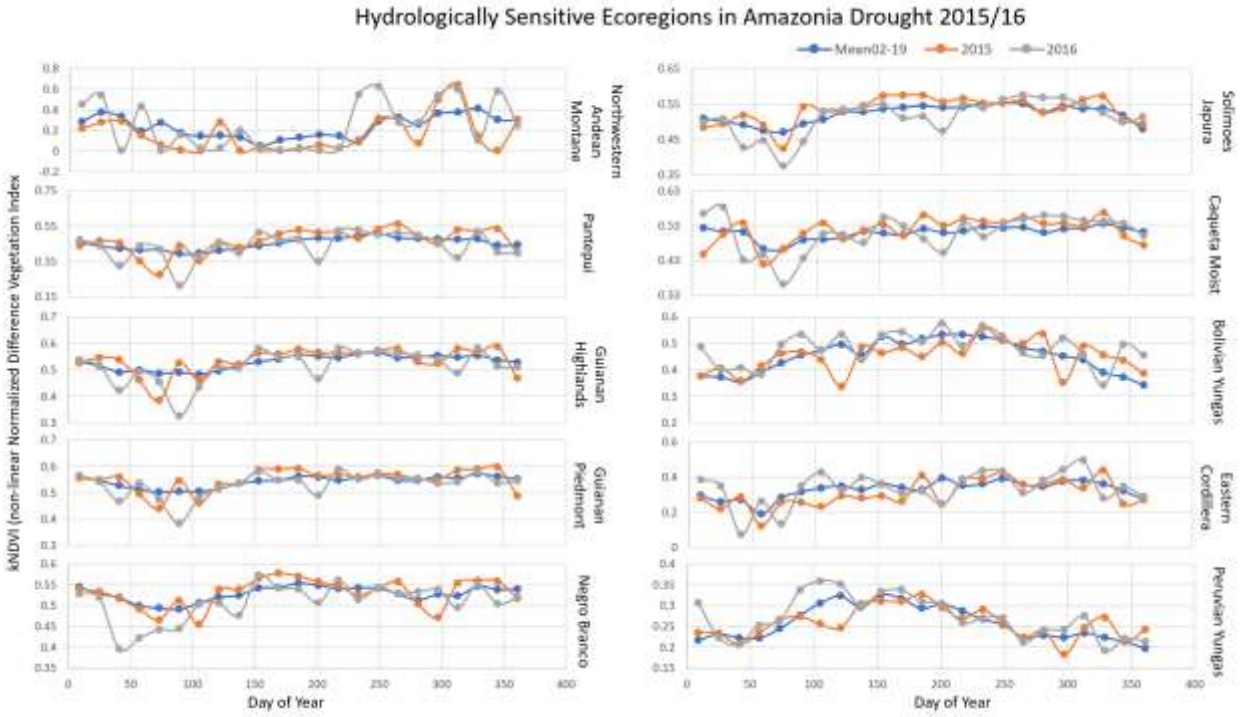

Figure 8: Time series of kNDVI for hydrologically sensitive ecoregions during Drought 2015/2016. The time series for 2015 (orange) and 2016 (blue) year are plotted relative to the historical mean 2002-2019 period. The historical mean does not include drought years.

In spatial retrospect, for the 2005/06 drought the kNDVI anomalies are concentrated on the southwestern and northern ecoregions. For the non-sensitive ecoregions, the southeastern part of the basin, the high anomalies is attributed to the arc of deforestation. In the 2010/11 drought, the north central area has a greater anomaly, while in 2015/16 and negative anomalies are basin-wide with greater clusters in the northern and northeastern areas (Figure 9).

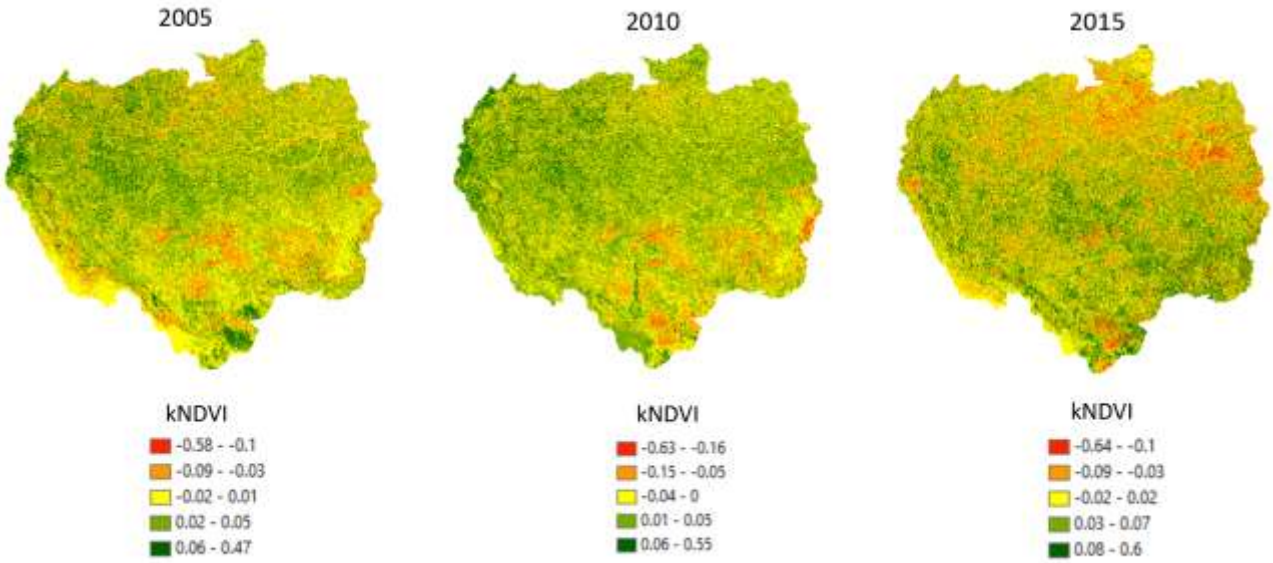

Figure 9: Amazon kNDVI anomalies relative to 2002-2019 period. Based on the difference of average kNDVI of 2005/06, 2010/11, 2015/16 relative to historical average 2002-2019 period. The historical average does not include extreme drought years. The figures display decrease (red) and increase (green) in transpiration or photosynthetic activity.

4. Discussion

At large scales reduced tree cover is known to decrease recycled rainfall up to ~30% (Staal et al., 2018, Spracklen et al., 2015, Leite-Filho. 2021) and is easily driven by drought (Staal et al., 2020; Zemp et al., 2017), resulting in an increase in longer dry seasons (Ruiz-Vasquez et al., 2020, Wunderling et al., 2022, Bagley et al., 2014) making tropical rainforests hydrologically sensitive to tree cover loss. Another study indicates that previous rainfall recycle values are underestimated and that loss of tree transpiration in the Amazon could result in a 55-70% decrease in precipitation

annually. Although all ecoregions in Amazon are hydrologically sensitive, our study shows the highest hydrologic sensitivity occurs along central, northern, and southwestern Amazonia ecoregions. The attribution for these results in the southwestern areas (Peruvian and Bolivian Yungas) is primarily due to local recycled rainfall where ~70% of their rainfall is generated in the Amazon (Zemp et al., 2017, Weng et al., 2018, Sierra et al., 2022). For the southwestern ecoregions, the dependency on rainfall recycling (which is ~30-50%) (Mu, 2021, Weng et al, 2018) is high, but slightly lower than the southwestern regions. This makes it hydrologically sensitive to tree cover loss. For the northern and central areas, a great source of rainfall stems from incoming Atlantic moisture, which is reduced during drought (Mu, 2021), representing up to 60% of rainfall within these ecoregions. Thus, the combination of a reduction in both recycled generated rainfall and incoming Atlantic moisture is a plausible explanation for high hydrologic sensitivity to tree cover loss and a drier climate state.

In contrast, although the non-sensitive ecoregions (southeastern grayed area) (figure 5) also benefit from moisture recycling (40%) (Connor et al., 2021), they have gained a degree of resilience to drought since they have been highly deforested in recent years resulting in a constant drier/warmer climate with more drought resistant vegetation species. This tropical savanna area, representing 20% of the Amazon basin, has undergone large-scale deforestation and conversion to pastureland where crops exert lower evapotranspiration rates compared to tropical native vegetation. Thus, this is a potential explanation as to why these ecoregions do not show relatively high values of hydrologic responses to drought or tree cover loss as compared to the rest of the basin.

The clear negative anomalies of the kNDVI values relative to the historical mean 2002-2019 for the majority of ecoregions support the hypothesis that tree cover loss results in the reduction in vegetation-generated rainfall. Since kNDVI is a strong proxy for photosynthetic activity coupled to transpiration processes responsible for the changes in rainfall patterns in Amazonia, observing

anomalous patterns in this index allows us to detect the ecoregions with the greatest transpiration losses (negative anomaly on kNDVI) during extreme drought. In the 2005/06 drought, the Marajo Varzea and Rio Negro Campinarana found in the western-central Amazon where this drought had a greater impact, show large anomalies in kNDVI along these ecosystems. Moreover, the Marajo Varzea ecoregion lies at the mouth of the Amazon River and largely separates the Atlantic Ocean from inland rivers. The predominance of palms such as burit and acai represents most of its vegetation (Sears, 2018). The most severe threat to this fairly intact region is recent human-induced habitat loss. Rio Negro Campinarana, on the other hand, is dominated by herbaceous savannas, lichens, and grasses. Epiphytic orchids and bromeliads are also abundant (Sears & Lemos, 2018). In the 2010/11 drought, the Bolivian Yungas found at the eastern foothills of the Andean Mountains had large negative kNDVI anomalies. The anomalies in transpiration are attributed to the high dependency on rainfall recycling. Moreover, the mountains block moisture from the North Atlantic trade winds enhancing this feedback. Slash and burn practices threaten most unprotected areas. Forest clearing occurs in foothills for crop cultivation which has endangered over 20 species. The Caqueta ecoregion, located in the northwestern Amazon, has resulted in the clearing of forests near the headwaters of the Vaupes region for large scale cattle ranching (Sears & Marin, 2018). These ecoregions are also found at the foothills of the Andean Mountains. The 2015/16 drought affected the Northwestern Andean Montane ecoregion where 50 % of plants are endemic species. The Eastern Cordillera Real Montane ecoregion, also affected in 2015/16, sits at eastern foothills of middle Andean mountains extending north-south from southern Colombia through Ecuador, and Northern Peru. The dominant vegetation species are tropical evergreens but species vary dramatically with elevation (Salcedo, 2018). The Pantepui ecoregion has relatively high elevation making it a quite intact area, but it is hydrologically sensitive due to its ability to capture moisture when recycling occurs. Overall, most of these impacted regions were found int

very sensitive areas of intact Amazon forested vegetation, regions threatened by increasing human activities.

5. Conclusions

Studies agree that the pristine areas are critical for a thriving Amazon ecosystem, particularly, for acting as a resilient system against climate change and intensifying droughts. In this study, however, we identify that the pristine and relatively intact Amazon areas are hydrologically sensitive to drought-induced tree cover loss, particularly along north, northwestern and southwestern Amazonia. Ecoregions within these areas include: Bolivian, Peruvian Yungas (southwest), Negro-Branco, Gurupa Varzea, Rio Negro Campirana, Japura Solimoes, Uatuma, Negro Campirana, Jurua Purus, Solimoes-Japura, Caqueta, Napo, Eastern Cordillera Real Montane, and Cordillera Oriental Montane (northern, northwestern and central). We attribute this impact to the high dependency on these regions on incoming rainfall generated from forest evapotranspiration relative to the rest of the basin. In this study, we also identified the ecoregions with greatest transpiration anomalies.: Rio Negro Campirnarana, Caqueta, Eastern Real Montane, Northwestern Andean montane, Pantepui, Bolivian Yungas, and Marajo Varzea. Previous studies have reported that recycled rainfall accounts for up to 70% (Weng et al., 2017) in the southwest region, and has a relatively long dry season. Thus, reduced rainfall can have major impacts on these ecosystems. Moreover, the recycled rainfall feedback accounts for up to 50% in the north and northwestern regions. In addition, a great portion of the rainfall in these regions also depends on incoming Atlantic moisture that is significantly reduced during drought, especially during the El Niño Southern Oscillation (Drought 2005 and 2010). Although the Northwestern Amazon is a well-preserved tropical forest, there is still a high level of misunderstanding as to the regional dynamics of land use and land cover change which will define the fate of the hydrologic processes for these ecoregions. There are traces of land use and land cover changes such

as illicit crops, logging, pastures, and forest regeneration due to land abandonment (Baker & Spracklen, 2019). How these ecological impacts will play out depends on where proximal land use change will take place, whether the Atlantic trade winds change in intensity, and how the behavior of new dry seasons will proceed (Wu et al., 2017).

References

Mu, Y., Biggs, T. W., & De Sales, F. (2021). Forests mitigate drought in an agricultural region of the Brazilian Amazon: Atmospheric moisture tracking to identify critical source areas. *Geophysical Research Letters*, *48*(5), e2020GL091380.

Bagley, J. E., Desai, A. R., Harding, K. J., Snyder, P. K., & Foley, J. A. (2014). Drought and deforestation: has land cover change influenced recent precipitation extremes in the Amazon?. *Journal of Climate*, *27*(1), 345-361.

Baker, J. C., & Spracklen, D. V. (2019). Climate benefits of intact Amazon forests and the biophysical consequences of disturbance. *Frontiers in Forests and Global Change*, *2*, 47.

Camps-Valls, G. et al., (2021). A unified vegetation index for quantifying the terrestrial biosphere. *Science Advances*, *7*(9), eabc7447.

Frappart, F. et al., (2012). Surface freshwater storage and dynamics in the Amazon basin during the 2005 exceptional drought. *Environmental Research Letters*, *7*(4), 044010.

Leite-Filho, A. T., Soares-Filho, B. S., Davis, J. L., Abrahão, G. M., & Börner, J. (2021). Deforestation reduces rainfall and agricultural revenues in the Brazilian Amazon. *Nature Communications*, *12*(1), 2591.

Panisset, J. S., Libonati, R., Gouveia, C. M. P., Machado-Silva, F., França, D. A., França, J. R. A., & Peres, L. F. (2018). Contrasting patterns of the extreme drought episodes of 2005, 2010 and 2015 in the Amazon Basin. *International Journal of Climatology*, *38*(2), 1096-1104.

Ruiz-Vásquez, M., Arias, P. A., Martínez, J. A., & Espinoza, J. C. (2020). Effects of Amazon basin deforestation on regional atmospheric circulation and water vapor transport towards tropical South America. *Climate Dynamics*, *54*, 4169-4189.

Salcedo, J. 2018. Eastern South America: Ecuador into Colombia and Peru https://www.worldwildlife.org/ecoregions/nt0121. Accessed July 9, 2018

Sears,R. 2018. Northern Brazil at the mouth of the Amazon River. https://www.worldwildlife.org/ecoregions/nt0138. 7 August 2018

Sears, R., Lemos Sa, Rosa. 2018. Northern South America: Northwestern Brazil and eastern Colombia. https://www.worldwildlife.org/ecoregions/nt0158. 29 September 2018.

Sears, R. Marín, C. 2018. Northern South America: Southeastern Colombia into Brazil https://www.worldwildlife.org/ecoregions/nt0107 Accessed July 31, 2018.

Spracklen, D. V., & Garcia-Carreras, L. J. G. R. L. (2015). The impact of Amazonian deforestation on Amazon basin rainfall. *Geophysical Research Letters*, *42*(21), 9546-9552.

Staal, A., et al., (2018). Forest-rainfall cascades buffer against drought across the Amazon. *Nature Climate Change*, *8*(6), 539-543.

Staal, A., et al., (2020). Feedback between drought and deforestation in the Amazon. *Environmental Research Letters*, *15*(4), 044024.

Weng, W., Luedeke, M. K., Zemp, D. C., Lakes, T., & Kropp, J. P. (2018). Aerial and surface rivers: downwind impacts on water availability from land use changes in Amazonia. *Hydrology and Earth System Sciences*, *22*(1), 911-927.

Wu, M., Schurgers, G., Ahlström, A., Rummukainen, M., Miller, P. A., Smith, B., & May, W. (2017). Impacts of land use on climate and ecosystem productivity over the Amazon and the South American continent. *Environmental Research Letters*, *12*(5), 054016.

Wunderling, N., Staal, A., Sakschewski, B., Hirota, M., Tuinenburg, O. A., Donges, J. F., ... & Winkelmann, R. (2022). Recurrent droughts increase risk of cascading tipping events by outpacing adaptive capacities in the Amazon rainforest. *Proceedings of the National Academy of Sciences*, *119*(32), e2120777119.

Zemp, D. C., Schleussner, C. F., Barbosa, H. D. M. J., & Rammig, A. (2017). Deforestation effects on Amazon forest resilience. *Geophysical Research Letters*, *44*(12), 6182-6190.

Conclusions and Future Work

For the first study, I assessed the hydrologic sensitivity to climate variability for all terrestrial biomes. We established a novel metric, the Hydrologic Sensitivity Index, which measures the hydrologic response of any region to climate variability and can be applied to small and large scales. This index is based on annual values of PET and AET, and P, to assess the interannual change in hydrologic behavior (ΔAET/P) of a location relative to a change in climatic condition (ΔPET/P). For values $HSi \geq 1$: Sensitive and $HSi < 1$: Resilient. This index is also useful to determine the hydrologic and climate condition direction. For instance, a decrease in water yield (+ΔAET/P, higher AET) or an increase in water yield (-ΔAET/P, higher AET) plus an increase in warmer conditions (+ΔPET/P) or cooler conditions (-ΔPET/P). In summary, this study indicates that the majority of the regions detected as hydrologic sensitive areas are changing towards drier conditions with decreasing water yields. Moreover, the highest responses of hydrologic sensitivity to climate variability were identified within high and low latitudes during the 2001-2016 period. Particularly, tropical rainforests show the largest hydrologic sensitivity with the majority of their sensitive area trending towards decreasing water yields followed by boreal systems with increasing water yields. We found that sensitivity is amplified at high elevations and in steep-sloped terrain (high slope angle), outlining the importance of topography on hydrologic responses. We direct the attention toward climate warming resulting in increasing snow melt and precipitation in Arctic tundra and boreal forests and increasing tree cover loss in tropical forests, as possible mechanisms driving the observed patterns. Globally, boreal and tropical forests, the two biomes producing the greatest water yields also display the greatest extent of hydrologic sensitive land. This makes them hotspots for hydrologic surveillance of expected impacts from further increases in climatic shifts with the potential to significantly alter the global water cycle. Future work (second study) should determine if the

hydrologic sensitivity patterns found in this study represent tipping points in changing hydrologic dynamics within each biome and assess at the regional and local scale their cascading impacts on ecosystems and human settlements.

For the second study, we globally synthesized the hydrologic sensitivity to forest cover loss by computing the critical thresholds (tipping points) of forest cover loss across different forest types that underwent either drought, wildfire, or deforestation-induced tree mortality. Using the novel HSi metric we computed the sensitive area in 45 events covering five distinct forest types (Tropical, Boreal, Temperate Coniferous, Mixed and Mediterranean forests) and plotted the results against tree cover loss. The trends were useful to compute the sensitive rate (the speed at which the affected area attains hydrologic sensitivity) once the critical thresholds were surpassed. Forests with lower-than-median critical thresholds of tree cover loss before heightened hydrologic responses are established (<19%) were identified particularly within the Congo basin, Sumatra Island, Borneo island, and Chilean subtropical areas. Overall, this study shows that tropical rainforests display more sensitivity to land cover changes indicating that flourishing tree cover represents a key role in providing stability in their hydrologic systems. This trend is followed by the boreal systems with low critical thresholds (~32%) while high critical thresholds (46-53%) are seen in the Temperate Forest group (Temperate Coniferous, Mixed, and Mediterranean). Studies agree that the tree cover loss (mainly deforestation and drought) in the tropics results in decreases in recycled precipitation, accounting for up to 30-70% which is our major explanation for the high hydrologic responses to tree cover loss. Boreal system hydrologic has not been widely assessed in previous work and we identified that their hydrology also becomes unstable due to tree cover loss (mainly as a result of wildfire events).

For the third and final study, we assessed the hydrologic sensitivity to drought-induced tree cover loss for the 30 distinct Amazonia ecoregions during 2005, 2010, and 2015 droughts. We identified pronounced hydrologic sensitivity to tree cover loss in the pristine Amazon area within the southwestern,

central, and northwestern ecoregions. Studies agree that the most sensitive regions are located in the southwest since 70% of its rainfall is generated by tree transpiration. This area is dominated by the Peruvian and Bolivian Yungas, The northwestern and central pristine areas are also dependent on vegetation for generating 50% of their rainfall in addition as well as the incoming Atlantic moisture which are both reduced during extreme drought. These ecoregions include: Negro-Branco, Gurupa Varzea, Rio Negro Campirana, Japura Solimoes, Uatuma, Negro Campirana, and Jurua Purus, Solimoes-Japura, Caqueta, Napo, Eastern Cordillera Real Montane, and Cordillera Oriental Montane. Anomalies in transpiration were evaluated for each ecoregion where the Bolivian Yungas, Marajo varzea, Rio Negro Campinarana, Northwestern Andean Montane, and Eastern Cordilleran Real Montane display the greatest transpiration loss due to drought relative to a historical average 2002-2019 period. The majority of these ecoregion are located at eastern foothills of the Andes mountains with high endemism of species.

Vita

Marisol Dominguez completed her B.Sc. in Environmental Sciences degree at the University of

Texas at El Paso (UTEP) in Spring 2016. As an undergraduate student, she worked as a Math Tutor and volunteered as an intern at the Environmental Protection Agency (EPA) Region 6 where she became aware of the water scarcity issues her community faces. Marisol then enrolled in the PhD in Geology (Hydrology focus) in the Spring of 2017 at UTEP. In the Spring of 2018, Marisol was granted the National Science Foundation Graduate Fellowship to fund her research for 3 years. She decided to graduate with her master's degree along the way in December 2021 while at the same time publishing her first work entitled "Global Analysis of the Hydrologic Sensitivity to Climate Variability" in Journal of Hydrology. Throughout her time as a graduate student, she worked as a research and teacher assistant and presented her research at multiple conferences such as the American Geophysical Union (AGU, New Orleans 2017, Washington D.C. 2018) and European Geophysical Union (EGU, Vienna 2019), Japan Geophysical Union (JPGU, Chiba Prefecture 2019) and Frontiers in Hydrology (FHAGU, San Juan 2022), while teaching undergraduate level Introduction to Physical Geology course. In the Fall of 2018, she won the Outstanding Paper Award at the AGU Conference. In March 2019, she won in a 3-Minute Thesis Competition held at her university. Apart from her science career, she is a professional painter which focuses on painting wildlife presenting her work in the AGU Virtual Art exhibit at the American Geophysical Union Chicago in December 2022. Marisol is currently working as a Field Hydrologist at the International Boundary and Water Commission overseeing the Rio Grande river water by monitoring water levels and discharge across diverse gaging stations and making deliveries during scheduled periods between U.S and Mexico. Finally, she is obtaining her Ph.D. in Geological Sciences in May 2023. Contact Information: marisol.dominguez@ibwc.gov